

Alma Mater Studiorum - University of Bologna  
Department of Electrical, Electronic, and Information Engineering  
“Guglielmo Marconi” - DEI

Thesis for the Doctorate of Research in Electrical Engineering

**Fabrication, Electrical Characterization and Simulation  
of Thin Film Solar Cells: CdTe and CIGS Materials**

Presented by

**Nima E. Gorji**, PhD Candidate

**Coordinator:** Prof. Domenico Casadei

**Tutor:** Prof. Ugo Reggiani

**Advisor:** Dr. Leonardo Sandrolini

Cycle XXVI

SD 09/E1-Elettrotecnica, SSD ING-IND/31-Elettrotecnica

December 2013, Bologna, Italy

## PREFACE

CdTe and Cu(In,Ga)Se<sub>2</sub> (CIGS) Chalcogenide materials are the most promising semiconductor compounds for large scale production of efficient, low-cost thin film solar cells, and several research institutes and companies such as First Solar Company have announced their plans for their large production lines. Such devices to become a commercial successful, a number of issues require being concerned such as upgraded fabrication process, material properties analysis and characterization which can lead to high efficiency and long-term stability. In this thesis, we start from the fabrication of CdTe thin film devices where the R.F. magnetron sputtering system is used to deposit the CdS/CdTe based solar cells. The CdCl<sub>2</sub> post-growth treatment is modified in order to uniformly cover the cell surface and reduce the probability of pinholes and shunting pathways creation which, in turn, reduces the series resistance. The deionized water etching is proposed, for the first time, as the simplest solution to optimize the effect of shunt resistance, stability and metal-semiconductor inter-diffusion at the back contact. Also, it is proposed that water rinse can reduce the effect of annealing in Ar ambient. This idea can be a cheaper and easier alternative for the electropolymerization of an organic conductive polymer material (i. e. polypyrrole) on the semiconductor CdTe surface, before the metallic back contacting. This interfacial layer can avoid shunting pinholes and surface defects. In continue, oxygen incorporation is proposed while CdTe layer deposition. This technique has been rarely examined through R.F sputtering deposition of such devices. The variation in the size of the grains and phase transformation are considerable and in some aspects are not consistent with the devices fabricated by other deposition techniques. Oxygen could increase the grain sizes effectively and could transform the crystallinity from cubic phase to hexagonal for a higher O<sub>2</sub> content. The above experiments are characterized electrically and optically by current-voltage characterization, scanning electron microscopy, x-ray diffraction and optical spectroscopy. Furthermore, for the first time, the degradation rate of CdTe devices over time is numerically simulated through AMPS and SCAPS simulators. The simulation results are in consistency with the practical reports. It is proposed that the instability of electrical parameters is coupled with the material properties and external stresses (bias, temperature and illumination). This analysis tracks the formation of mid-gap defects as a function of excess charge carriers, the profile of which depends on different defect creation process. We show that there is a coupling between the defect concentration and carrier concentration which can alter the material properties and increase the recombination rate or built-in field. In the second part of the thesis, the CIGS materials are simulated and characterized by several techniques. The surface photovoltage spectroscopy is used (as a novel idea) to extract the band gap of graded band gap CIGS layers, surface or bulk defect states energies and to study the doping homogeneity of thin film structures. The surface roughness is scanned by atomic force microscopy on nanometre scale to obtain the surface topography

of the film. We verify that the improvement in crystallinity of the film occurs by the coalescence of the neighbouring islands driven by the thermal energy acquired from the annealing treatment. Next, the effect of carrier collection time and series resistance on the current-voltage characteristics of the CIGS devices are investigated by two and four-points probe technique. Moreover, the simulation studies are performed to analyse the effect of the diffusion and recombination at the grain boundaries and trap states that are normally present in the film morphology. A modified equivalent circuit is proposed and the formulation is extended for such phenomenon. In another approach, the band gap grading in the valence band is simulated by AMPS simulator and several graded profiles are examined in order to optimize their thickness, grading strength and electrical parameters. Furthermore, the transport mechanism in CIGS devices are modelled through a simple theoretical approach to show the effect of the grading strength, recombination rate at the space charge region of the solar cell. For the first time, the Auger generation is modelled in a graded band gap CIGS device. The simulations show a higher theoretical efficiency and current voltage-characteristics which which are strongly dependent on the probability of secondary electron generation. All the above obtained results suggest further investigations and a systematic development through both practical and theoretical researches.

## ACKNOWLEDGEMENTS

I should acknowledge many people who supported me by their knowledge and kindness during the completion of this thesis.

Any success I experience in my life is as much a reflection of the support of my family. Nobody overestimates their effective role in a successful life.

I am thankful to my tutor, Prof. Ugo Reggiani, and my advisor, Dr. Leonardo Sandrolini, for their scientific supports. Their understanding and guidance made this PhD efficient. It is really interesting to work with them. Prof. Karpov is appreciated for his friendly and fruitful practical and theoretical guidance and encouragement during my internship in the University of Toledo, Ohio, USA. From this University, I also remember to thank Dr. Dohyoung, Dr. Vasko and Dr. Grice who assisted me in fabrication and characterization of CdTe devices. I also appreciate Dr. Nardone for the valuable discussion on the numerical analysis of degradation mechanisms.

The CIGS devices that I received were fabricated by Prof. Barreau, and Prof. Kauffmann from France and Germany. Their collaboration is greatly acknowledged. Moreover, the researchers of the Department of Physics of the University of Bologna and ARCES (Cesena) are appreciated for their cooperation.

I am very thankful the three years financial support of my PhD by MIUR scholarship. Also, Marco Polo Grant by my department (DEI) for my internship in USA (2013) is acknowledged.

Intel Company is gratefully appreciated for the Doctoral Student Honour Award which partially financed the completion of this thesis.

All the friends, colleagues and officemates are the subject of my special thanks. Best wishes for your future plans and endeavours.

I must declare my joyful life here in Italy. It was a great opportunity to live in such a wonderful country as expected.

*dedicated to Italian researchers of photovoltaic systems*

## CONTENTS

• Preface	I
• Acknowledgements	III
• Introduction	VI
• <b>CHAPTER I. Fabrication of CdTe Thin Film PV Devices</b>	1
1.1 Fabrication of CdTe Thin Film Devices	2
1.2 Fabrication Experimental Procedure	2
1.3 CdCl <sub>2</sub> Treatment and Annealing	3
1.4 Shunting Pinholes	7
1.5 Conclusion of CdTe Fabrication	10
• <b>CHAPTER II. Electrical Characterization of CdTe Thin Film Devices</b>	12
2.1 Electrical Characterization Applications	13
2.2 Surface Modification; Nonuniformity Effects	13
2.3 Current-Voltage Characterization (DIW Rinse)	15
2.4 SEM Characterization (DIW Rinse)	18
2.5 XRD Characterization (DIW Rinse)	20
2.6 Optical Characterization (DIW Rinse)	21
2.7 Oxygenation of CdTe Layer	23
2.8 SEM Characterization (Oxygenated CdTe)	24
2.9 XRD Characterization (Oxygenated CdTe)	26
2.10 Conclusion of Characterizations	27
• <b>CHAPTER III. Simulation of Degradation in CdTe Thin Film PV Devices</b>	29
3.1 Degradation of the electrical parameters	30
3.2 Numerical Algorithm	32
3.3 Theory and Model	33
3.4 Variation of Electrical Parameters by Time	36
3.5 Degradation Feature in J-V Curves	40

• <b>CHAPTER IV. Electrical Characterization of CIGS Thin Film PV Devices</b>	46
4.1 Electrical Characterization, Spectroscopy and Microscopy	47
4.2 CIGS Sample Preparation	47
4.3. Surface Photovoltage Spectroscopy Analysis	49
4.4 Atomic Force Microscopy Analysis	52
4.5 Admittance Spectroscopy (J-V Measurements)	53
4.6 Two and Four-points Probe Characterization	54
• <b>CHAPTER V. Simulation of CIGS Thin Film PV Devices</b>	58
5.1 Trap States and Grain Boundaries Equivalent Circuits Modeling	59
5.2 Equivalent Circuits Modified for Buffer Layer and Auger Generation Phenomena	61
5.3 Band Gap Grading of CIGS Thin Film Solar Cells	64
5.4 Valence Band Grading	64
5.5 Conduction Band Grading	69
5.6 Graded Window Layer	71
• <b>CHAPTER VI. Modeling the CIGS Thin Film Photovoltaics</b>	72
6.1 Transport Mechanism in CIGS Devices	73
6.2 Photocurrent Density	74
6.3 Optimization of the Photocurrent Density	77
6.4 Auger Generation Mechanism	81
6.5 Auger Generation Formulation	83
6.6 Parameters Optimization for Auger Generation Probability	87
6.7 Conclusion of Simulation and Modeling	92
• <b>Conclusions</b>	94
• <b>References</b>	95

## Introduction

The subjects of this thesis are thin film solar cells based on sulfide, selenide, or telluride semiconductors. We call them the chalcogenides. The most prominent members, at least today, are CdTe and Cu(In,Ga)Se<sub>2</sub> (CIGS). The history of CIGS-based solar cells began in 1975 when Bell laboratory scientists achieved 12 % solar energy conversion efficiency with a cell where a layer of CdS was evaporated onto a CuInSe<sub>2</sub> single crystal. As the first evaporated CuInSe<sub>2</sub> films (from CuInSe<sub>2</sub> and Se evaporation sources) suffered from poor control of the ratio of copper to group III element, Cu/In (in early days the group III element was only indium). Material aspects of the chalcogenides for photovoltaics are with focus on II-VI and I-III-VI<sub>2</sub> materials.

These solar cells have been in production since the beginning of the twenty-first century, and production volume is growing rapidly. More companies are entering the field, each company expecting efficiency and cost advantages from their specific cell design or production process. This commercialization period, however, had a long forerunner. Chalcogenide photovoltaics has been the subject of research and development for four decades. The hope was that the use of polycrystalline films, instead of single crystal materials, would allow the fabrication of low-cost solar cells. Counting from 1980, there have been over 80 international scientific events dealing with this material group and its application in solar cells.

The authors do remember enthusiastic periods when exploitation appeared just ahead and then again pragmatic periods when more research was shown to be needed. However, constantly important findings have been made several of them producing unexpected results. The method was empirical science where in the best case theoretical understanding was the second step. The findings brought out several so-called magic steps which now are executed in production. Today it is fair to say that the achievements have been remarkable: chalcogenide-based photovoltaic devices achieve the highest energy conversion efficiencies among the thin film technologies more than 20 %.

Cost aspects require that photovoltaic devices to be fabricated from the abundant materials with low energy consumption, and with negligible environmental impact but in the same time to show a high efficiency of solar-to-electrical energy conversion. Chalcogenide thin film solar cells already fulfil many of these requirements. Last year, (2013), polycrystalline CdTe and CIGS thin film solar cells have shown a remarkable record efficiency of about 18.7 % and 20.4 % in laboratory scale, respectively [1, 2]. This values is still considered as a miracle, given that so many basic material properties are not well understood yet (Fig. 1).

As potentially efficient and low cost materials, many research groups are working on the electrical and optical properties of these types of solar cells. The hope was that the use of polycrystalline films instead

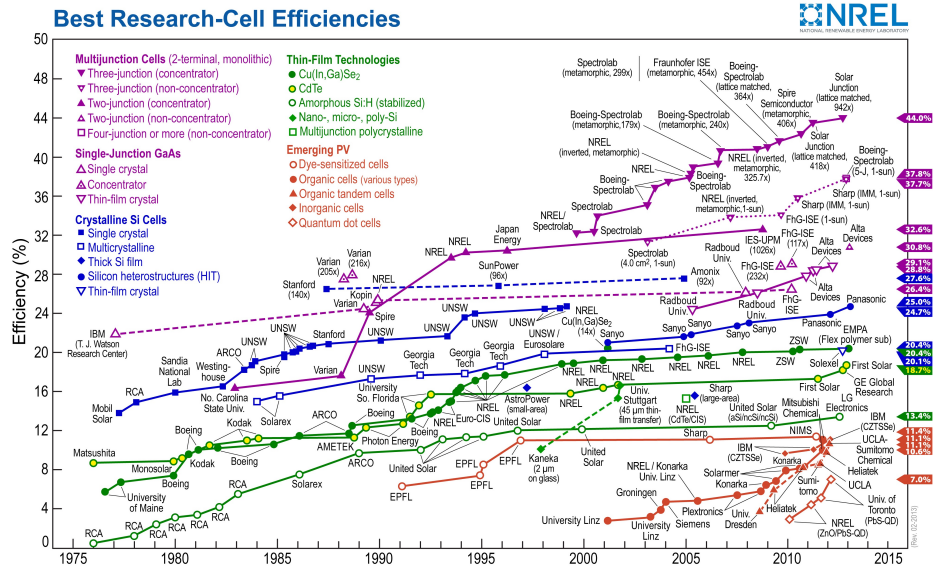


Figure 1: Development milestones for CdTe and CIGS thin film photovoltaics.

of single crystal materials would allow the fabrication of low-cost solar cells. To date, several deposition techniques such as magnetron sputtering [3], close-spaced sublimation [4], vapour-transport deposition [5], electro-deposition [6], screen-print deposition have been successfully developed for CdTe fabrication. CIGS devices are usually prepared by co-evaporation three stage process from elemental sources in the substrate configuration or roll to roll technique [7, 8]. The goal of all the deposition techniques are to obtain thin film modules with more than 15 % efficiency produced with costs below 0.5 \$/W [9, 10]. However, in despite of their industrial employment more research is necessary to reduce the degradation rate and instability of thin films which can further make this devices reliable [11].

Overall, improved processing and solar cell architectures together with new and improved characterization methods involving the latest development in microscopy and electrical measurement equipment are required in order to achieve the highest reliable energy conversion efficiencies among the photovoltaic technologies.

## Chapter I

### Fabrication of CdTe Thin Film PV Devices

In this chapter are considered two observable phenomena in the experimental fabrication and electrical characterization of the R.F. sputtered CdS/CdTe thin film solar cells which extremely reduce the overall conversion efficiency of the device: CdCl<sub>2</sub> residue on the surface of the semiconductor and shunting pinholes. The former happens through nonuniform treatment of the as-deposited solar cells before annealing at high temperature and the latter occurs by shunting pinholes when the cell surface is shunted by defects, wire-like pathways or scratches of the back contact from the external contacts. Such physical problems may be quite common in the experimental activities and reduce the performance down to 4-5% which leads to dismantle the device despite its precise fabrication. We present an electrical characterization on the samples received wet CdCl<sub>2</sub> post-growth surface treatment and annealing but are then damaged by the shunting pinholes.

## 1.1 Fabrication of CdTe thin film devices

It is now well known that CdCl<sub>2</sub> post-growth treatment and annealing at high temperature prior metallic back contacting the cell can greatly improve the electrical characteristics and stability of CdTe solar cells [12, 13]. The suggested reasons are that this treatment can: increase the grains size to about 1-2  $\mu\text{m}$  [14], reduce the surface and interfacial energy [15], and randomise the orientation of CdTe film [16]. The bigger grains and fewer boundaries in thin films lead to bigger minority carrier lifetime and lower resistivity due to fewer grain boundaries. CdCl<sub>2</sub> treatment and annealing either during or after CdTe film growth is a commonly used process to increase the grain size and density of the CdTe film. However, this step is very critical specially when the employment of CdCl<sub>2</sub> solutions is not by the dry vacuum process such as physical vapour deposition but is achieved through a wet surface treatment. Then the problem arises when the residue of CdCl<sub>2</sub> is left on the film surface and may not be eliminated or washed due to formation of Oxychlorides which are insoluble in water [17, 18].

Niles et al., suggested that CdO, TeO<sub>2</sub>, TeCl<sub>2</sub>O are building blocks for the surface Cl residue [17]. This happens when CdCl<sub>2</sub> solutions does not cover the cell surface uniformly and leaves residuals before the annealing process. The other common issue with a comparable effect is the shunting pinholes which act as shunting pathway through front and back contact. The defective pinholes or *local spots* on the surface of the solar cell can shunt the photocurrent through formation of a wire-like connection, thus decreasing the measured shunt resistance, open circuit voltage and degrade the overall performance of the device [19]. Both above issues have been shown to reduce the performance down to 4-5 % and dismantle the sample, therefore, they cannot be disregarded. We experimentally verify the strong effect of both cases on the electrical parameters of the device such as series and shunt resistances as well as performance parameters.

## 1.2 Fabrication experimental procedure

In this study, CdS/CdTe samples were R.F. sputtered in AJA system at 250 °C onto a rotating TEC15 glass substrate coated with a High Resistive Transparent (HRT) layer of SnO<sub>2</sub>:F. The thin films were deposited at 10 mTorr Argon pressure, 50 W R.F. power with a substrate temperature of 270 °C. A CdS layer of 60 nm thickness was chosen as the heterojunction partner (window) of CdTe cells. The sputtered CdTe thickness was 2.1  $\mu\text{m}$ . During deposition, the sputtering rate was calculated by using an in-situ thickness monitor system and also verified by a DEKTAK profilometer after finishing the device. As-deposited CdS/CdTe films were then CdCl<sub>2</sub> treated and annealed at high temperature 387 °C as the standard activation temperature for sputtered cells. The treatment system includes a glass tube furnace in which the temperature is controlled by two halogen lamps on top and two other on bottom (750 Watt/lamp). The samples are activated between two graphite susceptors (9/16" thick) for uniform heat distribution and two



Figure 2: The three main step of CdTe deposition process; 1: R.F. sputtering machine, 2: activation chamber, 3: metallization bell.

thermocouples to control the temperature of each side. After the heat treatment, the samples were blown N<sub>2</sub> gas to remove the dusts before Cu/Au back contact metallization (3.2 nm Cu and 20 nm Au) in a Bell-jar thermal evaporation system.

Finally, a copper diffusion heat treatment of 150 °C for 45 min was performed in room air ambient [20]. We note that CdCl<sub>2</sub> treatment was achieved after a methanol rinse and the samples were treated by a syringe which sucks in and drops a few CdCl<sub>2</sub> solution over the surface. This step is very critical since it is done by hand and depends mostly on the experience of the experimenter. Considering the effects of this step is one of the targets of this chapter. The electrical characterization was achieved under illumination of 100 mW/cm<sup>2</sup> through pogo-pin electrodes. A fan was cooling the characterization area in order to reduce the temperature effect on the current generation rate. Three main step of the CdTe thin film deposition process have been illustrated in Fig. 2. Step 1 refers to the R.F. sputtering process where the CdS and CdTe are deposited regularly on the glass/TCO substrate. Step 2 is to activate the device with CdCl<sub>2</sub> as post-growth treatment and annealing at high temperature. Step 3 is to deposit the metallic back contact through thermal evaporation at high voltage as was defined above.

### 1.3 CdCl<sub>2</sub> treatment and annealing

The common activation solution for almost all CdTe based thin film solar cells is CdCl<sub>2</sub> solution. However, the method of activation is different depending on the thin film deposition method. For example, the films

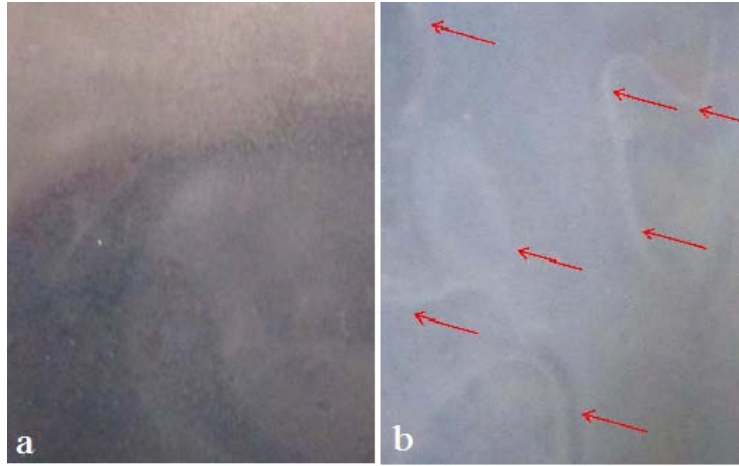


Figure 3: The CdS/CdTe thin films treated with  $\text{CdCl}_2$  solution through, a. uniform and b. nonuniform treatment.

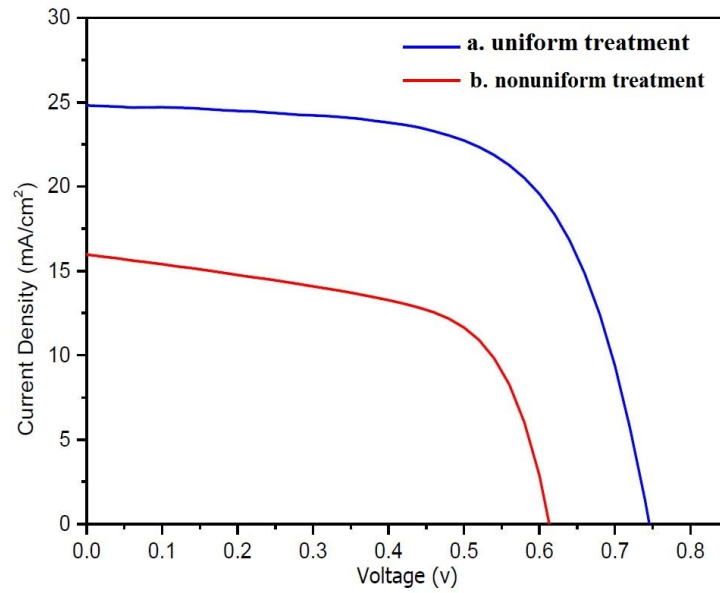


Figure 4: The current-voltage characteristics of the samples prepared through: a. uniform and b. nonuniform treatment.

grown by the close-spaced sublimation technique receive  $\text{CdCl}_2$  by evaporation [21, 22]. The evaporated solution uniformly covers the thin film and it can be immediately inserted into activation system. However, this method is not used in many other techniques like R.F. sputtering techniques which the treatment solution is dropped by hand using syringe or sucking tools. Attention must be paid to cover the entire sample uniformly and prevent the surface residuals. In our experiments, the sputtered CdS/CdTe sample is first cleaned by methanol and then is heated for some seconds. Next, a few drop of  $\text{CdCl}_2$  solution is poured on the sample by syringe and we wait the solution cover all over the sample. However, this step is not easy to handle since  $\text{CdCl}_2$  dries in some seconds before spreading over.

The difference between the uniform and nonuniform covered samples with  $\text{CdCl}_2$  is clear by the white fringes, tracks and lines which appear some seconds after this solution dries. Ignoring this critical issue and heating the cell with such inappropriate treatment can lead to quite low performance and to dismantle the cell. Fig. 3 shows the difference between uniform and nonuniform  $\text{CdCl}_2$  treatments. The dense white areas in Fig. 3(b) (indicated by the arrows) are formed when the solution cannot spread over uniformly and instead leaves residuals in some track forms. To show the importance of this step, both samples have been annealed at  $387^\circ\text{C}$  after the treatment and finished by the metallization. The relevant current-voltage curves are drawn for each sample in Fig. 4. The gap between the curves is significant.

The efficiency of the nonuniformly treated cell (with residuals) is 5.84 % while that of the uniformly treated one is about 11.83 %. This is a significant difference which was verified by repeating the treatment several times. A nonuniform treatment has a very strong influence on the performance because of the decrease in the  $V_{oc}$  and  $J_{sc}$ . Normally, when the solution residue over the cell, the  $\text{CdCl}_2$  solution is washed out by methanol and dried by heating for some seconds and the above process is repeated again. Disregarding such residuals lead to the low performance parameters. Surprisingly, shaking the sample for some seconds after the  $\text{CdCl}_2$  pouring can help to spread the solution all over the sample and to make a uniform treatment [23]. This avoids sediments of the solution on the cell surface and the remnant of the solution goes to the edges out of the solar cell area.

Fig. 5 displays the normalized electrical parameters in box plot; open circuit voltage  $V_{oc}$ , short circuit current  $J_{sc}$ , fill factor  $FF$  and efficiency ( $\eta$ ) for the 35 cells fabricated on each of the two (a) and (b) samples. The open circuit voltage is compared in actual values as its values are already fewer than one. All the data were obtained after finishing the cell with Cu/Au back contact deposited through a mask to provide a dot cell having an area of about  $0.062\text{ cm}^2$ . The samples were characterized under one sun illumination at room temperature.

Clearly, the higher values of all the parameters are associated to the uniformly treated sample (green boxes). The nonuniformly treated sample (b) resulted in maximum values  $V_{oc}=613\text{mV}$ ,  $J_{sc}=16\text{ (mA/cm}^2\text{)}$ ,  $FF=59.57\%$  and  $\eta=5.8\%$ . The uniformly treated sample (a),  $V_{oc}=748\text{mV}$ ,  $J_{sc}=24.87\text{ (mA/cm}^2\text{)}$ ,  $FF=65\%$  and  $\eta=12\%$  were obtained. Almost all the parameters are in the upper 50% of the box meaning that 35

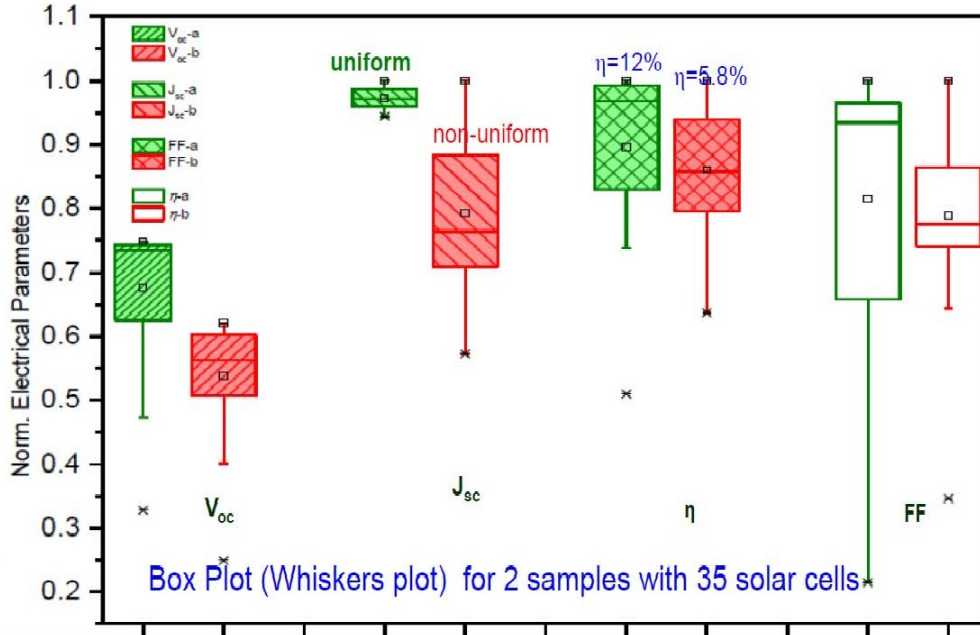


Figure 5: The box plot of normalized electrical parameters obtained for the samples with: a. uniform and b. nonuniform treatment (having residuals).

cells have similar characteristics. Still some of the cells behave differently leading to a scattered data in the box plot. The reason for such different results can be due to surface shunting pathway or measurement tools effects. This will be discussed in the next section. Therefore, uniformly  $CdCl_2$  treated cells behave quite better than the nonuniform ones as the treatment is expected to enlarge the grain boundaries ( $>1.7 \mu m$ ) and show higher  $V_{oc}$  [20].

The sediment  $CdCl_2$  solution which is appears as white tracks on the surface reduce the uniform diffusion of chlorine into CdTe film and the grain boundaries are not expected to passivate well and the devices show poor electrical properties. A good chlorine activation significantly increases the minority carrier lifetime (higher  $J_{sc}$ ) in CdTe and reduces the grain boundary recombination and native defects densities [14]. Then, the photo-current and open circuit voltage increase and the series resistance reduces. Furthermore, such sediment material on the surface of the cell will impede the perfect back contacting.

The Cu diffusion from the Cu/Au contacts cannot passivate such solids and the series resistance,  $R_s$  increases leading to a lower  $FF$ . The average  $R_s$  for sample (a) and (b) is 73.6 and 83.2 ( $\Omega$ ), respectively. This higher  $R_s$  for sample (b) decreases the  $FF$ , consequently. Paudel et. al, suggested that an optimized  $CdCl_2$  treatment for an optimized Cu back contact thickness will increase the cell stability [24].

The roll-over at high voltages in the current-voltage characteristics of the uniformly treated cell is ascribed to the schottky barrier at the back contact which impede the hole transport and limits the current.

This roll-over could be removed by chemically etching the cell surface prior to treatment and metal deposition. This pre-treatment will create  $\text{Te}^+$  surface and passivate the holes at the back region. Probably, despite the uniform treatment, the surface of this sample was having oxidation which was not removed through washing by deionized water.

#### 1.4 Shunting pinholes

The shunting pinhole can form due to the incomplete coalescence of the CdTe grains during deposition, or due to defects in the underlying surface or due to the microscopic contamination on the surface. surface shunting (defective pinhole) between the metallic back and conductive layer at front of the cell during fabrication or electrical characterization. Such shunting pinholes can also form when installing the sample in the thickness profiling system, current-voltage or capacitance-frequency characterization tools which slightly or strongly remove a small part of the surface material and make a big shunting resource. This phenomenon is quite probable in thin film fabrication laboratories and some of them can be seen by the naked eye and some of them are in the range of nanometers. Shunting pinholes are still worse than residues from the nonuniform treatment as they cannot be recovered or cured.

Karpov has quantitatively considered that such defective spots can change the distribution of electrical parameters (e.g.  $R_{sh}$ ,  $V_{oc}$ ) to strongly nonuniform electric potential and extremely reduce the device efficiency [25, 26]. In our samples, the most destructive scratching resource was the characterization set-up when the cells go under contact with pogo pins and needles for the current-voltage or capacitance-frequency measurements. Any external contact to the cells must be done very delicately in order to avoid any local spot, scratch and removal. Anyway, repeating the electrical measurements with the needles will also destruct the back contacts unavoidably. The copper tape can be replaced in such cases but it will also remove a thin layer of the metal when disconnecting. These types of disordered layers cause lateral shunting due to nonuniform topography and morphology [21]. The semiconductor nonuniformities were suggested to be filled by aniline mixtures (polyaniline) or even red-wine by electropolymerization of the aniline monomers (before metallization) which prevents the shunting of the front and back contacts [13, 16]. The current-voltage characteristics of two samples with shunting pinholes and intact, are displayed in Fig. 6. The shunting pinholes of our samples are mostly because of the scratches from the pogo pins used for electrical measurements. Clearly, there is a big difference in the open circuit voltage  $\Delta V_{oc}$  between two samples. This is due to the high recombination rate in the scratched area which is acting as a shunting path through the back contact. The inset represents the schematic circuit including a *weak-diode* that takes into account such pinholes on the surface [14].

As it is deduced from the curve, the intact sample with no shunting defect has  $V_{oc}=746$  mV while the shunted one has  $V_{oc}=328$  mV. The  $\Delta V_{oc}$  of the damaged sample lowers the  $FF$  from 33.21% to 64.37%

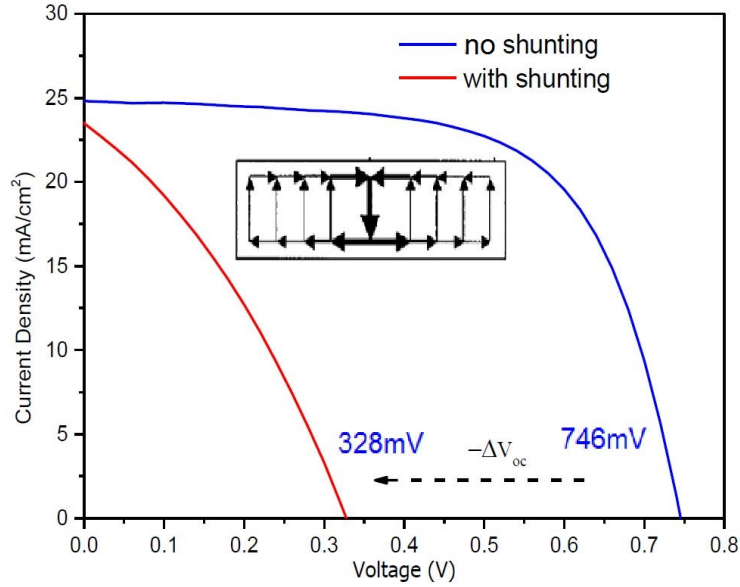


Figure 6: The current-voltage characteristics of the cells with shunting pinholes and intact cells. The inset is the circuit of the shunting pathway due to pinholes which rob the current leading to  $-\Delta V_{oc}$ .

and the efficiency from 11.90% to 2.55%. The current density is almost not affected in this case. However, there are some of the cells which show a quite low current density as well. This could be because of low carrier collection from the scratched cell. In our case, the back contact area is big enough to compensate such disability.

In order to show the shunting areas with high recombination rate on our samples,  $R_{sh}$  has been shown with a two dimensional diagram in Fig. 7. The  $xy$  axes shows the directions and number of the deposited solar cells. The red and blue areas are shunted and intact areas with higher and lower shunt resistances due to low and high recombination paths, respectively.

The distribution of the low resistance elements, i. e., shunts,  $R_{sh}$  shows that the cell has several scratches on the surface. The blue areas show a low  $R_{sh}$  of about 2.5-4.9 ( $k\Omega$ ), while it is about 9.6-10.78 ( $k\Omega$ ) for the red areas. The weak diodes cause to lower  $V_{oc}$  leading to lower the local efficiency. Extending these damages to the panel scale where many of such small modules are integrated altogether makes these disorders much more important.

Note that the disorders or shunts are also created under bias, long term illumination or temperature fluctuations [27] and different analysis methods are needed to consider the influence of such failure mechanisms [28]. The systematic studies on the shunt resources by laser scribing as an intentional way to scratch the cell revealed that the local spots can cause variation in the electric field in a weak diode, accelerate the defect creation by excessive local carrier concentration or local corrosion and as a result degrade the cell in

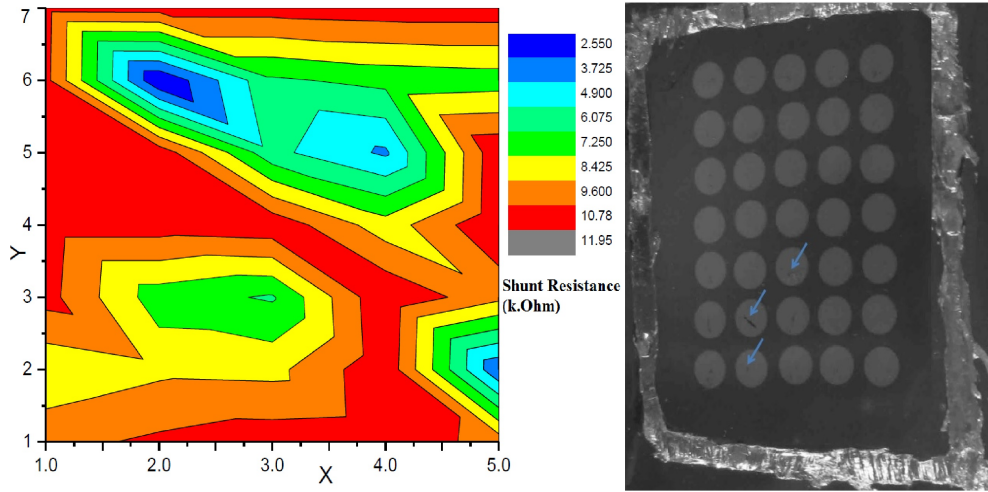


Figure 7: Contour-plot for the shunt resistance of the sample including shunting pinholes on the surface. The blue areas have the lowest  $R_{sh}$  due to pinholes while the red areas are intact cells.

such way that cannot be recovered by light soaking or isolating the shunting areas [29].

We only considered the surface shunts and pinholes due to contacted pogopins during J-V characterization. Delicately contacting these pins to the cell will not damage the surface. However, strong pressure has been considered to have reversible dependence on the solar cell parameters expected from the piezoelectric properties of CdS window layer [30]. For example,  $V_{oc}$  decreases with increasing the pressure as the piezoelectric charge density induces the voltage across the cell.

The effect of surface erosion on the efficiency of 35 solar cells is shown with the aid of three-dimensional topography in Fig. 8. The lower efficiencies appear as downward cones in the relevant positions. The lowest efficiencies (3-5 %) in blue colour are due to scratches while the red areas represent the safe cells with about 10-12% of efficiency. Clearly, the most part of the cell exhibits high efficiency. Further studies on the disordered surfaces including scratch or local spots can be done by lock-in thermography of thin film CdTe/CdS solar cells. The spatial variations on the device surface influences on the local characteristics. A bright spot on the back contact represents a weak diode with  $V_{oc}$  lower than the other parts [31].

At this time, there is not a solution to recover the scratched pinholes. However, the laser scribing is proposed to isolate and cut the scratched area from the rest of the cell [21]. This technique can also leave metallic particles and removal dust in the scribed area leading to new shunting pinholes. Therefore, care must be done to avoid the occurrence of such local disorders. The solar panels are usually protected by a glass frame in order to avoid such physical problems which can also come from environmental impacts. There is a debate on how to get rid of the pinholes formation during the different materials processing.

Some of the laboratories, use instead of a mechanical contact graphite-Hg paste, or silver paste that of

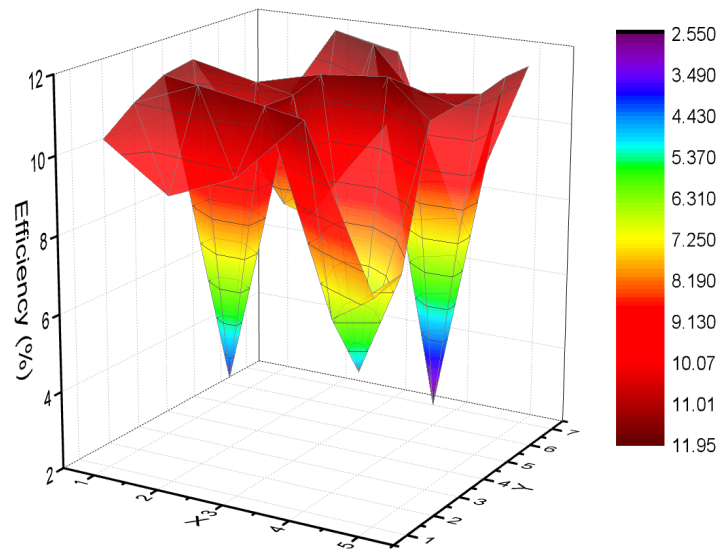


Figure 8: The three dimensional diagram of conversion efficiency for the sample with 35 solar cells deposited in  $7 \times 5$  positions. The red and blue areas have the highest and lowest efficiency, respectively. The blue areas are with scratched surfaces.

course can result in some other issue related to the different materials interfaces. The alternative solution for such issues is that before finishing the device, the surface of the sample is covered with a conductive polymer in order to protect the metallic back contact from the extra diffusion into the semiconductor and TCO layer. The concept of self-healing was introduced for such issues [29].

Roussillon et al., have proposed the concept of photovoltaic self-healing that selectively blocks the effects of lateral nonuniformities in thin-film semiconductor structures. The nonuniformity modulates the surface photovoltage distribution. When exposed to light and immersed in a proper electrolyte, this distribution will generate laterally nonuniform electrochemical reactions. Such treatments result in a nonuniform interfacial layer that balances the original nonuniformity. In Fig. 9 the open-circuit electric potential variations of CdS/CdTe device with the electrolyte treated and untreated cases are illustrated.

## 1.5 Conclusion of CdTe fabrication

Two physical problems effective on the electrical parameters of R.F. sputtered CdS/CdTe solar cells were considered; the nonuniform CdCl<sub>2</sub> treatment and surface scratches. Each issue is a common problem in thin film deposition laboratories and disregarding them leads to quite low performance and dismantle the sample. The electrical characterization of the cells with nonuniform CdCl<sub>2</sub> treatment, which appears as white tracks on cell surface, reduces the low efficiency down to 4-5%. This originates arises from both lower  $J_{sc}$  and  $V_{oc}$  as in nonuniform treatment, CdCl<sub>2</sub> cannot diffuse perfectly into the thin film structure

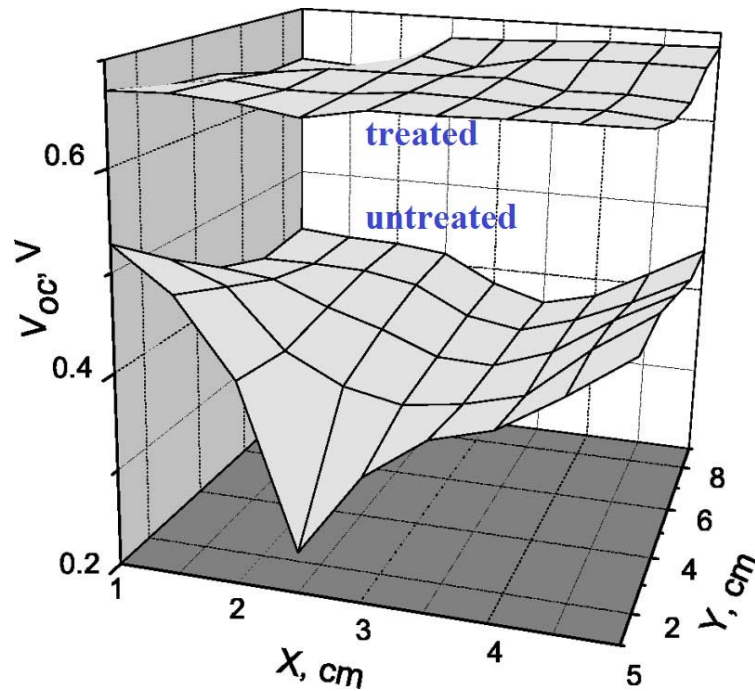


Figure 9: The three dimensional diagram of open-circuit voltage for the treated and not-treated CdTe PV Devices.

and increase the grain size. The box plot of the electrical parameters shows that the lower  $J_{sc}$  and  $V_{oc}$ ,  $FF$  and  $\eta$  are obtained for the nonuniformly treated sample.

The other issue is the surface defective pinholes and shunting pinholes which rob the current and lead to 3-5% efficiency. We presented the efficiency of this sample with 35 cells in 3D to show how the scratched areas have lower efficiency than the safe ones. This low performance is mostly determined by  $V_{oc}$  since the recombination rate increases in those spots. The 2D topography of the  $R_s$  and  $\eta$  for the shunted cells reveals that the local spots are low shunt resistance areas 9.6-10.78 ( $k.\Omega$ ). This requires that the electrical needles to be contacted the cell surface delicately. Electropolymerization of an organic material on the semiconductor CdTe surface before back contacting can avoid shunting pinholes.

In the next chapter we will provide an method to modify the surface of the device in order to support the  $CdCl_2$  post-growth treatment as well as pinhole surpassing before back contacting the device.

## Chapter II

### Electrical Characterization of CdTe Thin Film Devices

The  $\text{CdCl}_2$  post-growth treatment and annealing is a well-known step through the fabrication of efficient CdTe devices. This process can improve the morphology of the thin film, provide a better crystallinity and increase the open circuit voltage of the device. In this chapter we examine all these characteristics through electrical characterization and microscopy techniques. Moreover, we will propose a simple method to enhance the surface properties of the semiconductor where the micro nonuniformities are level out. In this regard, four set of R.F. sputtered CdS/CdTe thin film solar cells are activated through comparable treatment procedures. Two samples were rinsed into deionized water for an hour before  $\text{CdCl}_2$  treatment and then activated in Ar or air ambient. The two others are normally treated and activated in Ar and air, respectively.

The influence of water rinsing and annealing ambient on the electrical and optical properties of the films are investigated by current-voltage, field emission scanning electron microscope, X-ray diffraction and optical transmission spectroscopy. We examined the water rinse as a cheap and simple pre-treatment step to modify the semiconductor surface and to obtain quality device. In this way, the fill factor of the cells which were rinsed into water before  $\text{CdCl}_2$  activation were comparable with the one prepared without rinsing. There is a challenge between the effect of water and Ar on the electrical parameters of the cells. Water rinsed cells annealed in Ar showed a better properties than the one that received no water rinsing. The higher shunt resistance of the rinsed samples represents that water rinse could passivate the surface defects and pinholes. The grains size, phase and band gap of the thin films are extracted, analysed and compared with the as-deposited devices. In other experiment, CdTe thin films with  $2.1\mu\text{m}$  thickness were grown by the rf magnetron sputtering on top of the commercially available TCO deposited glass substrates under two different mixtures of Ar and  $\text{O}_2$ . The concentration of  $\text{O}_2$  was kept at 0%, 1% and 5%. X-ray diffraction shows a transition of cubic to hexagonal crystalline phase as the oxygen content increases from 0 to 5%. The measurements obtained larger band gaps and grain sizes for the films with higher oxygen content.

## 2.1 Electrical characterization applications

The pre-treatment of the semiconductor surface in order to level out the surface nonuniformities before CdCl<sub>2</sub> activation and annealing the thin films is a critical step to improve the electrical characteristics and stability of CdTe solar cells [13]. Karpov et al., suggested that chemical etching can improve the hole passivation at the back contact and electrochemical deposition of a conductive layer can protect the cell from pinhole's shunting [14]. On the other hand, the high-temperature techniques such as vapour transport deposition or close spaced sublimation have larger grain sizes than R.F. sputtered devices. Therefore, CdCl<sub>2</sub> activation is a critical step for sputtered cells to increase the typical CdTe grain sizes.

Although, CdCl<sub>2</sub> treatment in air ambient at high temperature is technologically known to affect the grain size and morphology of the film, but the physics of such mechanism has not been well understood yet. Although, standard annealing in air ambient generally leads to improved electrical characteristics [26], but annealing in Ar, N<sub>2</sub> ambient are also effective on the fill factor of the devices [20]. The fill factor of the cells treated in Ar ambient was improved by 3-4% likely due to better surface morphology and lower series resistance.

The scanning electron microscopy (SEM) of such devices shows that the surface morphology and grain sizes are quite bigger after CdCl<sub>2</sub> treatment and annealing [32]. The X-ray Diffraction (XRD) analysis after CdCl<sub>2</sub> treatment and annealed in air ambient showed a comparable changes in structure growth orientation [22]. The optical transmission spectroscopy reminds that the band gap of treated films are lower than as-deposited ones [20]. We present our studies on the effect of deionized water (DIW) rinsed samples annealed in air or Ar ambient. All four set of samples are optically and electrically characterized by current density-voltage (J-V), SEM, XRD and transmission spectroscopy. Then, the performance parameters, surface characteristics, morphology and optical parameters are extracted from the films prepared through different treatment and annealing procedures. The water rinsing proposed here can be the easiest and cheapest way to level out the surface nonuniformities and defect passivation before contact metallization.

## 2.2 Surface modification: nonuniformity effects

It was already proposed that the micrononuniformities on thin-film photovoltaics are the key factors of the large device area and the presence of potential barriers in the grain boundaries for polycrystalline films and in device junctions. The nonuniformity's effects in the terms of random microdiodes connected in parallel through a resistive electrode has been already proposed and modelled [14]. The microdiodes of low open circuit voltages are shown to affect macroscopically large regions. They strongly reduce the device performance and induce its nonuniform degradation in several different modes. The reduced open circuit voltage and high shunt resistance that we discussed about them in Chapter 1 could be created because of this

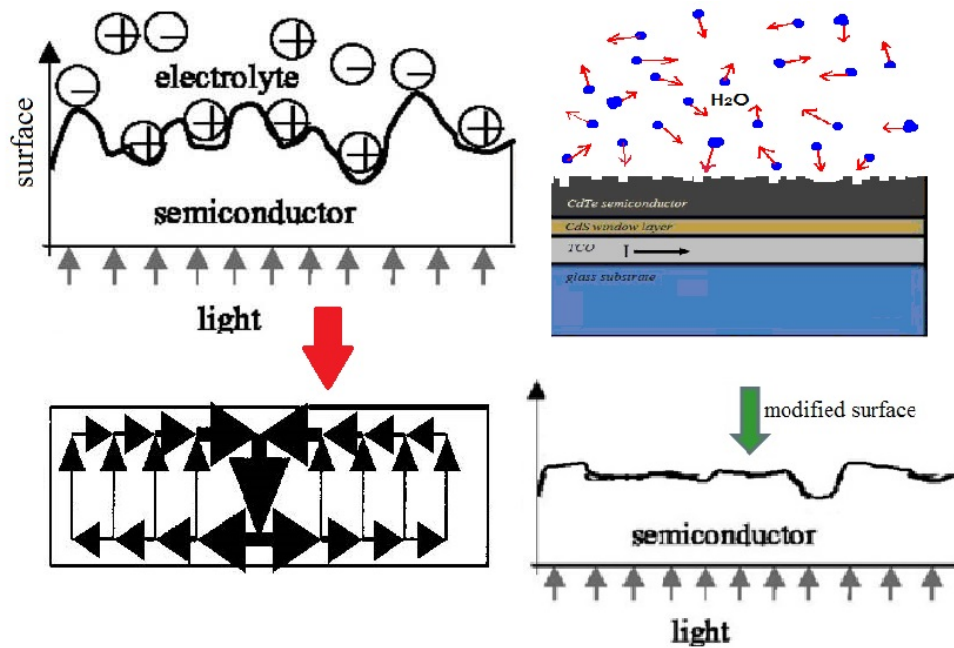


Figure 10: The nonuniformity on the surface of the CdTe film and resulted shunting pathway through the weak diode (large vertical arrow).

nonuniformities. In Fig. 10, these surface nonuniformities and the shunting results are shown schematically.

In this chapter we consider the surface modification methods and propose the deionized water as an potentially simple candidate. Four set of CdS/CdTe samples were R.F. sputtered onto a Pilkington TEC15 substrate with a high resistivity buffer layer. CdS layer of 60 nm thickness was chosen as heterojunction partner (window) of CdTe cells with 2.1  $\mu\text{m}$  thickness. Two of as-deposited samples were dipped into deionized water for an hour before treatment in order to treat the surface. Then, all the samples were CdCl<sub>2</sub> treated by dropping the solution on the cell surface. The rinsed samples were annealed at high temperature of 387 °C in Ar, (c), and in air ambient (a), respectively. The same procedure for non-rinsed samples ((d) and (b)) was repeated.

In another case the effect of Oxygen incorporation into the deposition process of CdTe layer is considered and three samples with 1%, 5% Oxygen as well as a Oxygen-free are fabricated and characterized by the above mentioned characterization techniques.

All the samples were Cu/Au back-contacted with 32 nm Cu, 20 nm Au in Bell-jar thermal evaporation system through a mask. Finally, the samples were heated for 45 minutes at 150 °C in air ambient Cu diffusion into CdTe structure [20]. At least 25 dot cells (with cell area of 0.062 cm<sup>2</sup>) were prepared on each sample. The finished solar cells were electrically characterized under an AM1.5 illumination by using an Oriel xenon solar simulator at room temperature. A part of sample (b) was taken as the as-deposited

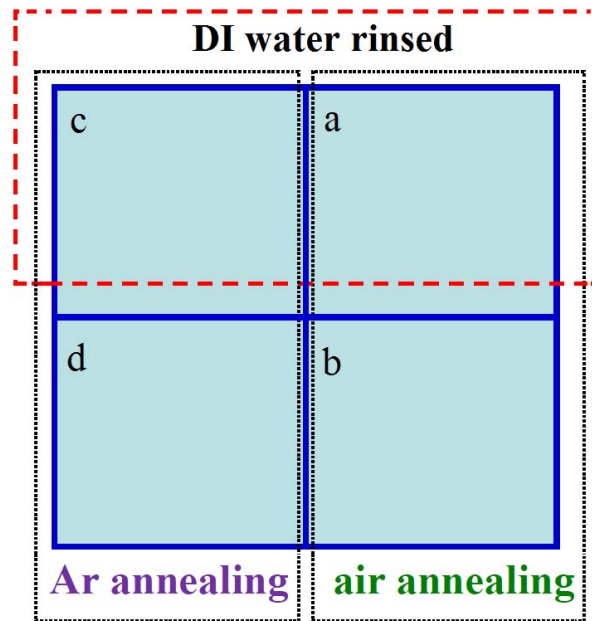


Figure 11: Four set of CdS/CdTe thin films prepared through different treatment and annealing procedure; (a): DIW rinsed before CdCl<sub>2</sub> treatment annealed in air, (c): DIW rinsed before CdCl<sub>2</sub> treatment annealed in Ar, (d): normally treated and annealed in Ar, (b). normally treated and annealed in air (reference).

and along with the other samples were all characterized by XRD using a Rigaku Ultima III high resolution instrument with Cu-K1 line ( $\lambda=0.154$  nm) at 45 kV and 40 mA. The detection angle is in the range of  $20^{\circ}$ - $70^{\circ}$ . The SEM micrographs were taken using a JEOL JSM-7500F scanning electron microscope with 5 KV accelerating voltage and a  $20 \mu\text{A}$  current. The transmission spectra were taken by Broadband (UV to mid-IR) transient absorption spectroscopy.

### 2.3 Current-voltage characterization (DIW rinse)

The electrical parameters, grains size growth, plane phase and optical parameters of all the samples have been studied by four different techniques and compared with the standard CdCl<sub>2</sub> treated sample (b) and an as-deposited cell taken from a piece of sample (b). Fig. 11 shows schematic of our treatment procedure on each sample; (a): was rinsed into DIW for an hour before standard CdCl<sub>2</sub> treatment and then it was annealed in air ambient at  $387^{\circ}\text{C}$ ; (b): is our reference sample prepared in standard way without water rinse but annealing in air ambient; (c): was rinsed into DIW but annealed in Ar and; (d): was prepared without water rinse but annealed in Ar ambient. It should be reminded that CdCl<sub>2</sub> treatment was handled by a few drops of solution on bare CdTe layer which is still a critical step in obtaining an efficient device.

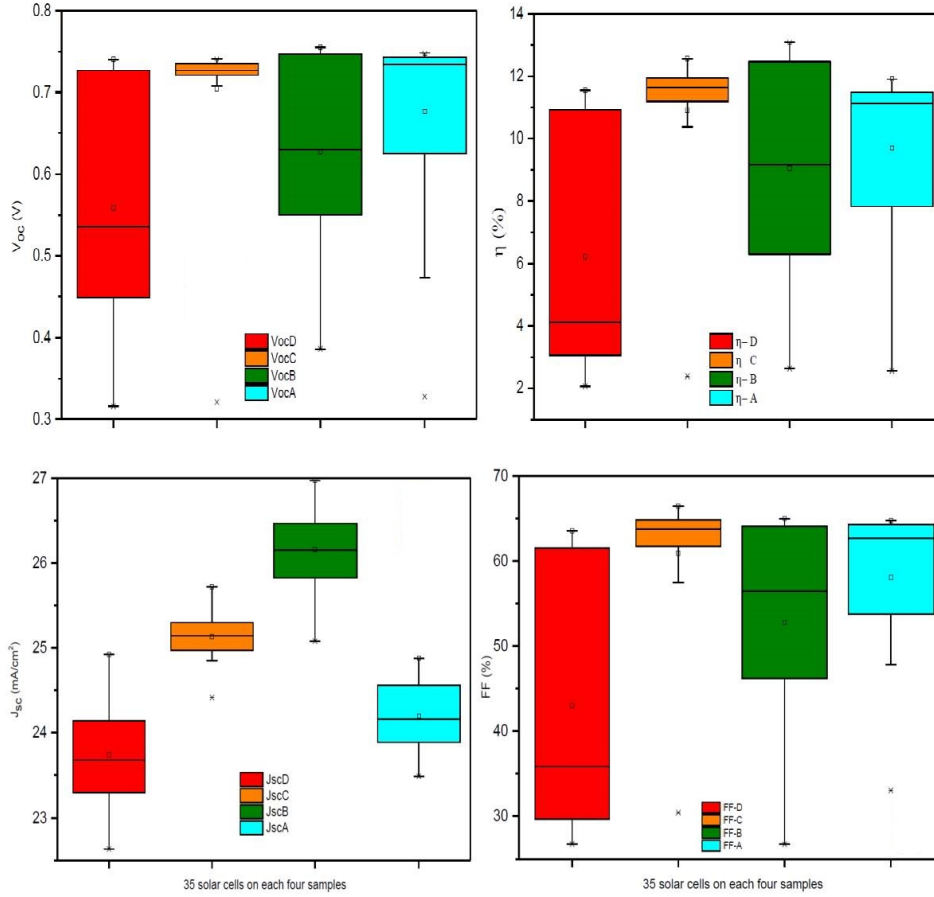


Figure 12: The box plots of normalized electrical parameters obtained for all the samples.

Covering the surface with a few drops of saturated solution must be done by experience in order to avoid any sediment on the surface [33].

The box plots in Fig. 12 compare the electrical parameters of all the samples. The best efficiency  $\eta=13.09\%$  was obtained for the reference sample, (b), prepared in normal way without water rinsing but annealed in air. This higher efficiency is attributed to the effect of  $\text{CdCl}_2$  activation on the CdTe based solar cells [24]. Chloride activation induces crystal regrowth and increases the grain sizes [22]. Therefore, for sample (b) we obtained the highest open-circuit voltage of  $V_{oc}=755\text{ mV}$  and short-circuit current density of  $J_{sc}=26.74\text{ mA/cm}^2$  with the maximum fill factor of  $FF=66.44\%$ . In contrary to such good properties, sample (d) which was annealed in Ar has the worse characteristics.

Rejon et al. have reported that in Ar activated devices have high series resistance, and low shunt resistances. The high series resistance is associated to the low quality devices [34]. In fact, annealing ambient will change the surface properties as we will consider by SEM images on our devices later on. The

Table 1: The best performance parameters of the four set of samples.

activation procedure	$V_{oc}$ (mV)	$J_{sc}$ (mA/cm <sup>2</sup> )	$FF$ (%)	$\eta$ (%)	$R_{sh}$ (k $\Omega$ )	$R_s$ ( $\Omega$ )
b (air,reference)	<b>755</b>	<b>26.74</b>	64.37	<b>13.09</b>	3	83.2
d (Ar)	734	24.89	63.21	11.54	0.38	235.5
a (DIW+air)	746	24.81	64.37	11.90	<b>16.12</b>	73.6
c (DIW+Ar)	739	25.57	<b>66.44</b>	12.56	8.16	<b>71.6</b>

low shunt resistance means that the recombination current is too high which reduces the performance of the cell by its impact on the open circuit voltage. For sample (d), we obtained the highest  $R_s=83.2$  ( $\Omega$ ) and lowest  $R_{sh}=0.38$  ( $\Omega$ ) Sample (a) which was rinsed into DIW and annealed in air ambient showed a remarkable shunt resistance of  $R_{sh}=16$  ( $\Omega$ ) among the other four set. We may relate this to the effects of water on the surface of the as-deposited sample. The enhanced surface will reduce the recombination rate at the interface with back contact. From the Table 1, high shunt resistance and low series resistance represent that the nonuniformities on the semiconductor surface are level out by water rinsing (sample (a,c)). This reduces the defective shunting pathways and smoothes the cell surface before annealing [13]. Further analysis has been done by XRD measurements.

Another interesting observation in our experiments was the challenge between the effects of DIW rinsing and annealing ambient (Ar and air). This is the case between samples (a) and (c) which were rinsed into DIW before CdCl<sub>2</sub> but then sample (a) was annealed in air and sample (c) was annealed in Ar ambient. Although annealing in Ar ambient can decrease the efficiency, DIW rinse can reduce this effect. This might be due to the smoother surface of DIW rinsed sample on which neutral Ar atoms cannot accumulate and localize into film structure since Ar atoms cannot interact with the other materials and they are just placed through the roughness of the film surface and create the voids in the early bulk layer and surface of the cell. This is why  $R_{sh,d}=16$  (k $\Omega$ ) is the highest. Another assumption is that water rinse could passivate the pinholes or defects on the surface and reduce the shunt resistance. In contrary,  $R_{sh,c}=8.1$ (k $\Omega$ ) and the lowest value among the other samples indicating that the cell has a better quality. Clearly, the lower series resistance leads to the higher fill factor and we obtained the maximum  $FF=66.44$  % as expected.

Annealing in Ar ambient is preferred to air ambient when preparing efficient devices in order to avoid the dust and impurities from air which can penetrate into the film structure. However, it seems that air ambient is more influential on the performance. This is probably due to the low O<sub>2</sub> percentage in the air components. A very low percentage of Oxygen can increase the band gap of CdS window layer and increase the quantum efficiency of the device [35].

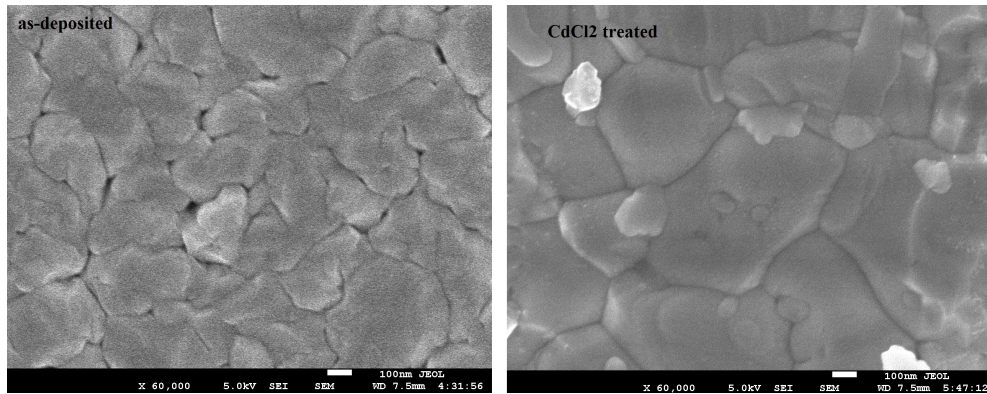


Figure 13: The SEM images of as-deposited and  $\text{CdCl}_2$  activated thin films. The influence of the treatment on the grain sizes is clear. The images were taken at 100 nm.

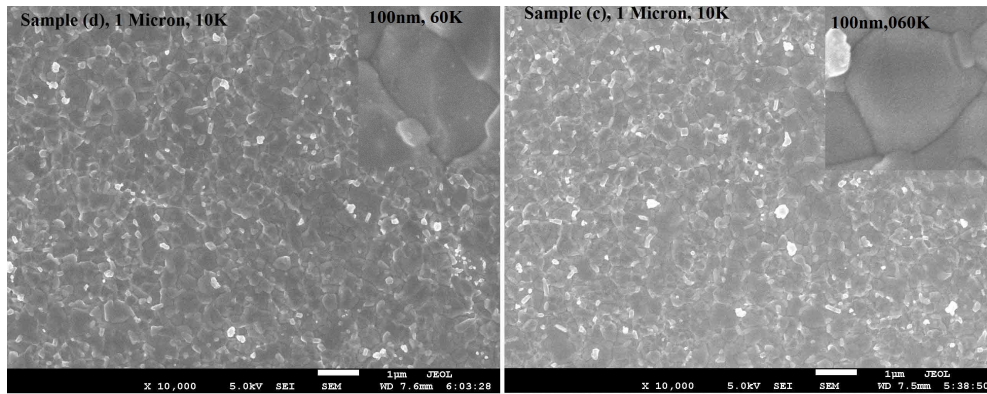


Figure 14: The SEM images of sample (c) and (d) both annealed in Ar (sample (c) was DIW-rinsed too) at  $1 \mu\text{m}$ , 30K. The inset; SEM images either samples in 100 nm, 60K zoom in. DIW rinsed cell shows more uniform treatment visible as a transparent light layer throughout the film.

## 2.4 SEM characterization (DIW rinse)

The surface morphology of the thin films was considered by SEM. Also, an as-deposited piece of sample (b) was characterized before  $\text{CdCl}_2$  treatment and annealing as the reference sample. First, we consider the grain boundaries of sample (c) and as-deposited one in order to show how the treatment and annealing changed the morphology of our devices. Fig. 13 shows the plan view of the SEM images taken at 100 nm. The influence of the  $\text{CdCl}_2$  treatment and annealing on the grain sizes is clear. The annealing can reduce the lattice mismatch at the junction and optimize the Chlorine diffusion into the grain boundaries and passivate them. Such process will increase the electrons recombination lifetime by reducing the shunt resistance which

in turn increases the performance of the device [22].

From Table 1, we see that there is a challenge on the effect of DIW rinse and in Ar annealing. Therefore, hereafter, we only consider this issue in order to avoid any repeated analysis and to further understand the novelty of the latter phenomenon. Thus, the effects of DIW rinse, CdCl<sub>2</sub> treatment and annealing in Ar ambient, sample (c) and (d) were investigated. In Fig. 14, the challenge between DIW rinse effect and annealing in Ar effect on the morphology of the thin films has been displayed. The images were taken at 1  $\mu\text{m}$  in order to have a wider view on the film morphology.

The surface of DIW rinsed sample (c) shows a uniform treatment containing transparent white particles throughout the film representing that the Cl or water molecules have covered the CdTe surface. The contaminants, however, make the facets slightly not clear. Such morphology have been observed and verified on the different positions of the cells. Inset of Fig. 14 clearly shows the grain sizes at 100 nm. As SEM images were taken after activation step, the resolution of the grain boundaries is not high enough. We extracted the average grain sizes by *ImageJ* software and *Excel* calculator. ImageJ is free software to count and analyse the optical images [36]. For sample (c) and (d) the average grain sizes were obtained about 1.04 and 1.00  $\mu\text{m}$ , respectively. The distribution of the grain sizes is almost uniform. However, the DIW samples still show brighter images meaning that the DIW effect is quite deep to interior of the grains or it helps the better diffusion of Chlorine into the film structure.

Since the grain sizes of the rinsed samples (a,c) are not bigger than the normally treated ones, we should attribute their high shunting resistance to the filled pinholes and defects by water molecules. It could also be said that sample (c) is showing some bimodal type growth with some of the larger grains. Nevertheless, this observation requires a systematic approval and further investigation to verify if it is because of DIW rinse effect. Our assumption is that dipole molecules of water with kinetic energy to move and rotate in the solution can reduce the roughness of the surface and reduce the probability of Ar atoms localization. The other possibility is that, the water molecules will fill the nonuniformity of the surface and impede the Cu atoms to diffuse into the absorber layer. Then, we obtain lower series resistances. Nevertheless, this will reduce the performance as Cu diffusion will align the Schottky barrier at the back region and assist the passivation of the holes.

Also, similar to the rinsing process in order to remove the HCl solution in sublimation methods, the DIW can create Te<sup>+</sup> on the surface or additional acceptors which are diffused into CdTe layer, shift the holes Fermi level and increase the  $V_{oc}$  [33]. According to the theoretical calculations, defects can partly be passivated by Cl, S, and O atoms where the most perfect passivation is achieved by Cl addition through CdCl<sub>2</sub> activation. Also, Cl and Cu co-passivation has been suggested to obtain efficient devices [35]. Roussillon et al., have suggested that the illumination and immersion of the cell (surface) into a proper electrolyte as a pre-treatment step levels out the original surface nonuniformity and will improve the device efficiency from 1-3 % to 11-12 % [13]. Also, Oxygen of water can reduce diffusion of Cu back contact at grain boundaries,

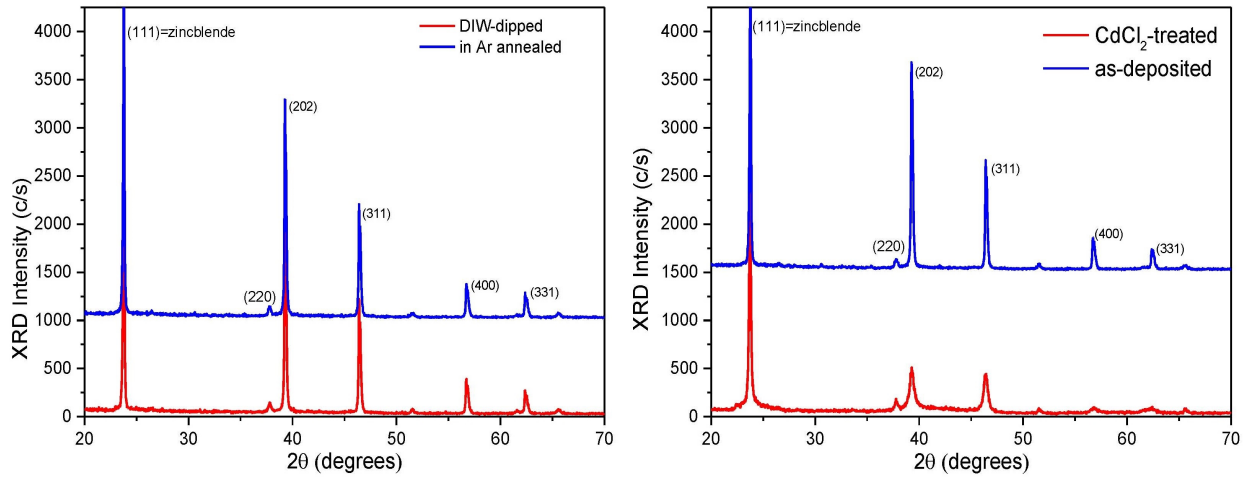


Figure 15: The XRD patterns of our as-deposited and treated CdTe films. Both films show zincblende phase with (1 1 1) plane with less oriented structure for as-deposited cell. The XRD patterns of DIW rinsed and in Ar annealed CdTe films. Both samples show zincblende phase as the main plane. Water rinsing could not be such effective on the phase transmission.

minimize the shunts formation of Cu and decrease the degradation rate. Further accelerated lifetime testing is required to analyse the degradation of the DIW pre-treated devices.

## 2.5 XRD characterization (DIW rinse)

The X-ray diffraction analysis can better show the orientation and crystallinity of CdTe films. Fig. 15 shows the XRD patterns of as-deposited and CdCl<sub>2</sub> treated CdTe thin films as a function of the diffraction (Bragg) angle  $\theta$ . The chloride treated and annealed films obtained higher diffraction peak intensities indicating improvement in crystalline quality. The treated device exhibited maximum peak intensity of 3831 c/s at  $2\theta=23.75^\circ$  associated with (1 1 1) Miller indices which is relevant to zincblende phase [37]. However, they are not the main phase in the XRD intensities. At almost same degree of  $23.73^\circ$ , the as-deposited one has a maximum intensity of 2593 c/s.

The treated film shows also some weaker peaks at higher  $2\theta$  degrees which were not detected for as-deposited cell. This indicates that the treated film contains some grains grown with different orientation which are different than the zincblende phase. For example, the treated and as-deposited cell showed a smaller peak at  $2\theta=39.26^\circ$  and  $39.29^\circ$  relevant to (2 2 0) or (2 0 2) which is cubic phase. but not zincblende. Also, there are some weak peaks at higher degrees  $46.39^\circ$ ,  $56.78^\circ$  and  $63.37^\circ$  with (3 1 1), (4 0 0) and (3 3 1) which all indicate the other orientation of cubic phase (not zincblende). The two latter peaks, which are almost missed in the as-deposited film, are probably relevant to the ITO layer (SnO<sub>2</sub>:F) pre-deposited on the glass substrate. This confirms that our treatment step could change the phase of the film structure.

However, a good treatment will lead to almost unique phase with the highest intensity. Lee, reported that the crystallinity can be improved and the phase can be transformed by activation and heat treatment [18].

Fig. 15 compares the XRD results of DIW rinsed and in Ar annealed samples (c) and (d). As was expected, the peaks are competing at several intensities. However, the maximum is still in the first peak at  $2\theta=23.78^\circ$  with 4158 c/s and 4007 c/s for sample (c) and (d), respectively. The strong peak for both samples is zincblende (1 1 1) and there are still some weak peaks with cubic plane. This indicates that both CdTe films treated with different procedure and annealed in Ar were grown with the preferred orientation of the (1 1 1) plane parallel to the substrate. We have not seen a significant phase discrepancy due to water rinsing. Moreover, the grains size can be obtained from the peak width of XRD curves. From Debye-Scherrer formula, the grain size, D, is given by,

$$D = \frac{K\lambda}{\beta\cos(\theta)} \quad (1)$$

where  $\beta$  is the full width at half maximum (FWHM) of the peak,  $\theta$  is the Bragg angle,  $\lambda$  is the wavelength of the X-ray (1.54 nm for our measurements), and K is the Scherrer constant which is taken as 0.94 for the calculations [38]. We obtained FWHM of the peaks for each sample by *Origin pro* software by fitting the peaks with Gaussian curve. The FWHM for as-deposited, treated, (c) and (d) samples are 0.15, 0.13, 0.104 and 0.11, respectively. Thus, at  $2\theta=23.73^\circ$ ,  $23.75^\circ$ ,  $23.76^\circ$  and  $23.76^\circ$  for each sample which are all equal to 0.41 Radian, the grain size is calculated in range of  $D=964-1.92 \mu m$ . This range is in good agreement with the obtained results from the SEM grains. Note that the actual crystallite size given by XRD might be different from the grain size shown in SEM.

## 2.6 Optical characterization (DIW rinse)

The optical properties of all CdTe films were studied by optical transmittance spectroscopy in the range from 500 to 1000 nm. Fig. 16(a) indicates that transmittance spectra of the DIW rinsed in Ar annealed samples were compared with as-deposited and treated ones. There is an abrupt absorption edge around 820 nm for all the samples regardless of the treatment procedure. This is corresponding to CdTe band gap. The absorption edge shifts to smaller wavelength (red-shift) for as-deposited film meaning that treatment and annealing will increase the film band gap. Thus, a lower transmission is obtained for the treated films probably due to the larger grain sizes and increased defects. The DIW rinsed and in Ar annealed films, (c,d), show the average transmission between the reference sample and as-deposited one. This could be due to the reflection from Ar and water complexes inside the film or because of the increased thickness which leads to higher absorption but lower transmission rate. As an important optical property, the band gap,  $E_g$ , of CdTe films can be extracted from the intercept of the absorption spectra,  $(\alpha h\nu)$  plotted versus  $h\nu$  given

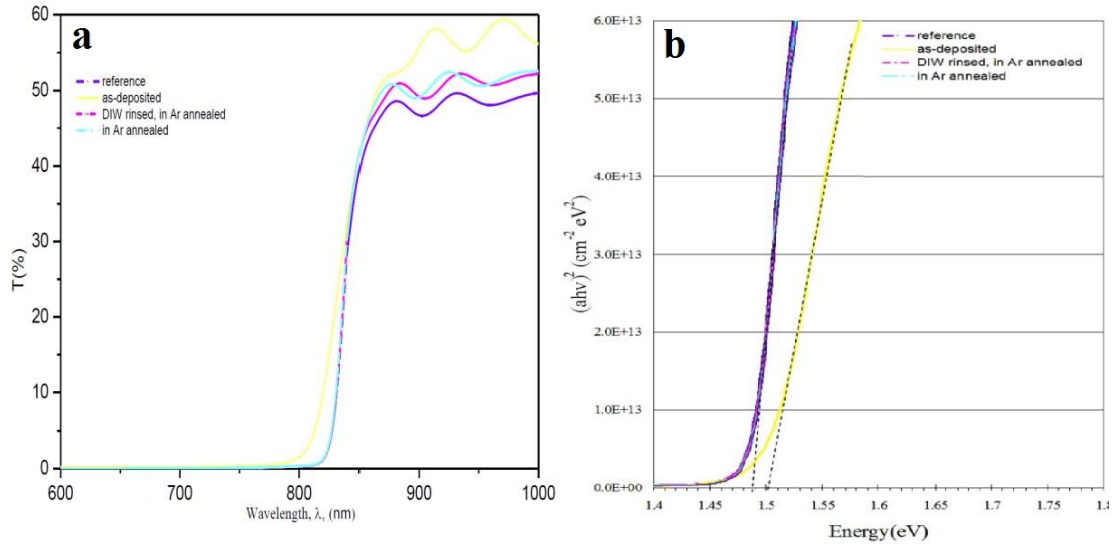


Figure 16: Left: The transmission spectra of CdTe films. All samples show very good absorption by around 820 nm. As-deposited sample has a red-shift to lower wavelengths. Right: The water rinse and in Ar annealed samples show lower absorption. The band gap extracted from transmission diagrams. The treatment reduced the band gap of the device.

by,

$$(\alpha h\nu)^2 = A(h\nu - E_g) \quad (2)$$

where,  $\alpha$  is the optical absorption coefficient,  $h\nu$  is the energy of the incident photons,  $h$  is the Plancks constant and  $A$  is materials constant. From Fig. 16(b), the band gaps of the films are estimated from the initial absorption edge line when  $(\alpha h\nu)=0$ . The absorption coefficient,  $\alpha$ , of the films for various wavelengths ( $\lambda$ ) can be calculated by from the transmittance values by,

$$T(\lambda) = \exp\left(-\frac{\alpha(\lambda)}{d}\right) \quad (3)$$

where  $d$  is the thickness of the film. The intercept of the Fig. 16(b), shows that the band gap of as-deposited cell is 1.5 eV which reduces to 1.49 eV for treated cells. The DIW rinse or annealing in air and Ar did not show much influence on the band gap of the cells. The decrease in band gap as a result of CdCl<sub>2</sub> treatment can be due to increased grains size which was confirmed by XRD and SEM characterizations.

## 2.7 Oxygenation of CdTe layer

The incorporation of Oxygen into CdS/CdTe thin film solar cells through deposition process has been suggested to improve the electrical parameters or material characteristic. NREL have reported the research strategies toward improving thin film CdTe photovoltaics beyond 20% efficiency. Their theoretical studies suggest much of the improvement associated with oxygen, chlorine, and copper is due to the interaction of these species with intrinsic defects related to Cd and Te vacancies, interstitials, and anti-sites in the bulk as well as within the grain boundary regions [39]. The beneficial effects of Oxygenation has been still under debate from the different aspects. It was found that deposition of CdTe layer in partially Oxygen ambient (Ar:O<sub>2</sub>) reduces the grain size of the film in terms of reduced nucleation rate [40]. But it also depends strongly on the substrate and after treatment annealing temperature. The CdS film deposited in the presence of oxygen can be a better choice for (CdTe) polycrystalline devices.

The Oxygen incorporation can transform the crystallinity from cubic to hexagonal while it amorphizes the phase for the higher contents [41]. Moreover, O<sub>2</sub> can improve the energy conversion efficiency through enhanced open circuit voltage from 780 to 812 mV [38, 42]. This is while, higher Oxygen content can increase the resistivity of the device and lower the performance due to formation of shallow acceptor complexes that oxygen forms with the cadmium vacancies [43]. This effect is probably due to the generation of nonradiative defects produced by the oxygen concentration, which are competing for the dominance with more efficiency than the radiative processes [44]. In fact, lower oxygen content decreases the resistivity whereas higher oxygen content increase the resistivity of the films up to 6 orders of magnitude. Alejo et al., reported a decreased (to 1.40 eV) and increased band gap (to about 3 eV) for the low (0.3 %) and high (0.6%) content of O<sub>2</sub> in the CdTe films. Oxygen acts as additional acceptor density in the CdTe layer which may [45]. However, there is not a clear relationship between the optical energy band gap and the oxygen content.

Still many inconsistency is observed between the results of the above investigations and the role of O<sub>2</sub> has to be clarified for different growth conditions and techniques. Using density functional theory calculation, Feng et al., have shown that when a Te atom is substituted by an O atom, the deep gap states can be shifted toward the valence band, making the site no longer a harmful non-radiative recombination centre [46]. In fact Oxygen atoms prefer to substitute the Te atoms and induce significant lattice relaxation due to their smaller atomic size. To our knowledge, just a few researches have been carried out about the Oxygenated CdTe deposited with R.F. sputtering technique. Since, the critical parameters of substrate temperature, pressures of the sputtering and reactive gas are more controllable in R.F. sputtering, we deposited several of Oxygenated and Oxygen-free CdTe thin film solar cells. Moreover, the effect of Chlorine post-treatment will be examined on all the devices. Emziane et al., reported that the concentration of oxygen in CdTe is further increased when the sample receive a post growth heat treatment of CdCl<sub>2</sub> compared to the samples without CdCl<sub>2</sub> treatment [42].

Our analysis include the Scanning Electron Microscopy (SEM), X-ray Diffraction (XRD) on the as-deposited and chlorine post-treated devices. Three set of CdS/CdTe samples were R.F. sputtered onto a Pilkington TEC15 substrate having Transparent Conductive Oxide (TCO) layer. CdS layer of 100 nm thickness was chosen as n-type window layer for CdTe p-type absorber layer (2.1  $\mu\text{m}$ ). The first set of the samples were deposited in Ar ambient ( $\text{O}_2$ -free), while the second and third set were grown at 1%  $\text{O}_2$  mixed with 99 % Ar and 5%  $\text{O}_2$  (95% Ar) mixed deposition ambient where both CdS and CdTe layers were Oxygenated.

## 2.8 SEM characterization (Oxygenated CdTe)

For comparison, the oxygen incorporated CdTe thin films were analysed by SEM micrographs taken on the as-deposited and  $\text{CdCl}_2$  treated devices. Fig. 17 displays the SEM images of CdTe films deposited under three different ambients:  $\text{O}_2$ -free, (100% Ar), mixed ambients of Ar and  $\text{O}_2$  including 1% and 5%  $\text{O}_2$ . Increasing the  $\text{O}_2$  content decreases the grain sizes. The grain size of the cell with 1%  $\text{O}_2$  did not show a big difference comparing with the  $\text{O}_2$ -free one. Instead, 5%  $\text{O}_2$  could reduce the grain sizes effectively. However, in some parts of the sample with 5%  $\text{O}_2$  there are some big grains which are probably due to a nonuniform treatment or annealing process. The films grown in the absence of  $\text{O}_2$  show a terraced morphology for the grains. It is very clear that the grain size has a significant dependence on  $\text{O}_2$ , as the  $\text{O}_2$  partial pressure increases, the grain size decreases. This type of morphology disappears when the oxygen concentration is increased in the deposition chamber. Grain sizes in the range from 0.8 to 1.5  $\mu\text{m}$  were measured. The smaller grain sizes were observed in the sample grown with the highest oxygen proportion in the CSS chamber [47]. Fig. 17, also shows the SEM images of the  $\text{O}_2$ -free and Oxygenated samples after  $\text{CdCl}_2$  treatment and annealing at high temperature. Note that comparing with upper part of Fig. 17, there is a clear change on the morphology of the devices. The treatment did not cause any obvious changes on the grain sizes of  $\text{O}_2$ -free and 1%  $\text{O}_2$  devices. However, the grains exhibit different features indicating that the nucleation behaviour on these pressures could be very different. Before the chloride heat treatment, the grains have sharp edges and clear facets. After the chloride heat treatment, the grains no longer exhibit sharp edges. The average grain size of these R.F. sputtered CdTe films as a function of the  $\text{O}_2$  content is plotted in Fig. 17. In contrary to the results by Major et al. we obtained bigger grain sizes for R.F. sputtered samples. The discrepancy may be due to the different fabrication parameters such as processing gas ( $\text{N}_2$  vs. 5%  $\text{O}_2$  mixed Ar), substrate temperature (250 C vs. 590 C), and the configuration of the system. As shown in the inset of 5%  $\text{O}_2$  sample (Fig. 17), the grains are extremely large with sharp edges and better uniformity [22]. It was suggested that  $\text{O}_2$  affects the nucleation process resulting in an increase in the number of nucleation sites and attaining denser films. The 5%  $\text{O}_2$  device showed the cluster formation and the grains appear nonhomogenous and nonuniform suggesting that there was a nonuniform nucleation throughout the CdTe surface. For the 5%  $\text{O}_2$  sample, the grains shaped differently and cannot be neatly arranged. Thus, a part of

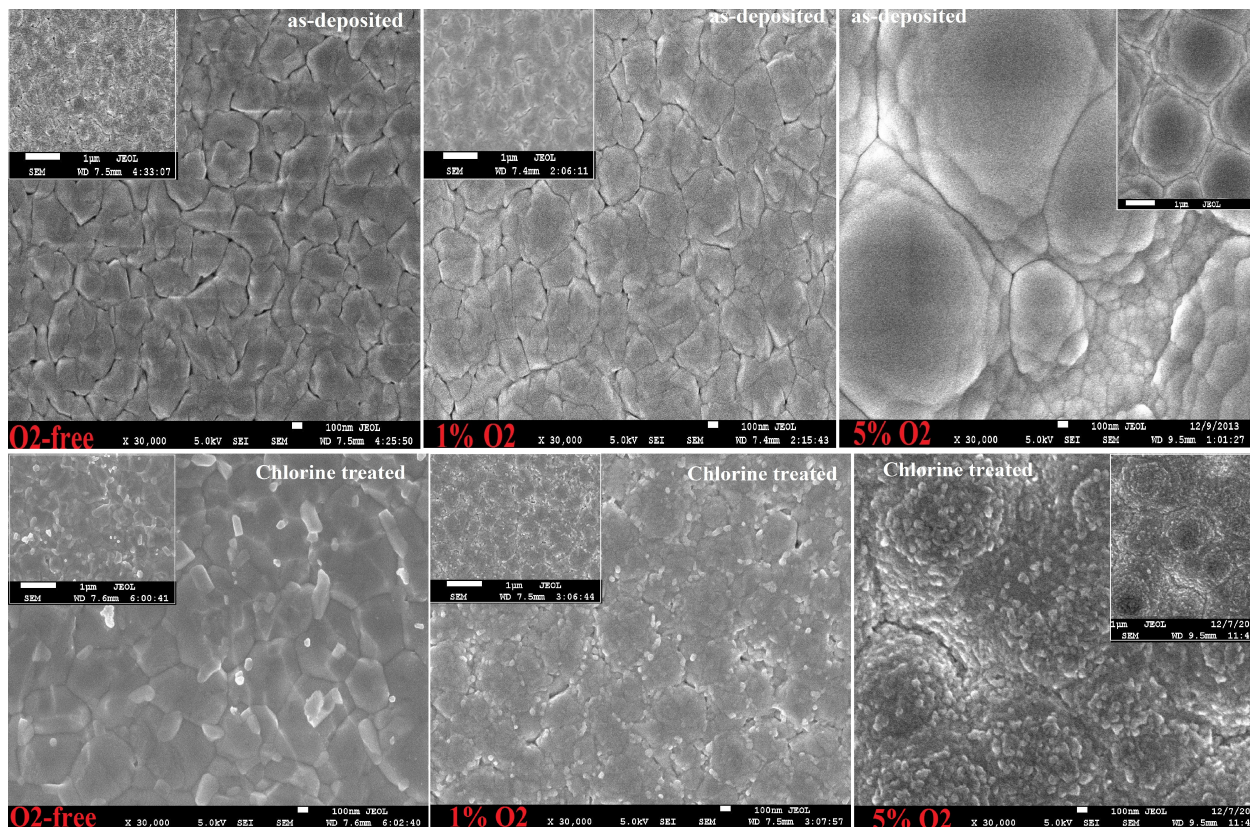


Figure 17: The SEM images taken at 100 nm from the as-deposited (upper) and Chlorine post-treated thin films grown under three different ambients of Ar and Oxygen mixture of: O<sub>2</sub>-free, 1% and 5% O<sub>2</sub>. The insets show the SEM images taken at 1 μm.

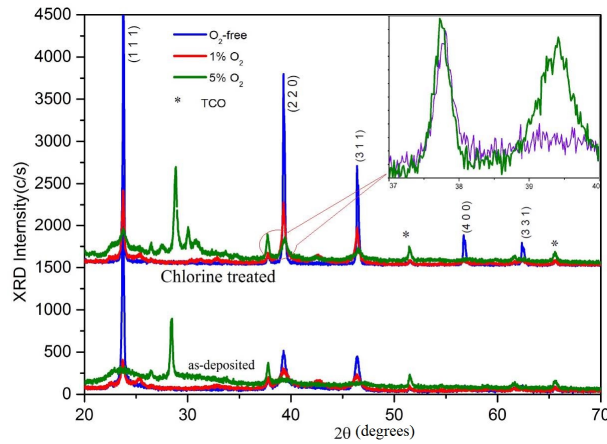


Figure 18: The XRD patterns of as-deposited and CdCl<sub>2</sub> treated CdTe thin films deposited under three different mixture of Ar: O<sub>2</sub>.

the SEM image shows quite smaller grains. However, the surface morphology of this film obtained at  $1\mu m$  (inset) confirms that the grain sizes are quite bigger than the O<sub>2</sub>-free and 1% O<sub>2</sub> samples. The columnar grains of as-deposited samples have regular shapes while they become spherical after CdCl<sub>2</sub> treatment and annealing in Ar. Note that the O<sub>2</sub>-free sample shows some Cubic and hexagonal crystals too.

## 2.9 XRD characterization (Oxygenated CdTe)

The optimal chloride activation that was estimated by SEM analysis is further confirmed by X-ray diffraction. For this, we performed XRD of all the as-deposited and chlorine treated O<sub>2</sub>-free and Oxygenated samples at scan angle ( $2\theta$ ) from 20 to 70° with 10 steps. The diffractogram of all the six samples presented in Fig. 18 shows that the treated films were grown in an obvious orientation except for the 1% O<sub>2</sub> device which has slightly oriented randomly before and after CdCl<sub>2</sub> activation. The XRD intensity of the O<sub>2</sub>-free device is not comparable with the Oxygenated devices neither for the as-deposited nor for chlorine treated. Consistent with the SEM patterns, the grains of the as-deposited O<sub>2</sub>-free device are grown in an obvious cubic phase orientation (1 1 1). The (1 1 1) cubic direction is the preferred orientation of the as-deposited non-oxygenated films. However, O<sub>2</sub>-free chlorine treated device has still some hexagonal phase grains too. Both of as-deposited and chloride treated devices exhibit the zinc blende cubic structure before and after chloride heat treatment while the treatment can induce some hexagonal orientation too. The 1% O<sub>2</sub> obtained no strong preferred growth orientation in either case even though all the diffraction peaks become double intensive after the chloride treatment, indicating improvement in crystalline quality. The very weak peak of 1% O<sub>2</sub> represents that Oxygen is changing the phase of the crystallinity. Generally, The oxygen incorporation

into the lattice sites takes place in a random way without preference in the substitution of the Cd or Te atoms. Therefore, both CdTe hexagonal and cubic crystalline phases coexist in 1% O<sub>2</sub> device.

The phase of the peaks have been indicated regularly in the inset of Fig. 18 (left). These results are in consistency with the reports of Sandoval et al. [48]. As the oxygen content increases from 0% to 5% the relative intensity of the peaks decreases. The XRD peaks of the O<sub>2</sub>-free and 1% O<sub>2</sub> devices are in a same  $2\theta$  angle whereas 5% O<sub>2</sub> shifts the peaks  $5^\circ$  to the right. Nevertheless, the maximum peak of O<sub>2</sub>-free devices (2593 & 4158 c/s) are considerably lower than the one of 1%O<sub>2</sub> (918 & 411 c/s) or 5% O<sub>2</sub> (894 & 1199 c/s). 5% O<sub>2</sub> incorporation significantly reduced the peak so that even chlorine treatment could not strength it significantly. The XRD peak of 5% O<sub>2</sub> device splits into two peaks in the scan range of 37-40 after chloride heat treatment. This peak splitting is the evidence of CdTeO<sub>3</sub> or CdTe<sub>2</sub>O<sub>5</sub> alloying due to Oxygen mixture into CdTe material [49]. The 5% O<sub>2</sub> content has almost changed the crystallinity from Cubic to hexagonal phase. This hexagonal crystallinity phase has not yet been observed in bulk CdTe material, and it has been rarely observed in thin film material [50, 51]. For both 1% and 5% O<sub>2</sub>, the reduced maximum peak intensity of (1 1 1) and appeared shoulders located at the range of 25-30<sup>0</sup> and 35-40<sup>0</sup> is corresponding to the first stages of hexagonal phase formation. Between the peaks of 5% O<sub>2</sub> devices, the (0 0 9) and (0 0 2) hexagonal planes have the highest diffraction intensities. For the 5% O<sub>2</sub> devices, the diffraction lines at 28, 30, 38 and 40<sup>0</sup> are related with the hexagonal phases with (1 0 0), (0 0 2), (1 1 0) and (2 0 0) planes. The small peaks in several part of the pattern (represented by \*) are expected to be noise from TCO layer.

## 2.10 Conclusion of characterizations

The effects of deionized water rinsing prior to annealing in Ar and air were investigated through electrical and optical analysis of CdTe thin film samples. There's a challenge between the effect of water rinsing and in Ar annealing where water effects are protecting the cell properties from the negative effects of Ar. The water rinsing did not reduce the efficiency but also could reduce the series resistance down to  $R_s=71.6 (\Omega)$ . This could be due to passivation of pinholes or defects on the surface. The maximum FF= 66.44 % obtained for water rinsed in Ar annealed sample.

SEM images of the as-deposited and treated samples shows that treatment will increase the grain sizes. However, water rinsing leads to uniform chlorine diffusion into the grain interiors and reduces the localization of Ar atoms in the film structure. XRD results revealed a single phase crystallinity of zincblende for our R.F. sputtered films with improved orientation for water rinsed in Ar annealed sample (c). The band gap of the as-deposited cell was bigger than the treated ones obtained through transmission spectroscopy. The water rinsing before annealing in Ar ambient seems protect the cell from the defects and impurities penetration (i.e. Ar inert atoms). Also, water molecules can fill the pinholes on the semiconductor surface and reduce the diffusion of Cu into grain boundaries which minimizes the shunts formation and decreases the degradation

rate. However, the effect of water rinsing (as a cheapest solution for pre-treatment process) might be still considered systematically for its reproducible effects on the surface nonuniformity level out and defect passivation issues. In another case, CdTe thin films with  $2.1\mu\text{m}$  thickness were grown by the R.F. magnetron sputtering on top of the commercially available TCO deposited glass substrates under two different mixtures of Ar and  $\text{O}_2$ . The concentration of  $\text{O}_2$  was kept at 0%, 1% and 5%. The crystallographic, morphological, optical and electrical properties of the as-deposited and  $\text{CdCl}_2$  treated samples with subsequent annealing at high temperature were studied by X-ray diffraction, scanning electron microscopy, atomic force microscopy, (optical) UV-vis spectrometry and current-voltage characterization, respectively. X-ray diffraction shows a transition of cubic to hexagonal crystalline phase as the oxygen content increases from 0 to 5%. The measurements obtained larger band gaps and grain sizes for the films with higher oxygen content.

In the next chapter, we consider the defect concentration on the degradation and instability of the CdTe devices. All the considered cases above are considered that how we can improve the performance of the device and how the degradation resources can be prevented. For example water rinse effect and in Ar annealing as well as Oxygenation could lead to lower degradation rate due to the fact that the extra Cu diffusion was prevented. In the next chapter we will numerically consider that in any case that the impurities are inserted into the morphology of the film from the deposition process or characterization shunting, how they can runaway through time and reduce the electrical parameters of the device.

## Chapter III

### Simulation of the Degradation in CdTe Thin Film PV Devices: a numerical approach

The long-term stability of thin film photovoltaic devices remains rather unpredictable compared to their crystalline counterparts. That uncertainty needs to be minimized in order to provide a greater portion of low-cost solar electricity on a global scale. A numerical approach has been developed for predicting the degradation over time of the performance in thin film CdTe devices. The approach couples device simulation with a physical model of uniform degradation that depends on material properties and stress conditions. In the case of CdTe PV devices, a model of mid-gap defect generation proportional to excess charge concentration predicts some of the degradation behaviour observed in real cells, but it appears that more than one mechanism is at play. Specifically, the combined mechanisms of defect formation with simultaneous strengthening of the back contact barrier is worth pursuing further as a cause of degradation under open circuit and forward bias. Additional experimental data and further development of quantitative models are required to better understand the degradation of CdTe PV devices. The approach presented here can have great predictive utility if employed in parallel with experiment.

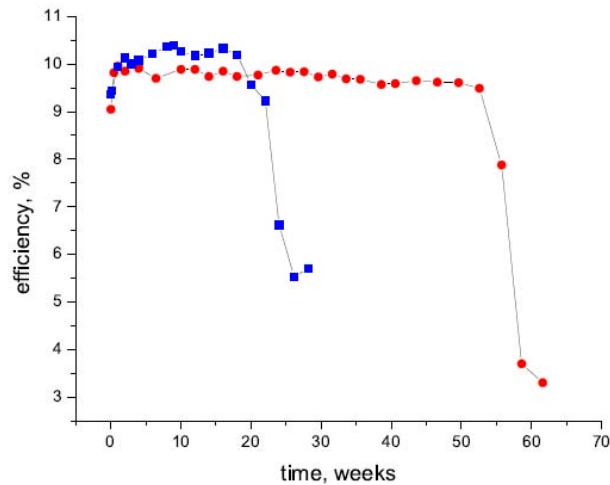


Figure 19: Drastic decrease in efficiency of two CdTe based devices after long time stable performance. Note that the observed drop is still continuous taking several weeks and thus cannot be attributed to a mechanical damage of cells during testing. The time to failure varies between nominally identical cells.

### 3.1 Degradation of the electrical parameters

The long-term stability of thin film photovoltaic devices remains rather unpredictable compared to their crystalline counterparts [52]. That uncertainty needs to be minimized in order to provide a greater portion of low-cost solar electricity on a global scale. Similar reliability issues will be faced by more advanced technologies that have yet to hit the market. Predicting degradation is complicated by the fact that it depends not only on the type of stress (light, temperature, bias, atmospheric conditions, and combinations thereof) but also on fabrication details and transient effects. Inherent nonuniformities (more pronounced in thin films) lead to variable degradation even in devices that have been fabricated and stressed in identical conditions. Moreover, the importance of grain boundary effects (related to regions of enhanced carrier collection, diffusion pathways, strong variations in defect concentrations, etc.) must be considered. A better understanding of the physics is required to improve accelerated life testing and reduce the uncertainty in product lifetimes. Over the past several decades, experimental studies have uncovered important correlations between device recipes, stress conditions, metastable effects, and performance degradation in thin films including CIGS [53, 54, 55] and CdTe solar cells (Fig. 19). The degree of understanding varies with each technology but, in all cases, more quantitative analyses are required to continue moving from correlation to causation based descriptions [56].

In our numerical simulation the device is considered under stress of various conditions: bias, illumination, and temperature. Hence, one can observe the connections between physical/chemical device parameters, stress conditions, and stability based on a postulated time-dependent, physical model of degradation. As a

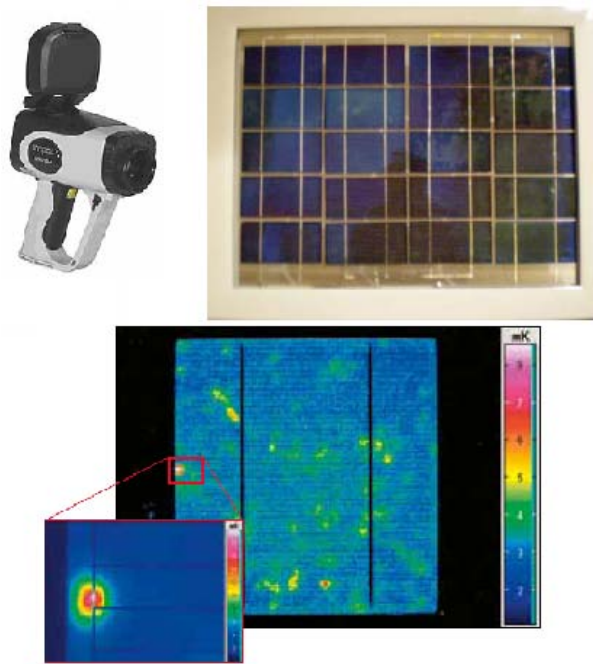


Figure 20: An established way of observing lateral nonuniformities in PV modules is infrared (IR) camera mapping.

case study, CdTe-based PV devices is used here along with a specific physical model of defect generation rates [57, 13]. The device and model studied here can be substituted with others; the rest of the algorithm would remain unaltered.

In what follows, we will refer to uniform degradation mechanisms as those that can be described purely in one dimension. They determine the evolution of performance in terms of temporal changes in device parameters, such as dopant/defect concentrations, carrier concentrations, contact barriers, built-in field, etc., as functions of position along the transversal direction of the device while ignoring the lateral directions.

Though cells are never 1D, no matter how small the area, we may glean some important physics from this approach. Superimposed and coupled with that 1D perspective are nonuniform degradation mechanisms. Their effects are 3D by nature and are related to shunting and weak micro-diodes (regions of low  $V_{oc}$ , but not shunted) [14]. Such nonuniformities are unavoidable in thin film technology due to their unique physics and can have a significant impact on device degradation by robbing current from a large area of the cell or creating hot spot (runaway) instabilities [58, 59]. The coupling between uniform and nonuniform mechanisms is unclear. An established way of observing lateral nonuniformities in PV modules is infrared (IR) camera mapping: IR pictures of different parts of a module showing different temperatures; these nonuniformities depend on the device current and voltage. There exists a variety of complimentary mapping techniques, which also reveal lateral nonuniformities: optical beam induced current (OBIC), electron beam

induced current (EBIC), surface photovoltage (SPV) mapping, photoluminescence (PL) mapping, and some others (Fig. 20) [27, 30]

1D numerical modelling was used to predict photoinduced degradation in a-Si:H based on the model of defect generation proportional to recombination rate [60]. The model fit the experimental results well if only midgap defects were allowed to vary with time. A similar model will be used here for the case of CdTe cells. Numerical methods have also been employed to study the metastable behaviour of intrinsic defects in CIGS [61]. There it is suggested that multivalent defects that undergo thermally activated transitions between donor and acceptor configurations are responsible for metastabilities and stress-induced performance variations.

Ultimately, device stability is measured in terms of the efficiency variation over time,  $\eta(t)$ . Degradation modes are the observed temporal changes in performance, including the metrics of open circuit voltage, short circuit current, and fill factor, as well as J-V curve features, such as rollover and dark/light crossover. Quantitative physical models should elucidate the link between the observed modes and the underlying degradation mechanisms.

### 3.2 Numerical algorithm

The first step in the procedure is to specify the baseline cell parameters for use in a solar cell device simulator. Here we used the freeware 1D solar cell simulator SCAPS-1D, but others could be used. SCAPS was selected for its ease of use, low computational cost, internal batch-run and scripting options, and unique ability to simulate capacitance-voltage (CV) and capacitance-frequency (Cf) [62]. Although only seven device layers are allowed, interface states can be input between each layer and the parameters can be input as functions of distance (graded). SCAPS uses finite difference techniques to numerically solve the coupled Poisson and current continuity equations for the electric potential and quasi-Fermi levels for electrons [ $E_{Fn}(x)$ ] and holes [ $E_{Fp}(x)$ ] in one dimension.

Another requirement is a time-dependent model of degradation that determines the evolution of a specific device parameter in terms of stress-related conditions. For example, a model considered here tracks the formation of mid-gap defects as a function of excess charge carriers, the profile of which depends on light, bias, and temperature. In that example, we would refer to mid-gap defects as affected parameters and excess charge carriers as causal parameters. Other conceivable models can be used, such as effects caused by mobile ion diffusion/electromigration, accumulation of interfacial defects, etc.

Ultimately, the time-dependent mathematical model will be cast into a discrete-time form. After establishing the baseline parameters and physical model, the algorithm entails the following steps:

- (1) divide the semiconductor layers into a number of sublayers or, if possible, input the parameters as continuous functions of distance;
- (2) numerically solve the semiconductor equations under reference conditions (in the dark, unbiased at

room temperature) to establish the initial performance metrics ( $\eta$ , FF,  $V_{oc}$ , and  $J_{sc}$ ) and band diagram;

(3) solve the semiconductor equations under the desired stress conditions to determine the new values of the causal parameters;

(4) use the discrete-time form of the model to predict the new values of the affected parameters based on the causal ones;

(5) calculate the performance metrics under reference conditions now with the new affected parameters as input values;

(6) repeat (3)-(5) with the new causal values until the desired number of time steps has been reached.

The algorithm is used to investigate the effects of a model by systematically varying stress conditions: illumination, temperature, and bias.

An important limitation is that the discrete-time approach averages the effects over time but the predominant degradation modes should be observable. As with all simulators, given the large number of input parameters, it is important to employ a judicious alteration of input values. Another issue is that more than one degradation mechanism may be at play in real devices and distinguishing their effects may be difficult.

### 3.3 Theory and model

This section focuses on CdTe-based thin gfilm solar cells. We start with the established Gloeckler baseline model [103] which has a superstrate structure with the layers  $\text{SnO}_2/\text{CdS}/\text{CdTe}$  of thicknesses of 500 nm, 25 nm, and 4000 nm, respectively. For the purpose of tracking defect evolution in the absorber, the CdTe layer was divided into 4, 1- $\mu\text{m}$  layers, labelled as  $i = 1-4$  in Fig. . The PV devices performance metrics of this cell as calculated using SCAPS are:  $\eta=15.97\%$ ,  $V_{oc}=0.87\text{ V}$ ,  $J_{sc}=24.1\text{ mA/cm}^2$ , and  $\text{FF}=76.2\%$ ; these values serve as the initial/normalization values for the results presented below.

The reference (equilibrium) condition for this study was dark, with zero bias, at  $T=300\text{ K}$ . Stressing was simulated either in the dark or AM 1.5G light at an intensity of  $100\text{ mW/cm}^2$ . Reverse, zero, open-circuit, and forward bias values were applied to the device at temperatures of 300 and 333 K. Various combinations of the stressing conditions are evaluated later on. We will consider three similar models, all of which depend on charge carrier concentrations. They are based on a quantitative model that was evaluated in connection with electron beam induced current (EBIC) decay in CdTe PV devices [13]. The basic premise of it is that excess charge carriers (electrons and/or holes) cause new defects to form. Those carriers could be introduced through doping or external excitations. Material properties are altered by the new defects thereby increasing recombination or altering the built-in field. In turn, those changes affect free charge carrier formation and a feedback loop is established. Hence, there is a coupling between defect formation and charge carrier concentrations. At this point, the microscopic nature of the defects, including the associated lattice reconfigurations and specific energy levels, will not be considered; this study focuses on

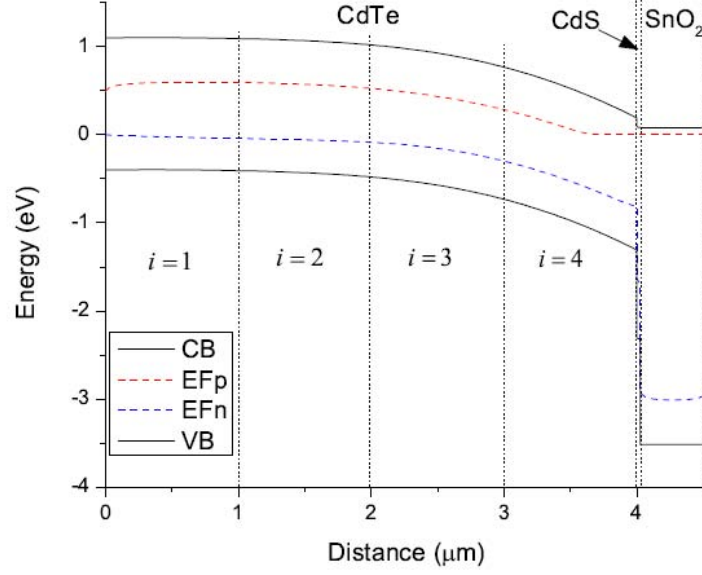


Figure 21: Device structure and equilibrium band diagram for the baseline cell showing the division of the CdTe into  $i=1-4$  layers. The band diagram is for AM1.5G, 1 sun light at short-circuit conditions.

the predictions of the degradation model based on the evolution of generic mid-gap defects. Specific defect parameters could be included, but at this point we want to minimize the number of tunable parameters.

In its simplest form, the defect generation rate is linearly proportional to the concentration of nonequilibrium charge carriers. Hence, the rate equation is given by [13],

$$\frac{dN}{dt} = \alpha n - \beta N \quad (4)$$

where  $\alpha$  and  $\beta$  are, respectively, defect creation and annihilation rates, and  $n$  can represent either electrons or holes. The term with  $\beta$  accounts for annealing effects that lead to saturation or reversal of defect formation. Both  $\alpha$  and  $\beta$  are material parameters that are temperature activated and depend on the type of defect being considered.

The coupling of Eq. (4) with  $n$  can be established through the quasi-stationary approximation,  $\frac{dn}{dt} = G - C_n N_n \approx 0$ , where  $G$  is the generation rate, and  $C_n$  is the recombination coefficient. Solving the coupled equations results in an exponential time dependence for  $N(t)$  that saturates at  $N_\infty = \sqrt{\alpha G / C_n \beta}$ . To further simplify our discussion, here we will consider only the short time approximation, when annealing is insignificant ( $\beta t \ll 1$ ). In that case the linear model yields the following defect generation rate,

$$N = N_0 \sqrt{1 + \frac{t}{\tau}} \quad (5)$$

where  $N_0$  is the initial defect concentration and the characteristic degradation time is  $\tau = N_0^2 C_n / (2\alpha G)$ . maybe if holes are used in the model, the quasi stationary approximation is  $G - C_p p^2 = 0$ , which leads to  $N \propto t$ .

We will also consider two forms of higher order kinetics: (i) quadratic in electron concentration, and (ii) proportional to the recombination rate, or electron-hole product  $np$ . In the approximation of low annealing, the rate equation for the quadratic model is [13],

$$dN/dt = \alpha n^2 \quad (6)$$

Defect generation proportional to  $n^2$  (electrons or holes) can be associated with the formation of certain types of defects, such as negative-U, AX, or DX centers, which have been studied using first principles methods in CIGS [64] and CdTe [63, 65]. The recombination-based model is predominantly mentioned in the literature for a:Si-H, where defect generation is modelled by direct recombination of free electrons and holes. The generation rate (again, neglecting annealing) is then given by [66],

$$dN/dt = \alpha Cnp = \alpha R \quad (7)$$

where  $C$  is the overall transition probability for  $np$  annihilation at the defect centre and  $R$  is the recombination rate. We note that the meaning and units of  $\alpha$  is different in the different models. The quasi-static balance conditions give the carrier concentrations as  $n=G/C_n N$  and  $p=G/C_p N$ , yielding the defect generation rate,

$$N = N_0 \sqrt[3]{1 + \frac{t}{\tau}} \quad (8)$$

The characteristic time is different in this case and depends more strongly on the generation rate:  $\tau = N_0^2 C_n C_p / (3\alpha G^2)$ . The results of Eq. (8) can be reduced to the more familiar dependence in the a-Si:H literature:  $N(t) \approx c_{sw} G^{2/3} t^{1/3}$ , where  $c_{sw}$  is the Staebler-Wronski coefficient. It fits the degradation data for a-Si:H well over a limited range [66]. More comprehensive defect rate equations and the notion of dispersive behaviour in disordered systems have led to stretched exponential time dependence which fits a wider range of data [67]. The above generation rate equations must be cast into discrete forms for use in the numerical model.

Neglecting the annihilation term, the linear model in Eq. (4) can be written as,

$$N_i^{(t+1)} = N_i^{(t)} + \alpha \Delta t (n_i^{(t)} - n_i^{(0)}) \quad (9)$$

where  $n$  represents the appropriate species concentration depending on the scenario being modelled (holes were used for the simulations in this study), and the superscripts are the time increments separated by the step size  $\Delta t$ . The subscript  $i=1, 2, 3, \dots$  refers to the sublayers that the device is partitioned into for modelling purposes, but may be converted into continuous functions of position if allowed by the simulation software. As mentioned above, the CdTe layer was split into 4 layers of 1- $\mu\text{m}$ -thick in this study (see Fig. ).

The concentrations are therefore taken as the mean value in each layer. Similar notations pertain to the higher order rate equations given in Eqs. (3) and (4) with discrete forms:

$$N_i^{(t+1)} = N_i^{(t)} + \alpha \Delta t (n_i^{(t)} - n_i^{(0)})^2 \quad (10)$$

and

$$N_i^{(t+1)} = N_i^{(t)} + \alpha \Delta t R \quad (11)$$

The analytical treatment assumes that recombination coefficients are independent of defect concentrations and their occupancies. That assumption is not required in the numerical approach because the solver calculates recombination,  $R$ , based on the Shockley-Read-Hall (SRH) model.

Another critical point is that the numerical approach considers the spatial dependence of all parameters, while the analytical estimates assume spatially uniform values. This is an important difference because the location of new defects can be just as important as concentration with respect to the degradation rate and observed mode.

### 3.4 Variation of electrical parameters by time

In this section, the rate equations (9), (10), and (11) will be referred to as the  $p$ -model (since hole concentration is used),  $n^2$ -model (electron concentration), and  $np$ -model, respectively. Again, saturation effects are not included so the results pertain to early stage degradation. Simulation results for the  $p$ -model will be presented first followed by the  $n^2$  and  $np$ -model for comparison. All light stress conditions refer to AM1.5G, 1-sun. Using the  $p$ -model, the general trends and modes of degradation for stress conditions of  $T=300$  K, bias near  $V_{oc}$ , under light and in the dark are presented in Fig. 22 (a) and (b), respectively. The performance metrics were normalized to the baseline values and each time step was set to  $\alpha \Delta t=1$  in Eq. (9). For this analyses, we kept the device under light and open-circuit conditions during each of 8 time steps at the end of each we calculated the electrical parameters. After 8 time steps under light, the efficiency decreased by 23 % with about 17 % loss for FF and nearly equal losses in  $V_{oc}$  and  $J_{sc}$  of about 3-4 %. In the other case, the device was left under darkness and in open-circuit condition. The dark results after 10 time steps show a very similar trend but with 19 % loss in efficiency (16.5 % after 8 steps) and less relative decrease in  $J_{sc}$ . The tenth time step in the dark shows nearly the same values as the sixth time step in light, indicating that the degradation modes are the same, only the rate is accelerated in the light. In other words, allowing the dark conditions to continue for a longer time would likely render the two scenarios equivalent. Correlation coefficients for the light case are presented in Table 2 and show a strong connection between efficiency loss,  $V_{oc}$ , and FF.

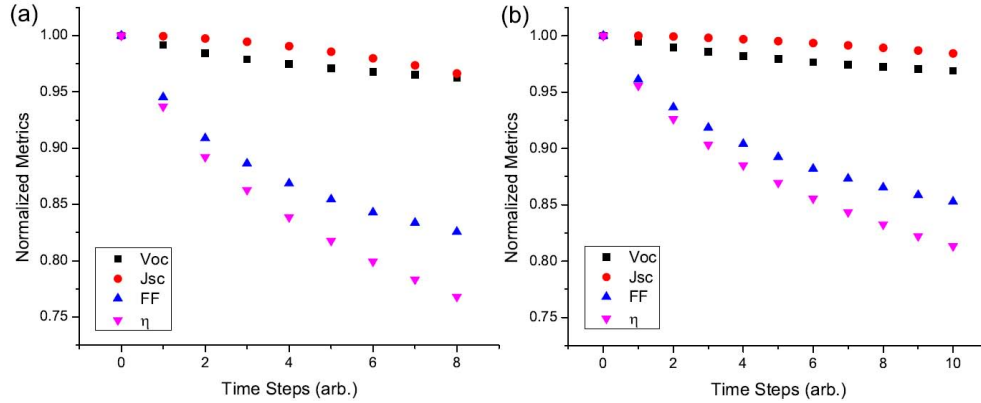


Figure 22: Degradation of performance metrics as functions of dimensionless time ( $\alpha \Delta t=1$ ) simulated for stress conditions: (a) AM1.5 illumination,  $100 \text{ mW/cm}^2$  intensity, bias= $V_{oc}$ ,  $T=300 \text{ K}$ ; (b) dark, bias= $0.85 \text{ V}$ ,  $T=300 \text{ K}$ . Results are normalized to the baseline values  $\eta_0 = 15.97 \%$ ,  $V_{oc}=0.87 \text{ V}$ ,  $J_{sc}=24.1 \text{ mA/cm}^2$ ,  $FF=76.2 \%$ .

Table 2: Correlation coefficients for the degradation of PV devices metrics under light, bias= $V_{oc}$ ,  $T=300 \text{ K}$ .

Source	$\Delta\eta$	$\Delta V_{oc}$	$\Delta J_{sc}$	$\Delta FF$
p-model	10	1.4	0.2	8.4
np-model	10	1.5	2	8.4
$n^2$ -model	10	3.4	1.0	5.8
Ref. 17	10	1-3	1-3+	8-10
Ref. 18	12	4	2+	9
Ref. 19	39	11	6	26

The results are summarized in Fig. 23 for  $T=300 \text{ K}$  after 8 time steps of  $\alpha\Delta t=1$  in each case. Very little degradation was observed for the short-circuit and reverse-bias conditions, which is to be expected since excess charge carriers are quickly swept away by the strong electric field. The stronger dependence on bias than light is also natural since carrier concentrations depend exponentially on applied voltage and linearly on photon flux.

Light and dark stress conditions were also evaluated at short-circuit and reverse-bias= $-0.5 \text{ V}$  conditions. The case of stress under light at bias= $V_{oc}$  was also compared at two different temperature of  $T=300$  and  $T=333 \text{ K}$  as shown in Fig. 24. At both temperatures, the same trend is observed for efficiency decay. It is important to note that the simulation for both temperatures was run at time steps of  $\alpha\Delta t=1$ , yet  $\alpha$  is very different because it is temperature activated,  $\alpha \propto \exp(E_a/kT)$ . Assuming an activation energy  $E_a \approx 1 \text{ eV}$  would result in  $\alpha$  being about 50 times greater at 333 than at 300 K. Therefore, in real time, the degradation rate would be about 50 times faster at 333 K. Although SCAPS does not calculate temperature-dependent mobilities, it does so for the effective densities of state and all exponential temperature dependencies. A comparison of the degradation behaviour for the  $n_2$ -model and np-model is shown in Fig. 25, with stress conditions of light, bias= $V_{oc}$ , and  $T=300 \text{ K}$ . Since numerical values for  $\alpha$  are unknown, time steps were chosen such that significant degradation could be observed in 5-10 steps. Though arbitrary, that method allows us to investigate the differences in modes for the various mechanisms. For the  $n^2$  model,  $\alpha\Delta t=t=10^{-12}$

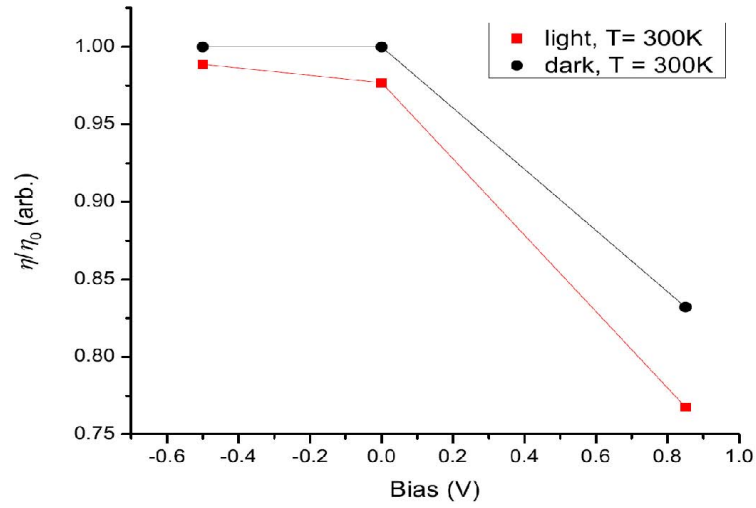


Figure 23: Efficiency variation after 8 time steps as a function of bias for light and dark conditions at  $T=300$  K. Efficiency normalized to initial value  $\eta=15.97$  %.

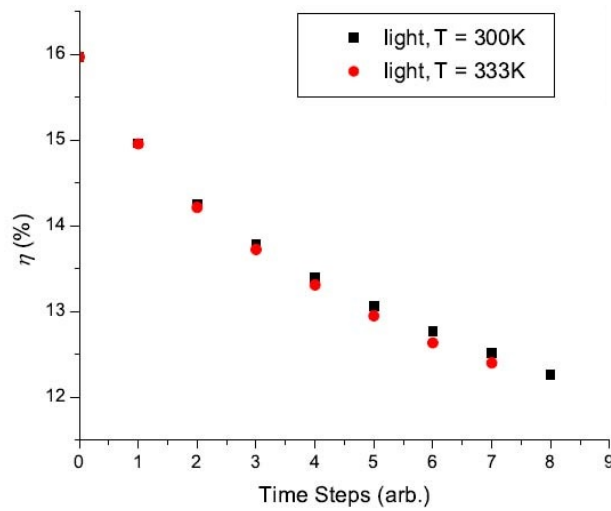


Figure 24: Efficiency degradation under light and bias= $V_{oc}$  at two different temperatures. Although the lines overlap, the degradation is much greater at the higher temperatures in realtime devices.

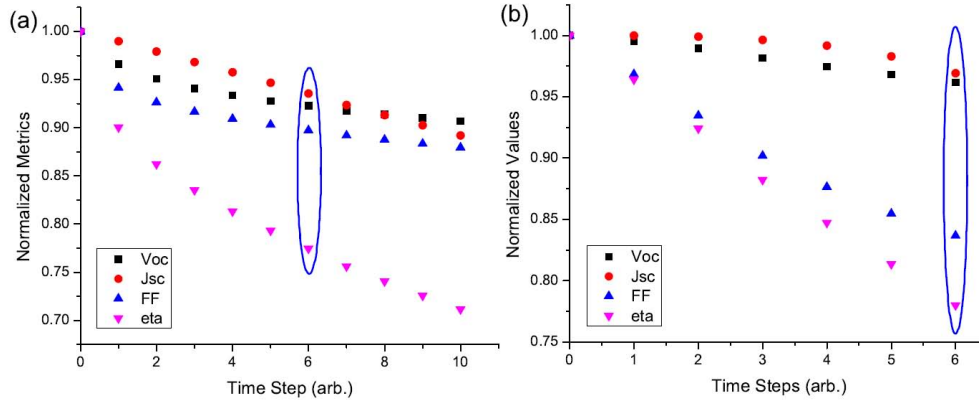


Figure 25: Degradation of performance metrics for (a) the  $n^2$ -model of Eq. (6) and (b) the  $np$ -model of Eq. (7). Stress conditions are light, bias= $V_{oc}$ ,  $T=300$  K. Metrics are normalized to the baseline values. The time steps are (a)  $\alpha\Delta t=10^{-12}$  and (b)  $\alpha\Delta t=3\times 10^{-7}$ . The circled values indicate nearly equal efficiency loss  $\eta/\eta_0\approx 77.5\%$ .

was used and  $\alpha\Delta t=3\times 10^{-7}$  for the  $np$ -model. After six time steps, efficiency drops by about 22.5 % from the baseline value in both cases. However, degradation in the  $np$ -model is more driven by FF ( $\approx 16$  % of the loss), while  $V_{oc}$  and  $J_{sc}$  contribute almost equal parts of the remainder. FF contribute about 8 % of the loss in the  $n^2$ -model. The general shapes of the curves are also different. In the  $np$ -model,  $\eta$ , FF, and  $V_{oc}$  are nearly linear. In both cases,  $J_{sc}$  takes on a different curvature than the other three metrics, which tend to be very similar to each other.

It is interesting to observe the differences in how the spatial distributions of mid-gap defects for each model evolve during stress. Fig. 26 illustrates mean mid-gap defect concentrations in the 4 layers of CdTe for each of the three models. For the  $p$ -model, more defects are generated in the middle two layers, where the increase in hole concentration is the greatest. Eq. (6) provides a reasonable fit to defect generation rates in layers 1 and 4, where the exponent is close to  $1/2$ , but it breaks down in layers 2 and 3. The assumptions of uniform recombination rate and recombination coefficient independent of defect concentration may not be appropriate there. Taking the overall average defect concentration as a function of time leads to a good fit with Eq. (6) using an exponent of 0.65 rather than 0.5 (not shown).

The  $n^2$ -model [Fig. 26(b) - note the ordinate log scale] leads to a very different defect distribution with accumulation near the CdS/CdTe interface (layer 4). In that region, defect generation is better fit with an exponential type function,  $N(t)=N_0+a[1-\exp(-t/\tau)]$ , with  $N_0=2\times 10^{14}$  and  $\eta=18.8$ . Fig. 26(c) presents the defect concentrations for the  $np$ -model. As with the  $p$ -model, the defects are predominant in the middle two layers of CdTe. Using Eq. (7) with an exponent of 0.3 rather than  $1/3$  provides a good fit for the defect generation in layer 4 but breaks down for the other layers where, instead of decaying, defect generation accelerates in the regions of higher concentration. In all cases of Fig. 26, the accuracy of the analytical

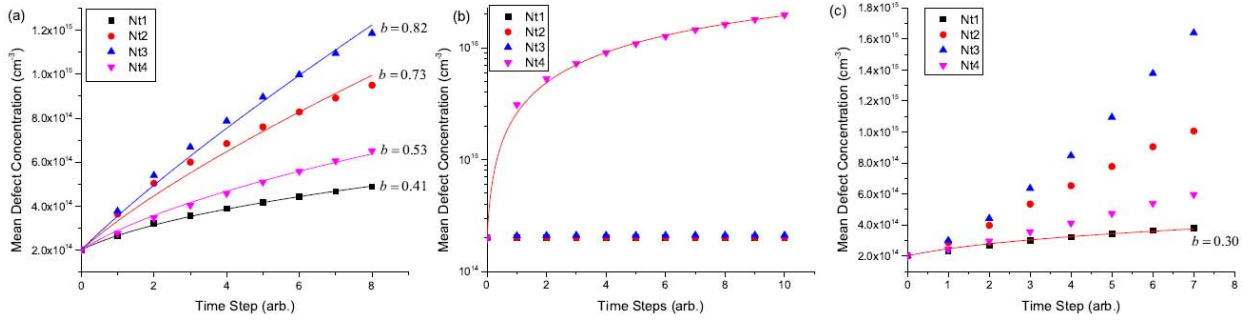


Figure 26: Evolution of mean mid-gap defect concentration in each layer of the CdTe (layer 4 is adjacent to CdS) for the (a) p-model, (b)  $n^2$ -model, and (c) np-model. In (a) and (c) the lines show fits to the data using a general power law,  $N=N_0(1+t/\tau)^b$  with  $N_0=2\times 10^{14} \text{ cm}^{-3}$  and the indicated values of  $b$ , for comparison with Eqs. (2) and (4). An exponential function is used in (b) (see text). A log scale was used for (b) to expose the rapid change in the first two time steps. All stress conditions are light, bias= $V_{oc}$ ,  $T=300 \text{ K}$ .

estimates tend to decrease as the charge carrier concentrations increase.

With a greater concentration of mid-gap defects near the main junction, the  $n^2$ -model leads to greater loss of  $V_{oc}$  compared to the others. Degradation effects on the band diagram are shown in Fig. 27(a): the built-in field decreases as the mid-gap defect concentration becomes high enough to compensate the acceptor concentration ( $N_A=2\times 10^{14} \text{ cm}^{-3}$ ). The p-model also reduces the field but it does so more uniformly across the device, as shown in Fig. 27. Energy band changes are similar for the p- and np-models (not shown).

The J-V curves after degradation in light, bias= $V_{oc}$ , and  $T=300 \text{ K}$  for the three different models are compared to the pre-stress curve in Fig. 28. All post-stress curves represent about 23 % efficiency loss. It can be seen that the  $n^2$ -model results in the most  $V_{oc}$  loss and least FF loss; it also appears to have the least shunt resistance. The p- and np-models are nearly indistinguishable.

### 3.5 Degradation feature in J-V curves

In the above case study, the only parameter that was altered from the baseline value was the mid-gap defect distribution in CdTe,  $N(x, t)$ . Considering models up to second order, its evolution could depend on five combinations of charge carrier concentration:  $n$  and  $p$  in first order and  $np$ ,  $p^2$ , and  $n^2$  in second order models. The results for the p-,  $n^2$ -, and np- models were reported here to illustrate the differences in degradation behavior. Preliminary tests of the n-model indicated a slow degradation rate compared to the p-model and the  $p^2$ -model showed little difference from the np-model. It is important to ask which, if any, of the above models best describes the degradation behaviour of real CdTe cells. The contributions of  $V_{oc}$ , FF, and  $J_{sc}$  losses to overall efficiency loss are shown in Table 3 for each of the three models. In each model case, stress conditions are under light, bias= $V_{oc}$ , and  $T=300 \text{ K}$ . For a 10 % efficiency loss in both the p-

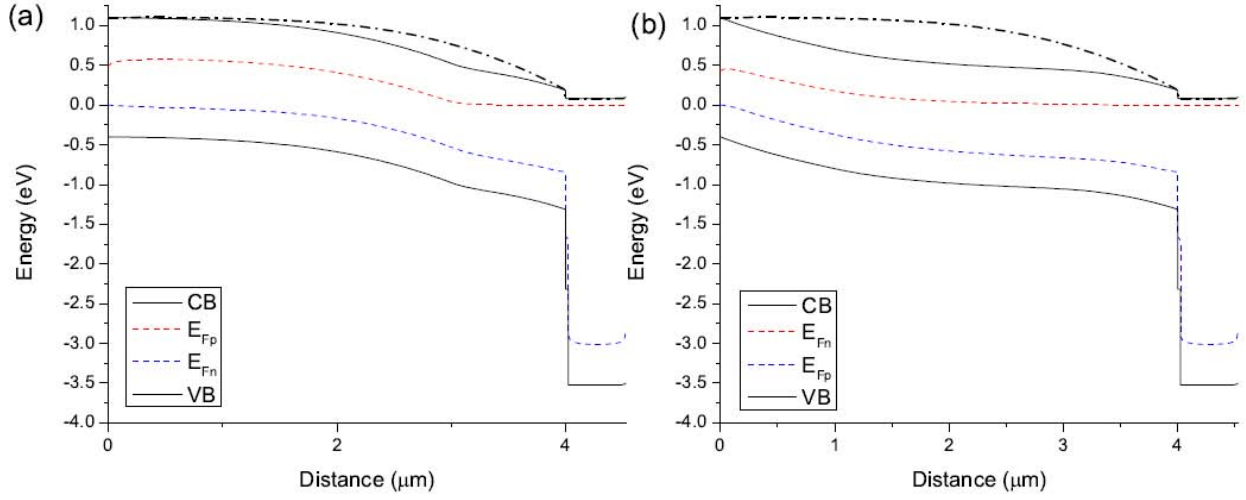


Figure 27: Band diagrams at  $J_{sc}$  for the degraded cells using (a) the  $n^2$ -model and (b) the p-model. The pre-stress conduction band is shown as the dash-dot line for comparison. Stress conditions are light, bias= $V_{oc}$ ,  $T=300$  K. Both diagrams are at an efficiency loss of 25 %.

Table 3: Contributions to efficiency loss (all in %) from the models studied herein and approximate values obtained from Refs. [70, 71] The model stress conditions were: light, bias= $V_{oc}$ ,  $T=300$  K. All bias stress was at bias= $V_{oc}$ .

The + indicates an increase in the value.

	$\eta$	FF	$J_{sc}$	$V_{oc}$
$\eta$	1	-	-	-
FF	0.997	1	-	-
$J_{sc}$	0.884	0.847	1	-
$V_{oc}$	0.901	0.993	0.998	1

and np-models, FF contributes more than 8 % of the total loss, with between 1-2 % from  $V_{oc}$ , and minimal loss. The n-model shows declines of 5-6 % for FF, 3-4 % for  $V_{oc}$ , and about 1 % for  $J_{sc}$ . A comparison to representative data [68] shows that the p and np models are more indicative of the observed degradation mode, while the  $n^2$ -model yields more relative loss in  $V_{oc}$ . The degradation mode that is typically observed in CdTe cells stressed under forward bias= $V_{oc}$  has the greatest loss in FF, followed by some loss in  $V_{oc}$ , and minimal  $J_{sc}$  decline (sometimes it increases).

Care must be taken in discerning the different modes because greater relative losses in  $V_{oc}$  and  $J_{sc}$  have been observed under reverse bias stress [69, 56]. Comparing the band diagrams in Figs. 27 (a) and (b),

provides some insight to the cause of excessive FF loss. In the p-model, the weaker electric field and greater mid-gap defect concentration distributed over a wide region of the CdTe layer leads to greater recombination and less current collection. Excessive recombination in near the main junction in the  $n^2$ -model leads to greater  $V_{oc}$  loss. Another discriminating feature is the time dependence of performance losses. Referring to Figs. 22 and Figs. 25, the np-model leads to a linear decline in efficiency over time, while both the p- and  $n^2$ -models can be reasonably fit with a power law,  $\eta(t) = N_0(1 + \alpha t)^a$ . A power

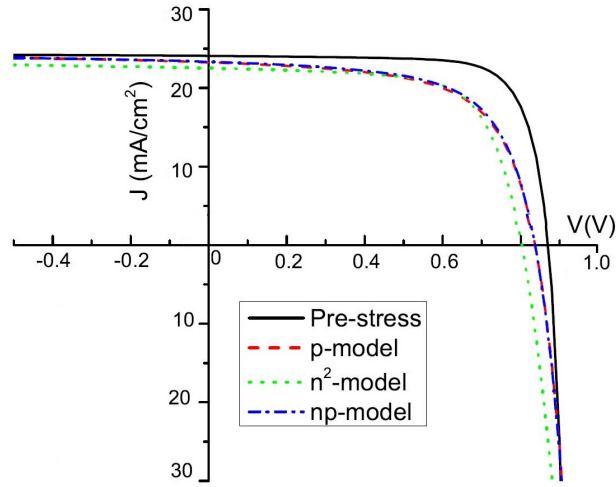


Figure 28: Pre-stress and post-stress J-V curves for the three models discussed in the text. Stress conditions are light, bias= $V_{oc}$ ,  $T=300$  K. Each post-stress condition is at approximately 23 % efficiency loss.

law dependence was also used in Ref. [70] to fit  $\eta(t)$  for 2000 hours of light soak, bias= $V_{oc}$ , and at various temperatures. Degradation features are often observed in the first quadrant of the J-V curve. As shown in Fig. 29, both the p- and  $n^2$  models indicate light-dark crossover, but only the  $n^2$ -model exhibits early signs of rollover. In both cases, the effects are small and occur at relatively high currents compared to what is typically observed in degradation studies [69, 71].

There are several mechanisms that are not included in the models studied here. One important example for CdTe is the change in the back contact barrier.<sup>13</sup> For the sake of discussion, if the back barrier for holes at the CdTe/metal contact is increased from the baseline value of  $\phi_{bp} = 0.4$  eV to 0.5 eV, the J-V curves for the post-stress  $n^2$ -model results [Fig. 29(b)] change to those shown in Fig. 30. It is evident that the rollover feature becomes much more prominent with increasing barrier height.

Those J-V curves are representative of what is typically observed for forward bias degraded CdTe with Cu-containing back contacts. Adding the higher barrier to the already stressed cell lowers the  $V_{oc}$  from 0.80 to 0.78 V and the FF more drastically from 68.35 % to 61.57 %, with an efficiency drop from 12.37 to 10.84 %. Those changes match well with the degradation/recontacting study of Ref. [68] where it was found that  $V_{oc}$  did not recover after recontacting while FF partially recovered (i.e.  $V_{oc}$  loss was not associated with back contact deterioration).

The numerical approach to uniform degradation would be useful for studying other possible mechanisms specific to CdTe including, compensation of shallow donors in the CdS layer, lowering of the CdS band gap, electromigration of mobile ions (typically Cu) [72] and deterioration of the main junction due to diffusion of S from the CdS region. Such studies are essential because many observations remain unexplained:

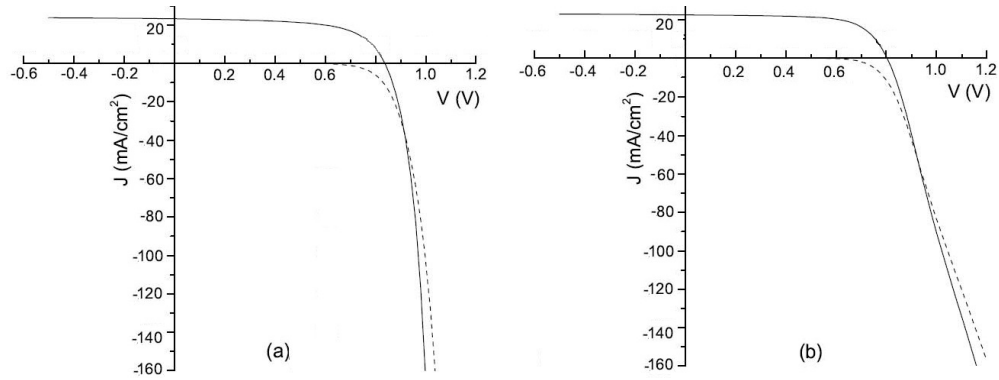


Figure 29: Post-stress light and dark J-V curves for the (a) p-model and (b)  $n^2$ -model. Stress conditions are light, bias= $V_{oc}$ ,  $T=300$  K. Each post-stress condition is approximately at 23 % efficiency loss.

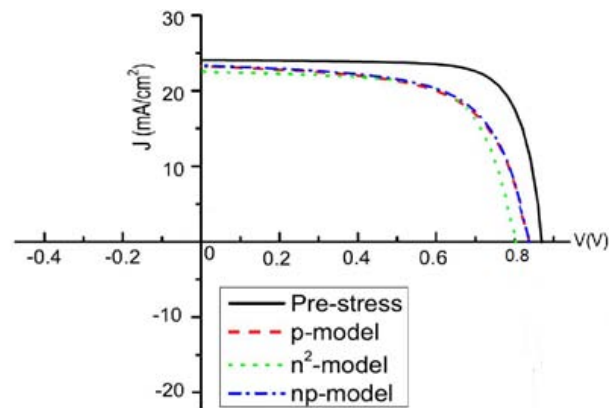


Figure 30: Post-stress light and dark J-V curves for the p-model,  $n^2$ -model and np-model. Stress conditions are light, bias= $V_{oc}$ ,  $T=300$  K. Each post-stress condition is approximately at 23 % efficiency loss.

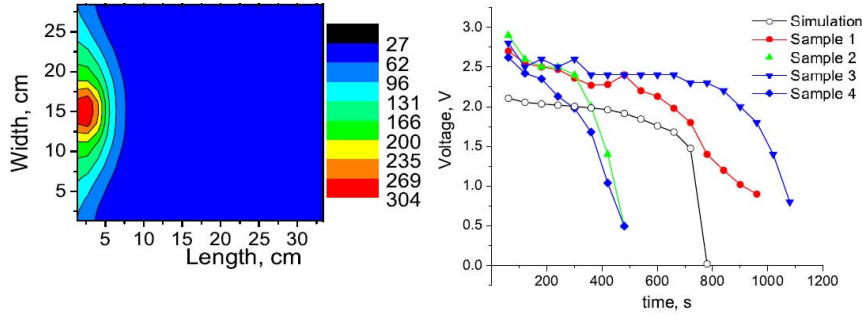


Figure 31: Hot spot runaway over time in a thin film device and the distribution of voltage and temperature around this spot.

degradation under reverse bias (with different modes than forward bias); differences in degradation behaviour between devices with and without Cu, with different back contact and substrate material [71]; and different degradation modes depending on temperature [70]. In addition to specific mechanisms, such studies must also consider the effects of alternative band structure such as a light-modulated front barrier [73] or a gull-wing singularity due to the piezoelectric nature of CdS [74]. In any case, employing the numerical approach requires a physical model in the spirit of that presented in the next section.

Another question pertains to the nature of  $\alpha$ ; it remains a phenomenological parameter. Its meaning is similar in all the models: it represents the probability of forming new defects in response to the presence of excess charge carriers (or recombination in the np-model). As an activated parameter, small variations in the barrier  $E_\alpha$  result in exponential changes in defect formation rates. Hence, nonuniformities play an important role in the different degradation rates observed in sister cells. Furthermore, as a material parameter the barrier depends on impurities, such as Cu in CdTe cells, leading to a possible cause of the different degradation behaviour of devices with and without Cu. In other words, electromigration of Cu in CdTe devices could have a strong effect on  $\alpha$  and therefore on the degradation behavior. Very recently, the other possible degradation mechanisms for CdTe thin film devices were presented by Vasko et al. using numerical and experimental analysis [59]. This degradation is called hot spot runaway. Hot spots are spontaneously emerged in forward biased thin film photovoltaics based on CdTe devices (Fig. 31). These spots evolve over time shrinking in their diameter and increasing temperature up to approximately 300 °C above that of the surrounding area. Their numerical approach explores a system of many identical diodes in parallel connected through the resistive electrode and through thermal connectors, a model which couples electric and thermal processes. Fig. 31 sketches the temperature and electric potential distributions across the hot spot. Simulated temperature distributions at different time instances. Note the differences in temperature scales shown to the right. The modeling results show that hot spots emerge collapsing from a rather large area of nonuniform temperature, then collapse to local entities. Still further consideration both numerically and experimentally is required to develop the removal or healing of such failures in the thin film solar cells.

---

Even in laterally uniform devices local spot heating is severe and stable enough to sustain the addition of faulty local elements. In order to improve the module design or reduce these degradation modes, a thorough understanding of origin of these defects hot spots and their development resulting into failure is needed first. Various modes of degradation are briefly discussed above which will give an insight to find the reversible solutions.

## Chapter IV

### Electrical Characterization of CIGS Thin Film Devices

Surface Photovoltage Spectroscopy (SPS) is a fast non-destructive method to extract the band gap, surface or bulk defect states energies and to study the doping homogeneity of semiconductor thin film structure. The Cu(In,Ga)S<sub>2</sub> (CIGS) sample shows a steep increase of SPS at the band gap of 1.12 eV for CIGS structure, whereas for CdS window layer it appears at 2.6 eV. However, already below this band gap, we observe a slight SPS response even down to about 1.40 eV photon energies. This indicates the presence of states in the band gap, likely resulting from disorder induced by the Indium doping in order to grade the band gap.

The surface roughness has been obtained from surface topography maps of Atomic Force Microscopy (AFM) on nanometre scale. The improvement in crystallinity of the film occurs by the coalescence of the neighbouring islands driven by the thermal energy acquired from the annealing treatment. The root mean square (rms) roughness of the CIGS thin film was 37.8 nm for 400C annealed film. The grains sizes are almost uniform and smaller than 1  $\mu\text{m}$ .

In continue, the two and four point probe are used in order to characterize a CIGS solar cell. Applying the two wires gives higher current density at the lower voltages due to the lower series resistances while the four wire application results in higher current densities at higher voltages probably due to a better carrier collection. The ideality factor of each voltage region represents the dominant current mechanism. The longer the carrier collection time, the higher the current density at the higher voltage ranges.

Moreover, the two-diode model was used to extract the electrical parameters. A four-diode equivalent circuit for CIGS thin film solar cells incorporating some physical phenomena such as trap states and grain boundaries is also presented. The proposed model can be used for the precise analysis, extraction of the electrical parameters and exact prediction of the current versus voltage characteristic of CIGS thin film solar cells. Furthermore, the buffer layer current and impact ionization effects are introduced and discussed in the equivalent circuit.

#### 4.1 Electrical characterization, spectroscopy and microscopy

The surface photovoltage spectroscopy has been found to be very effective for studying the properties of semiconductor such as extraction of band gap, band gap fluctuation,  $E_g$ , doping levels, defect energy distributions through surface states and homogeneity of the film [75, 76, 77]. The character of the surface electronics is a critical aspect of the CIGS materials that needs to be determined. This technique has been used as contactless technique for the characterization of  $\text{Cu}(\text{In,Ga})\text{Se}_2$  (CIGS) thin film photovoltaic samples [78, 79].

SPS has been also used for quality control of  $\text{ZnO}/\text{CdS}/\text{CIGS}$  thin film solar cells to detect "hard failures" following CIGS deposition, and both "hard" and "soft" failures following CdS and ZnO depositions [80]. SPS measurements on polycrystalline material make it possible to consider the effect of grain boundaries [81]. Further studies on the surface topography of solar cells in nanometre scale can be achieved by atomic force microscopy [82]. On the surface of a CIGS film, the different orientation of crystal facets form the areas with different work function due to the orientation dependent surface dipole [83, 78]. The AFM method provides a better resolution than the other microscopy methods (e.g. Surface Emission Microscopy) and allows real three dimensional manipulation and calculations in the images. Also, the roughness and grain size values of the film structure can be obtained from the AFM images [84].

#### 4.2 CIGS sample preparation

The thin film structure  $\text{ZnO}/\text{CdS}/\text{In}_2\text{S}_3/\text{Cu}(\text{In}_{0.85},\text{Ga}_{0.25})\text{Se}_2/\text{Mo}/\text{Glass}$  (Fig. 32) has been grown on 3 mm soda-lime glass substrates coated with a 300 nm thick Mo film. CIGS layers have been co-evaporated by three-stage process. The In and Ga of group III have been measured by energy dispersive X-ray spectroscopy to  $\text{In}/(\text{In}+\text{Ga})= 0.3$ .

The  $\text{In}_2\text{S}_3$  layers have been grown on these CIGS layers by co-evaporation of elemental Indium and Sulphide. The CIGS substrate temperature during Indium Sulphide deposition was 160 °C measured by a thermocouple positioned at the deposition side of the substrate. The thickness of the layers deposited on glass substrates has been evaluated to be around 50 nm by means of mechanical profilometer measurements. The back contact is conductive  $\text{ZnO}:\text{Al}$  (200 nm).

This sample was provided by the Institut des Matriaux Jean Rouxel, Universit de Nantes, France [85]. CIGS has a chalcopyrite structure (1.8 m) and the cell was treated by rinsing into deionized water (water treatment) and annealed in air at 200 °C for 20 min. The absorber is graded by the three-stage co-evaporation process (between 1.2 and 1.3 eV). The process is bithermal for the CIGS, 400-620 °C measured by thermocouple at the back of the cell. The area of the cell is 0.5 cm<sup>2</sup>. SPS analysis have been carried out at the thin film laboratory of the Department of Physics, University of Bologna. At room temperature, the



Figure 32: The structure of our CIGS thin film solar cell.

photon beam generated by a white light source enters the monochromator SPEX-500M, the monochromatic photon beam coming out of the exit slit is chopped and focused onto the sample surface (Fig. 33, Left). Appropriate low band pass filters have been used to prevent high order diffraction peaks. SPS is determined by measurements of the contribution of the local photocurrent to the tunnelling current while sweeping the voltage applied to the conductive tip [86].

The system allows the measurement of the surface photovoltage SPS signal in a wide spectral range ranging from 300 to 2000 nm by the use of different gratings and light sources (quartz-tungsten-halogen and xenon lamps). Photogenerated electron-hole pairs are collected by the semiconductor surface barrier, and the resulting change in the surface potential is the SPS signal. The SPS signal is capacitively picked up by an electrode made of metallic indium tin oxide film deposited on a thin glass substrate; it goes through a high impedance field effect transistor preamplifier and is measured by a lock-in amplifier [87].

The SPS effect on the band diagram of a CIGS solar cell structure has been displayed in Fig. 33, Right. In the SPS experiment, with the beam on, at the interface of the CIGS/buffer layer, the equilibrium is driven away and the photons of the beam creates the electron hole pairs. The built-in potential separates this pairs near the band edge which leads to a negative photo voltage in the CIGS absorber surface. This is a surface photo voltage with a magnitude as big as the energy of the Fermi level pinning. However, the other properties from both surface and subsurface of the film contribute to the SPS, e. g., the width of the surface space charge region and the recombination rate [78, 86].

The atomic force microscopy analyses were performed in semi-contact mode at the same laboratory. Surface morphology and surface properties have been characterized by AFM (NT MDT-Solver-PRO47). Non-Contact mode has been used to obtain a topography map of the surface. The tip was Silicon-coated Pt/Ir, diamond and conductive nano-needles ( $\text{Ag}_2\text{Ga}$  Nanoneedles). The topographic and current images are obtained simultaneously, as AFM tip scans the surface and the current is measured [88]. In the AFM measurements, between AFM tip and the sample surface, which give a two dimensional AFM topographic image of the surface, there is a Coulomb force between the tip and the sample, based on the difference in work functions between the tip and the sample and a charge transfer between them [89].

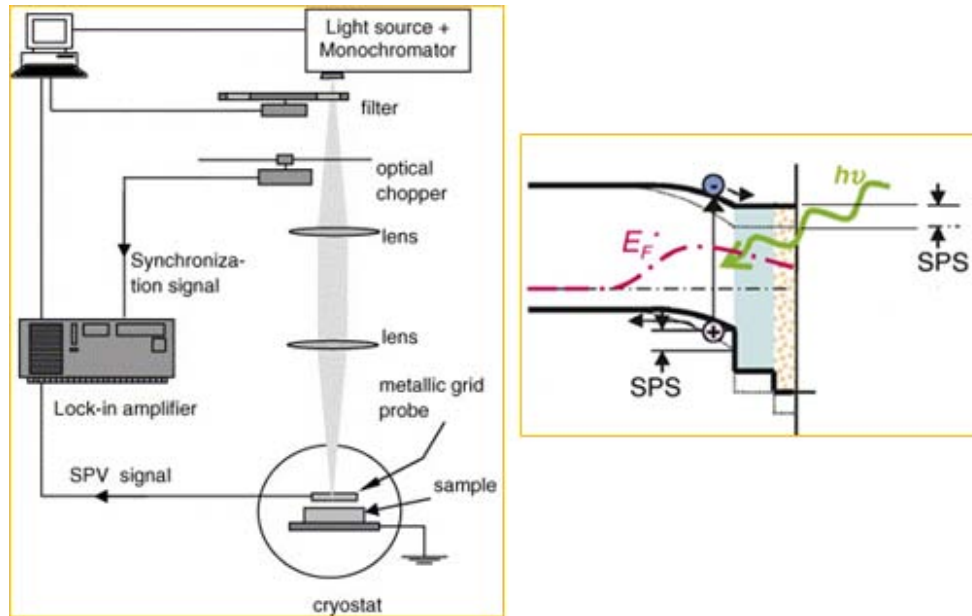


Figure 33: Left: schematic of SPS experimental set-up, Right: SPS effect on the band diagram of CIGS solar cell.

### 4.3. Surface photovoltage spectroscopy analysis

Surface Photovoltage spectroscopy analysis are based on measuring the SPS signal (which is a light-induced variation of the surface potential) as a function of impinging photon beam energy. Here, we discuss the first application of SPS measurements which is the approximate determination of the semiconductor band gap. The SPV signal is plotted versus the energy range of impinging photons in Fig. 34. This spectrum has been taken by grating B with  $1500 \text{ lines}/\mu\text{m}$  for photon energies in the range 0.8-1.4 eV. The most important features to interpret a SPS spectrum are the sharp slope changes knees associated with an abrupt increase of an additional carrier excitation mechanism. Considering the SPV curve in Fig. 34, three peaks and two knees are seen in the right-hand side. At low photon excitation energies SPS signal is 0 since the energy of the light is not sufficient to excite charge carriers in CIGS material. At around 1.16 eV, a peak is observed with  $6.5 \mu\text{V}$  in the spectrum. Then the signal falls for before 0.5 eV and then increases to a peak at about 1.2 eV with almost the same amplitude.

The next knee is seen at higher energies (1.3 eV) but with a lower level of SPS signal about  $5.9 \mu\text{V}$ . Here it might be concluded that the band gap is graded from about 1.12-1.25 eV. It can also be said that the first knee occurs at sub-band gap photon energies and corresponds to the onset of carrier excitation from surface states (as in Fig. 33, right). The second knee occurs in the vicinity of band gap energy and corresponds to the onset of band-to-band carrier excitation. Thus, Indium doping does likely results in graded band gap in

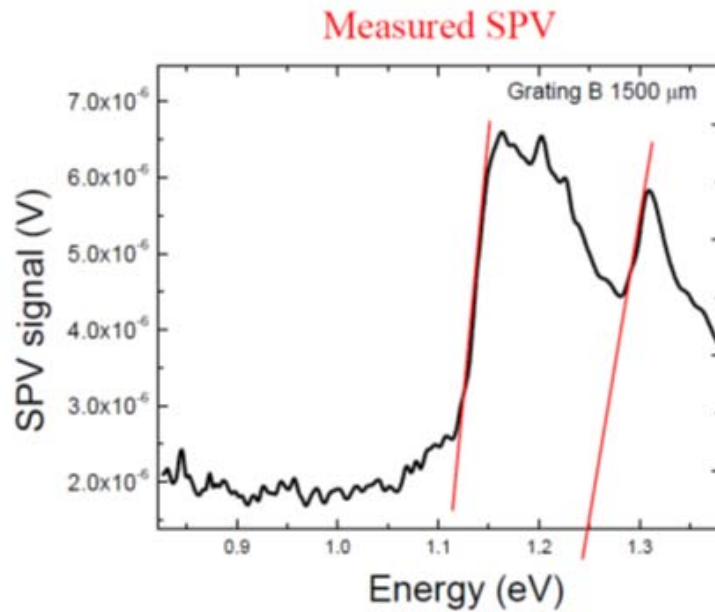


Figure 34: SPV signal vs. photon energy for the treated CdS/In<sub>2</sub>S<sub>3</sub>/CIGS solar cell.

the absorber layer.

The normalized SPS spectrum to its maximum values is seen in Fig. 34 and shows no SPS for photon energies less than 1.11 eV but follows an increase in SPS signal for greater values. The measurements with grating B was done for energy range 0.8-1.4 eV. The first sharp slope is around 1.1-1.2 eV. With a quantitative analysis of such spectra,  $E_g$  has been estimated by extrapolating the linear part of the curve to intercept the photon energy axis. The linear slope extraction results in band gap energy of 1.12 eV as is shown in the left side of the figure. The slope of the other main peak is not well visible to extract the linear slope. On the right side of Fig. 35, the grating A was used with 300 lines/ $\mu\text{m}$  where it remains until the highest energy measured in the spectrum (2.6 eV). Now the SPS increase indicates the band gap energy, at which the photon energies can excite the charge carriers and change the surface band bending. The excitation happens after 2.7 eV and a sharp knee is seen until 3 eV. A linear slope extraction gives a 2.6 eV band gap which is relevant to CdS window layer.

The  $(\text{SPS})^2$  can be assumed to be proportional to the absorption coefficient,  $\alpha$ , of the semiconductor material [78]. CIGS is also a direct band gap material. Then  $\alpha$  which is dependent on  $E_g$  by root square can be calculated to extract  $E_g$  as well. In a semiconductor, the band gap is determined by the absorption coefficient which is also obtained as a function of the photon energy. Note also that the SPS signal is proportional to the optical absorption coefficient. So, the energy gap could be determined by the SPS curve. At photon energies close to the band gap, SPS should increase rapidly up to a saturation value and  $E_g$

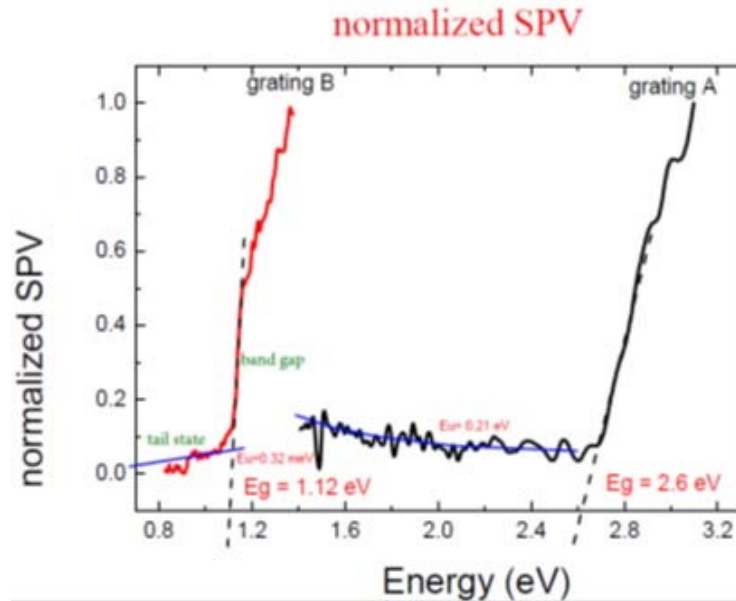


Figure 35: Normalized SPV spectrum vs. impinging photon energy through two different gratings A and B.

should be determined by the energy position of the knee. Sometimes, as in the present case, a peak rather than a knee is observed, due to electron-hole recombination at the surface strongly reducing the SPS signal for  $E \leq E_g$ .

At photon energies closer to the band gap of the cell, the SPS signal increases rapidly up to a saturation value and  $E_g$  should be determined by the energy position of the knee. In this case, a peak is observed due to electron-hole recombination at the surface which strongly reduces the SPS signal for  $E \geq E_g$ . The main peak can be related to the energy gap values  $E_g$  of the compounds. Thus, at photon energies close to  $E_g$ , the electron-hole pairs are generated in the near-surface layer and mainly recombine there through the high available density of surface states. The resulting SPS signal thus decreases. Therefore, only the peaks in the SPS spectra relevant to the surfaces provide the real value of  $E_g$ , which is equal to 1.12 eV for CIGS. At energy values higher than  $E_g$ , the signal starts decreasing due to electron-hole recombination at the surface, then it increases again and reaches a maximum at 1.3 eV. The measured band gap in our experiments is in agreement with the reported values in Ref. [90].

The broad peak related to the CIGS material observed in Fig. 35 and its energy gap of 1.12 eV for CIGS and 2.6 eV for CdS is in good agreement with the values reported in [91]. The measurements have been found quiet reproducible. The other main conclusion from Fig. 35 is that the normalized SPS spectrum taken with both gratings shows a non-zero value at energies lower than band gap. This sub-band gap SPS signals come from sub-band gap absorption representing the presence of trap or defect states in materials band gap. Such states are called Urbach band tails. The fitting results are 0.32 meV and 0.21 eV for

CIGS and CdS materials, respectively. The largest value of Urbach energies represents deeper tail states in band gap. Urbach energy is a measure of disorder in the material or an effect of high doping concentration ( $N_A \geq 10^{18} \text{cm}^{-3}$ ). In  $\text{CuInSe}_2$  and in  $\text{CuInS}_2$  sub-bandgap absorption is small. Urbach energy for CIGS materials suggests that the disorder is due to thermal vibration of lattice atoms.

#### 4.4 Atomic force microscopy analysis

AFM has been used to map the surface morphology and phase inhomogeneities of this thin film heterojunction. Since the sample is band gap graded by changing the Indium concentration through the absorber layer, the surface energy may spatially vary due to differences in the chemical composition. Thus, a phase image can represent the compositional inhomogeneity on the sample surface. Fig. 36,Left, shows the topography image obtained in AFM semi-contact mode surface of CIGS solar cell in the dark at low positive sample bias. The estimated average root mean square (rms) roughness of the CIGS thin film is around 37.8 nm for 400C annealed film. The grains sizes are almost uniform and smaller than 1  $\mu\text{m}$ . The morphology shows the presence of granular grains and treatment solutions (deionized water). These grains are typical of three-stage deposition process. Besides the grains there are also white spots that represent the complexes made after the treatment and annealing. Fig. 36,Right, is the phase image of the same area.

In this topographic image, the grains and Grain Boundaries (GB) are clearly seen. The variation of GBs due to differences in crystallographic orientation, contaminants and film quality is seen. The pixels in the two images have a corresponding relationship. The dark red parts represent the surface height in the range of 100 nm and the lighter ones are lower than 190 nm and 94 degree phase. The phase image is a signature of inhomogeneity in the composition of the sample surface; this image can be attributed to Indium segregation at surface defect states [90]. The surface diffusivity of Indium is higher than that of the other chemical components in thin film structure; therefore, Indium would segregate more likely. The surface of the cell looks slightly rough (rms=37.8 nm) but almost smooth with no cracks. This conclusion was attributed to the presence of  $\text{In}_2\text{S}_3$  buffer layer [90]. Clearly the growth conditions and annealing have a strong influence on the surface topography of CIGS films. The improvement in crystallinity of the film occurs by the nucleation of the neighbouring islands after the annealing treatment. Comparing the rms of our AFM on the treated CIGS film with the as-deposited film of Ref. [85], it can be deduced that the surface obtained after the treatment at 400 °C is smoother than the as-deposited films and the films annealed at 200 °C. A smoother film reduces the light trapping at the surface and reduces the number of interface states between the absorber layer and the window layer in the device. The films showed 112 oriented peaks with slightly random orientation and the grains average size was less than 1  $\mu\text{m}$ . However, Shafarman et al., [90] reported a random orientation, regardless of the Ga content for the band gap grading purposes, and grain sizes bigger than 2  $\mu\text{m}$ . The conclusion is that the three-stage process will reduce the orientation of the

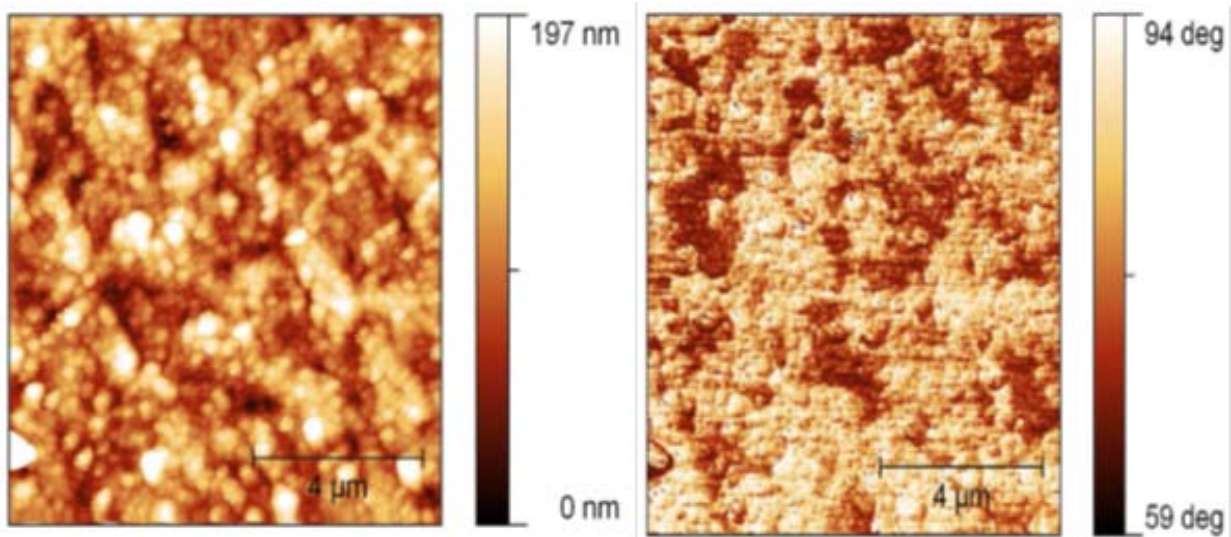


Figure 36: Left: topography of CIGS surface obtained in semi-contact mode showing the roughness and grain size distribution, Right: phase image of the film surface.

nucleation but the grain sizes will be smaller than elemental evaporation from four sources.

In summary, we have investigated a graded band gap chalcopyrite CIGS solar cell by the surface photovoltage spectroscopy and atomic force microscopy. The grading range was deduced by a single SPS signal from 1.12 to 1.25 eV which is acceptable for the Indium concentration against Ga of about 0.3. The CdS showed a 2.4 eV band gap in agreement with the conventional reports on that. The AFM measurements yield information on the orientation of the atomic nucleation and material homogeneity. The grains observed to form very oriented and the average size was almost uniform (less than 1 μm). The topography shows a uniform diffusion of the  $\text{In}_2\text{S}_3$  or deionized water into the absorber layer after the treatment and annealing. The surface of the cell looks slightly rough (rms=37.8 nm) but almost smooth with no cracks.

#### 4.5 Admittance spectroscopy (J-V measurements)

The solar cell for this measurements was fabricated by Helmholtz Zentrum Berlin for Materials and Energy (HZB), Berlin, Germany. A standard Sample of Glass/Mo/Cu(In,Ga)Se<sub>2</sub>/CdS/ZnO/ZnO:Al thin film deposited on a Glass/Mo substrate including a stripe of Al back contact. The front contact from Al is a collector with 2 tiny points which allows us to place the needles on the cell.

Mo has been sputtered with good adhesion on the glass substrate and good conductivity, CIGS and CdS were deposited by three-stage process and chemical bath deposition method, respectively. The process was performed at a nominal temperature of 330°C during stage 1 and at 560°C during stages 2 and 3. Then,

Table 4: The structure and electrical parameters of CIGS thin film solar cell [HZB, Germany].

glass	Mo	CIGS	CdS	ZnO	ZnO:Al	$\eta$	FF	$J_{sc}$	$V_{oc}$
1 $\mu$ m	2.1 $\mu$ m	50nm	325nm	125nm	200nm	16.45 %	73.5 %	35.4 mA/cm <sup>2</sup>	632 mV

ZnO bilayers were sputtered by vapour deposition method. The cells are V type graded band gap with Cu 21.18 (atom %), In (atom %) 20.66, Ga (atom %) 6.78 and Se (atom %) 51.38 leading to Ga/III=0.25, Cu/III=0.77. The integral composition of the absorber layer was measured by wavelength dispersive X-ray Fluorescence method. For the characterization of this device we used the Cascade Summit 12000 Probe Station and Keithley 2620 Sourcemeater connected to the Nucleus software and Labview program to control and record the current and voltage values.

The measurements were done in ARCES, Cesena, Italy. We start to put the sample on the chuck of the Cascade controlling with Nucleus program and make it stable using the vacuum holes over the chuck. However, in this case the sample is not quite stable due to its small size. The microscope and light will help to place 4 needles on the front and back contact of the desired cells. The needles are moved down to contact by handling the relevant gears over the cascade. On the other hand, using Labview code, the voltage can be applied by Source meter to the contacts and the current is measured. We have done 4-wires and 2-wires measurements under dark and biased conditions. For the 4-wires technique, the voltage is applied to the back contact by 2 needles while the front contact is grounded and the current is measured by 2 other needles on the front contact. For the 2-wires technique, the needles with the same role are shorted to common. The electrical parameters of our device were as presented in Table 4.

#### 4.6 Two and four-points probe characterization

The cells are forward biased from 0 V up to 0.7 V under dark condition for two different charge collection times 0.1 s and 10 s. The J-V characteristics were measured at ambient temperature (300 K) by means of two and four wire probe method as was defined above. The results shown in Fig. 38 and Fig. 39.

Since the dark J-V characteristic is a superposition of the two processes, diffusion and recombination, solar cells can then be modelled using the two-diode equivalent circuit shown in Fig. 37 with the diodes D1 and D2 representing the diffusion and recombination processes, respectively. This circuit is described by the following equation,

$$I = I_{01} \left\{ \exp\left(\frac{q(V - IR_s)}{n_1 kT}\right) - 1 \right\} + I_{02} \left\{ \exp\left(\frac{q(V - IR_s)}{n_2 kT}\right) - 1 \right\} + \frac{V - IR_s}{R_{sh}} \quad (12)$$

where V is the applied voltage, n is the diode ideality factor,  $I_0$  is the reverse saturation current, k is the Boltzmann constant, q is the electron charge and  $R_s$  and  $R_{sh}$  are the parasitic series and shunt resistances, respectively. The indices 1 and 2 are used for the first and the second junction interfaces or diodes which

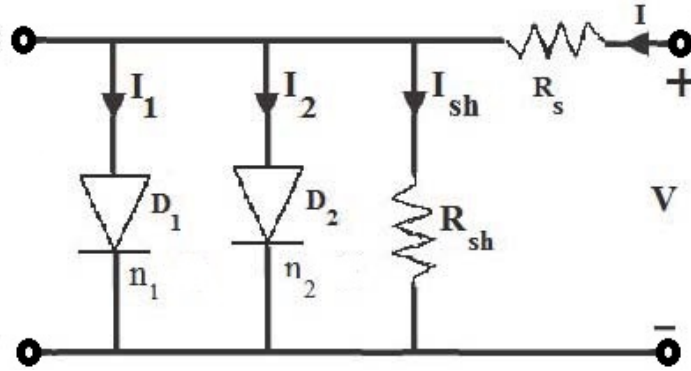


Figure 37: The conventional double-diode model for dark conditions.

Table 5: The electrical parameters extracted from the double-diode model.

$I_{01}(\text{mA})$	$I_{02}(\text{mA})$	$n_1$	$n_2$	$R_{sh}(k\Omega)$	$R_s(\Omega)$
$4.22 \times 10^{-6}$	$3 \times 10^{-11}$	1.7	6.3	98	15.16

are labelled.

The values of  $n$  and  $I_0$  are tabulated in Table 5. For the extraction of electrical parameters the analytical expression of Das et al., using the shape parameters can be extended to this dark measurements [92, 93].

The J-V curves in Fig. 38 and Fig. 39 can be considered in different voltage regions. In each region the different values of ideality factor, saturation current is obtained regarding the appropriate recombination or diffusion process. In the room temperature, if the ideality factor  $n$  is almost constant between  $1 < n < 2$  the interface recombination is dominated current transport. This value of  $n$  depends on the ration of dielectric constants and donor and acceptor concentration ratio. The low  $I_0$  and  $n$  values for room temperature further suggests that the junction interface has relatively less interface state density and thus, the contribution of depletion region recombination increases leading to the depletion region recombination dominating the current transport in this voltage region  $0.45 \text{ V} < V < 0.7 \text{ V}$ . A bigger value of  $n_2 = 6.3$  was observed for the voltage region  $V < 0.45 \text{ V}$ . usually, the idealities greater than 2 are attributed to recombination in the Quasi-Neutral Region (QNR) due to trap-assisted tunnelling and field-assisted recombination. Another reason for the high ideality factors could be attributed to nonlinear contact resistance. Tan et al., suggested that the J-V characteristics in the forward bias direction can be considered in each small voltage region separately [94].

At low voltage region  $0 < V < 0.3 \text{ V}$ , Eq. (12) does not fit linearly to a straight line but it fits with  $I \propto V^{1.4}$  which corresponds to tunnelling and/or Space Charge Limited Current (SCLC). The SCLC can be described by Child-Langmuir law. In the middle voltage region between  $0.3 \text{ V} < V < 0.55 \text{ V}$  the Shockley-Read-Hall recombination through a distribution of trap states within the space charge region could be the source of the diode recombination. This region is relevant to the ideality factors bigger than 1 as we stated above. In high

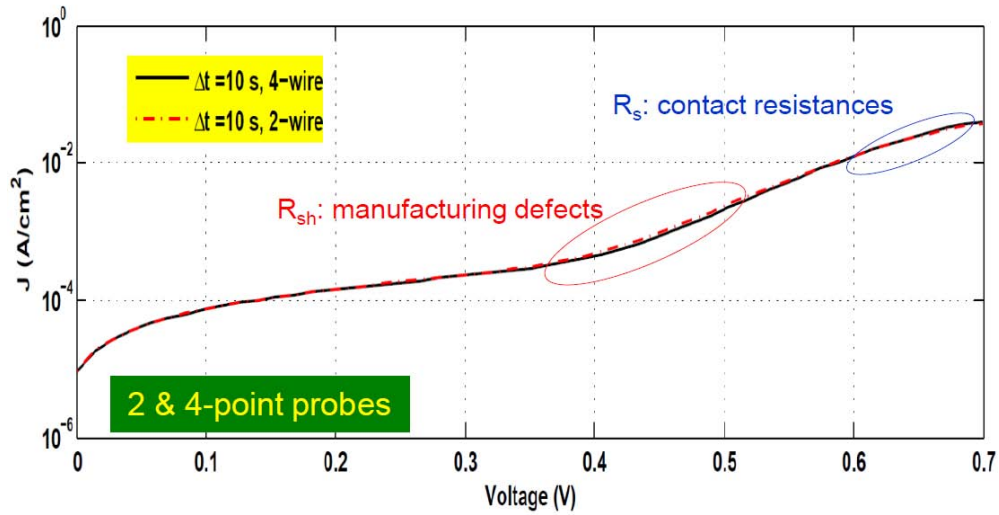


Figure 38: The J-V curve obtained from two and four-points probe technique in dark under forward bias. The results obtained are more precise comparing with the manufacturer's (HZB, Germany) reports.

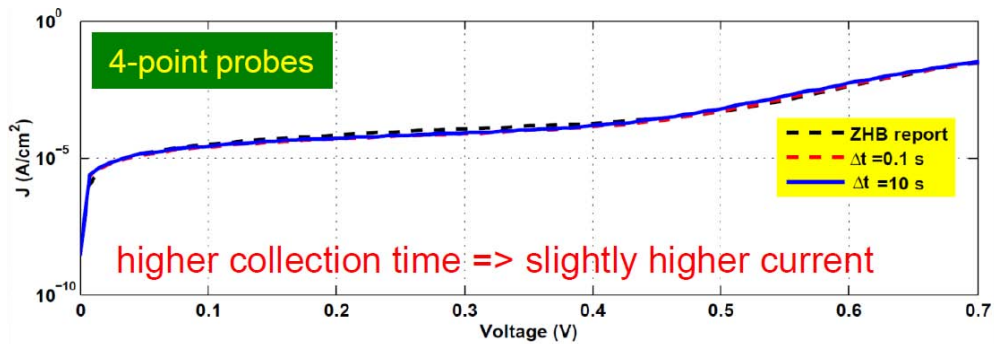


Figure 39: The J-V curve obtained with two and four-point probe technique in dark under forward bias for two different charge collection time  $\Delta t=0.1, 10$  s.

voltage values  $V > 0.55$  V, the SCLC could be dominant. The existence of SCLC could be attributed to the excessive amount of injected carriers which control the space charge and electric field profile of the junction. Under this circumstance, SCLC is dominated by the drift component of injected carriers. This current is described by the Mott-Gurney law. The SCLC in this range suggests an exponential distribution of trap states within the bulk instead of at the interface. This current was suggested to be proportional to  $V^2$ .<sup>43</sup> [95]. Thus, the contribution of a particular process depends on  $I_0$  and  $n$ . If, for instance, a recombination process has a low  $I_0$  and a low  $n$ , it may not carry much current at low voltage. At higher voltage, due to its strong voltage dependence (small  $n$ ), this process may dominate the diode. The other aspect of our analysis was to test the effect of carrier collection time on the J-V curves. The results show a lower current values for  $\Delta t = 0.1$  S in the higher voltage regions. Therefore, higher forward bias can collect the carriers in more efficient way at higher collection times ( $\Delta t = 10$  s). The chance for any recombination is reduced by immediately removing the generated carrier from the recombination path, so increasing the current density.

In summary, using two and four-points probe (four-wire) technique, the dark current-voltage characteristics of CIGS chalcogenide solar cells were derived for two different carrier collection time under forward bias. Device parameters were determined using the two-diode model. The parameters extracted from the dark J-V curve of the solar cells were series resistance, shunt resistance, saturation currents and ideality factors for different voltage regions leading to different current transport domination. For longer carrier collection times a slightly higher current density was obtained at higher voltage ranges.

## Chapter V

### Simulation of CIGS Thin Film Devices

To predict the output performance of thin film devices, their electrical properties can be analysed by means of equivalent circuits that represent the physical phenomena happening in the cell. Some of these phenomena like trap states and grain boundaries act as recombination or generation centres for the minority carriers [96]. One-diode model is usually applied to represent solar cells but it has been reported that using this model the current versus voltage characteristic of solar cells cannot be precisely calculated under low-irradiance conditions [97, 28]. Therefore, in this case, the two-diode model has been proposed for solar cells and the physical phenomena of CIGS solar cells have been introduced in the model [98]. In this section, we develop a four-diode model where the effect of recombination in the trap states and grain boundaries of the absorber region on the performance of the cell is emphasized and discussed. The diffusion and recombination current components of each phenomenon are taken into account. The developed model gives a more reliable insight into the physical behaviour of a CIGS cell. Furthermore, the buffer layer current and impact ionization effects are introduced in the equivalent circuit.

The characteristics of the graded band gap profiles of CdTe and CIGS thin film solar cells have been reviewed by many research groups [99]. Influence of the valence and conduction band grading of the absorber material on the main parameters of the cell have been considered. A new graded band gap profile is proposed which exploits the widening of both valence and conduction bands. Furthermore, we discussed the possibility of conduction band grading of the window material near the surface region to enhance the carrier transfer.

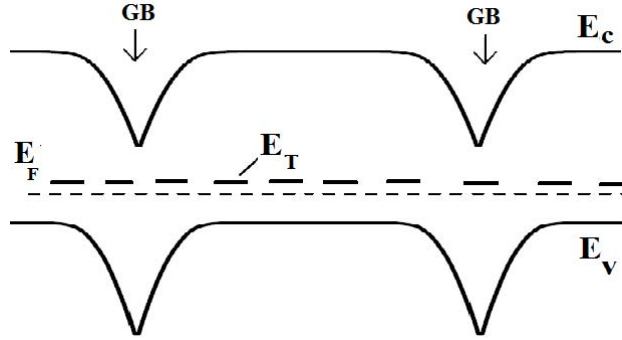


Figure 40: Energy diagram of grain boundaries (GB) and trap states (ET) in the absorber region of a CIGS cell.

### 5.1 Trap states and grain boundaries equivalent circuits modeling

With reference to Fig. 37, J-V is given by,

$$I - I_{ph} + I_1 + I_2 + \frac{V + IR_s}{R_{sh}} = 0 \quad (13)$$

where  $I_{ph}$ ,  $R_{sh}$  and  $R_s$  are the photocurrent, shunt resistance and series resistance, respectively.  $I_1$  and  $I_2$  represent the currents that flow through the diodes D1 and D2 with diode ideality factors  $n_1=1$  for the diffusion current component and  $n_2=2$  for the recombination current component, respectively.

In the following, we propose an extended equivalent circuit model with four diodes to consider the trap state and grain boundary effect on the behaviour of the cell. We have already shown that an effective method of analysis consists in dividing a solar cell into different areas and representing each of these areas with an ideal diode. First, we assume that the cell has two different regions with different current transport mechanisms: the trap state region and the grain boundary region. In this way we can accurately consider the recombination of minority carriers in the trap states located in the semiconductor band gap or in vicinity of grain boundaries. In fact, the recombination in the bulk and space charge region occurs with an exponential distribution of trap states or via a single trap level in the absorber band gap (based on Shockley-Read-Hall model). We call these levels as trap states to differentiate them from grain boundary states.

Grain boundaries are considered as two dimension defects within a polycrystalline structure where two misaligned crystalline grains meet. They usually form during a growth process of a material, when two crystals grown from individual nuclei with different crystal orientation touch each other (Fig. 40).

Grain boundaries may have a large impact on the electrical properties of a polycrystalline semiconductor. Hence even local lattice distortions or composition changes may influence the current recombination or current transport behaviour through the correlated potential barriers or wells. We take the effects of generation or recombination centres into account, with additional resistances in the equivalent circuit as the electrical resistivity is increased in their vicinity [100, 101]. The resistances  $R_{ST}$  and  $R_{SG}$  are introduced

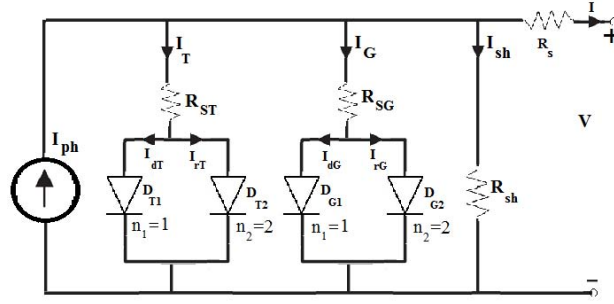


Figure 41: Four-diode equivalent circuit considering the trap state and grain boundary's shunting effects.

and each of them are connected in series with the parallel of two diodes as it is shown in the circuit model of Fig. 41. Then, the Eq. (4) changes to,

$$I - I_{ph} + I_T + I_G + \frac{V + IR_s}{R_{sh}} = 0 \quad (14)$$

where  $I_T$  and  $I_G$  are the trap state and grain boundary currents as,

$$I_T = I_{dT} + I_{rT} \quad (15)$$

$$I_G = I_{dG} + I_{rG} \quad (16)$$

Each of these currents includes two components for the diffusion and recombination phenomena indicated with subscripts d and r, respectively. The trap state recombination depends on the doping concentrations, energetic and spatial distribution of the recombination centres [100, 101]. In the equivalent circuit we separate the diffusion current component of trap state area from the recombination one. Obviously, this area opposes to the grain boundary region. We allocate diodes  $D_T$  for the trap state area and  $D_G$  for the grain boundary region. The current components can be expressed by,

$$I_{dT} = I_{0dT} \left\{ \exp \frac{q(V + IR_s + I_T R_{sT})}{n_1 kT} - 1 \right\} \quad (17)$$

$$I_{rT} = I_{0rT} \left\{ \exp \frac{q(V + IR_s + I_T R_{sT})}{n_2 kT} - 1 \right\} \quad (18)$$

$$I_{dG} = I_{0dG} \left\{ \exp \frac{q(V + IR_G + I_G R_{sG})}{n_2 kT} - 1 \right\} \quad (19)$$

$$I_{rG} = I_{0rG} \left\{ \exp \frac{q(V + IR_G + I_G R_{sG})}{n_2 kT} - 1 \right\} \quad (20)$$

where  $I_{0dT}$ ,  $I_{0rT}$ ,  $I_{0dG}$  and  $I_{0rG}$  are the diode saturation currents,  $q$  is the electron charge,  $k$  is the Boltzmann constant,  $T$  is the absolute room temperature and  $n_1=1$  and  $n_2=2$  are the diode ideality factors. The diffusion and recombination saturation currents are given by [102].

Table 6: The typical values reported in literature for the parameters of the modified 4-diode model.

$R_{sh}$ (k $\Omega$ )	$R_s$ ( $\Omega$ )	$I_{0dT}$ (nA)	$I_{0rT}$ ( $\mu$ A)	$I_{0dG}$ (nA)	$I_{0rG}$ (nA)
820	8	0.28	8.05	1	0.02

$$I_{0dT} = q \sqrt{\frac{D_{nT}}{\tau_{nT}}} \frac{n_{iT}^2}{N_A} S \quad (21)$$

$$I_{0rT} = qW \frac{n_{iT}}{2} \sigma_T \nu_{th} N_T S \quad (22)$$

$$I_{0dG} = q \sqrt{\frac{D_{nG}}{\tau_{nG}}} \frac{n_{iG}^2}{N_A} S \quad (23)$$

$$I_{0rG} = qW \frac{n_{iG}}{2} \sigma_G \nu_{th} N_G S \quad (24)$$

In (6)-(9),  $v_{th}$  is the thermal velocity,  $S$  the cell surface area,  $W$  the depletion region width and  $N_A$  the acceptor density.  $N_T$ ,  $N_G$ ,  $n_{iT}$  and  $n_{iG}$  are the density and the intrinsic carrier density of trap states and grain boundaries, respectively.  $D_{nT}$ ,  $D_{nG}$ ,  $\tau_{nT}$ ,  $\tau_{nG}$ ,  $T$  and  $G$  are the diffusion constant, lifetime and capture cross-section for the trap states and grain boundaries, respectively. Currently, it has not been possible to extract the parameters of the equivalent circuit shown in Fig. 41 fitting (2) to the measured current versus voltage characteristics through an optimization algorithm. Nevertheless, in several published papers [103], the order of magnitude of some of these parameters is presented. In Table 6 the values indicated in the literature are reported.

The saturation current of the diffusion component of the trap states is negligible in comparison with that of the recombination component. Moreover, the saturation current of the recombination component of the grain boundaries has a negligible value compared with the one of the diffusion component. Clearly, even if one deletes the circuit elements of the model shown in Fig. 41 whose parameter values are small, the conventional two-diode model is not obtained due to the presence of the resistances  $R_{ST}$  and  $R_{SG}$ . However, the four-diode model is useful because it allows a careful insight into the physical behaviour of the cell.

## 5.2 Equivalent circuits modified for buffer layer and Auger generation phenomena

Here, we propose an equivalent circuit including the recombination in the junction between the buffer and the window layer (i. e. ZnO) [104, 105] and the generation due to the impact ionization effect in the absorber material (Fig. 42) [106]. This equivalent circuit contains two nonlinear controlled current sources and, for simplicity, is obtained from the conventional two-diode model of Fig. 43. Other circuit elements could be added to take account of other phenomena, for instance, the tunnelling recombination currents or high resistance windows layers.

So, for this model, the current-voltage equation contains an additional term for the recombination current

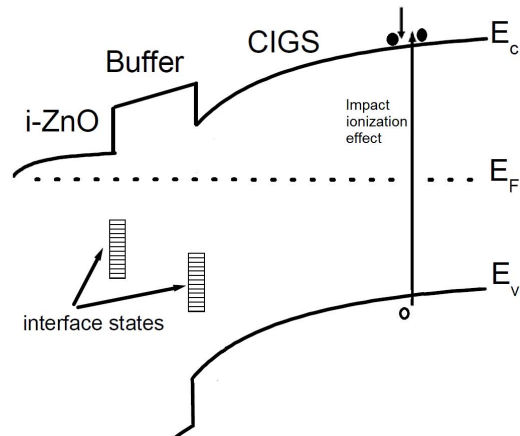


Figure 42: Buffer layer interface states and Auger generation effect in a CIGS solar cell.

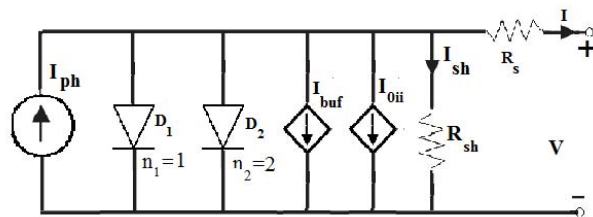


Figure 43: Equivalent circuit including the recombination current at the buffer layer and Auger generation process.

in the buffer layer [106]

$$I_{buf} = I_{ph} \frac{d_{buf}^2}{(\mu\tau)_{eff}[V_{bi} - (V + IR_s)]} \quad (25)$$

where  $d_{buf}$  is the thickness of the buffer layer over the effective drift length  $(\mu\tau)_{eff}[V_{bi} - (V + IR_s)]$ . In the term  $(\mu\tau)_{eff}$ ,  $\mu$  is the mobility of carriers and  $\tau$  is the recombination lifetime at the interface between the buffer layer and the absorber layer.  $V_{bi}$  is the built-in voltage in the cell. The recombination current in the buffer layer is given by the right-hand side of (14); and can be represented in the circuit of Fig. 43 through a nonlinear controlled current source  $I_{buf}$ , being the controlling quantity the voltage across the shunt resistance. As final case, another physical phenomenon for the photocurrent generation in CIGS solar cells can be the impact ionization mechanism in which the energy of an electron returning from the higher levels of the CB to the CB edge is used to pump another electron from the VB to the CB as shown schematically in Fig. 42. Therefore, the additional impact ionization term for the reverse current is given by [107].

$$I_{oii} = qm n_i^3(V)U \quad (26)$$

where  $m$  is the multiplication factor per surface and time ( $\text{cm}^6/\text{s}$ ),  $U$  is the volume of the cell and  $n_i$  is the intrinsic carrier density which is a function of the cell voltage ( $V$ ). In the circuit model of Fig. 42 the reverse current can be represented with a nonlinear voltage controlled current source  $I_{oii}$ .

The conventional model for these devices is simple and needs some additional terms according to the physical phenomena under consideration. We consider two of these physical phenomena that are likely to happen in the CIGS solar cells and have not been considered in equivalent circuit models yet. For example, the effect of the recombination in the single or multi trap states and grain boundaries both in space charge region or/and absorber bulk region. For each phenomenon, the diffusion and recombination currents are taken into account through a parallel of two diodes in the equivalent circuit in order to obtain a precise evaluation of the carriers transfer in the cell. So, a modified equivalent circuit with four diodes instead of two is presented.

Two additional resistances are also added to model the mentioned two areas, as these areas create resistivity, i. e. near the trap states and grain boundaries. Furthermore, the role of the buffer layer between the window and the absorber layer and the impact ionization effect are also considered in the equivalent circuit. The model allows an assessment of the effects of the recombination current in the buffer layer and the current source from the impact ionization phenomenon as effective mechanisms to increase the conversion efficiency of the cell over the Shockley-Queisser limit. A clear assignment to each additional branch in the equivalent circuit enables the evaluation of the influence of the corresponding phenomenon on the solar cell performance.

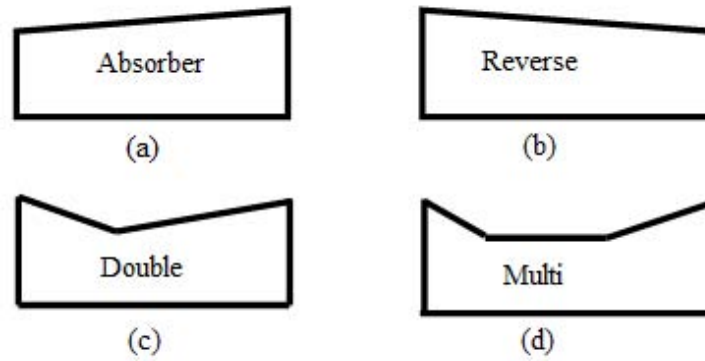


Figure 44: The possible CB graded profiles for the CIGS thin film solar cells.

### 5.3 Band gap grading of the CIGS thin film solar cells

$\text{Cu}(\text{In,Ga})(\text{S,Se})_2$  (CIGS) thin film solar cells have low cost and potentially high efficiency. The record efficiency of about 19.9 % has been achieved in laboratory scale [108]. To improve the device performance, the electronic and optical properties of the cell have to be optimized. Band gap grading of the cell materials is effective on reducing the recombination losses and amplifying the carrier collection in the cell [109, 110]. In this section, we review the characteristics of the last proposed graded band gap profiles and then, due to valence and conduction band widening effects on the performance parameters of the cell, we present a new graded profile in which the band gap widening of the absorber is included both in Conduction Band (CB) and Valence Band (VB). Widening the band edges at front and back regions of the cell is considered. Furthermore, we discuss the benefit of the CB grading of the window material near the interface region to enhance the carrier passivation and transfer through the cell.

### 5.4 Valence band grading

In this section, a brief review on the characteristics of the graded profiles is discussed. As early as 1960, Wolf proposed a graded band gap semiconductor for solar cell applications [111]. He proposed that as grading the band gap of the absorber material, the carrier collection improves with an increased quasi-drift electrical field in the Space Charge Region (SCR) of the cell. During the last decade, the following graded profiles have also been proposed (Fig. 44):

*Normal Grading:* Increasing gradually the Ga content ( $0 < x < 3$ ) [112] in the  $\text{Cu}(\text{In}_{1-x}\text{Ga}_x)\text{Se}_2$  compound, the band gap of the absorber linearly increases by linearly decreasing the electron affinity through the absorber [113]. In this case, the gradient in the Ga concentration produces a gradient in the electron

affinity which is accompanied by a quasi-electric field through the cell (Fig. 44a). This additional electrical field enlarges the diffusion length of the electrons. Therefore, the carrier collection will enhance and helps the minority carriers to be collected. On the other hand, widening the band gap at the back contact of the cell reduces the recombination rate at the metallurgical contact and raises the  $V_{oc}$  of the cell due to lower recombination current (saturation current) in higher band gap locations. Finally, the small enhancement in efficiency is due to enhanced carrier collection and a decreased recombination rate. Unfortunately, the  $J_{sc}$  decreases steadily by linearly increasing the band gap as the absorption coefficient depending on position decreases.

*Reverse grading:* With gradually decreasing Ga content through the absorber layer, the band gap of the cell is also reduced (Fig. 44b) [114, 115]. With linearly decreasing band gap toward the back contact, the recombination rate at back contact increases, but in the SCR, the  $V_{oc}$  is high due to widened band gap and lower recombination rate. In this profile,  $J_{sc}$  increases steadily due to increase in the absorption for smaller band gaps, but it is not significant due to reduced probability of the electron collection affected by a reverse quasi-electrical field [116].

*Double grading:* In a double graded band gap profile, the efficiency depends on the location of the minimum point of the band gap. In this profile, Ga content decreases from front surface to an optimum minimum position and then increases to back contact (Fig. 44c). Both kinds of grading affect the carrier collection probability. Front grading repels minority carriers away from the interface and back grading increases the band gap which enhances the carrier collection by drifting the carriers to the SCR due to additional electrical field. Therefore, the internal quantum efficiency and position dependent light absorption are increased and improve the  $J_{sc}$ . Anyway, the maximum band gap at the back contact will have to be optimized in order to obtain an improved short circuit current density. Without back grading, the internal quantum efficiency is lowered due to the lack of quasi-electrical field which helps the photo-generated carriers to reach the contacts. The optimization of band gap grading in CIGS shows an absolute gain in efficiency up to 3 % [117].

*Multi – Grading:* Multi-graded band gap structure has showed a better performance than other cases (Fig. 44d). In this case, an improved  $V_{oc}$  at front region and an improved  $J_{sc}$  at the back region are obtained. The cell has been simulated to give an efficiency up to 19.83 % theoretically and 18.8 % experimentally [117, 118]. All above discussed graded band gaps can be obtained by changing the Ga content in the absorber compound. The other possibility to grade the band gap can be grading the VB of the absorber [119]. Some of the authors have also considered the VB grading effects on the cell performance parameters. In Fig. 45, Decock et. al., proposed an absorber with grading towards the SCR with S and grading the back contact with Ga [120]. Grading the absorber material can be conducted by both front S and back

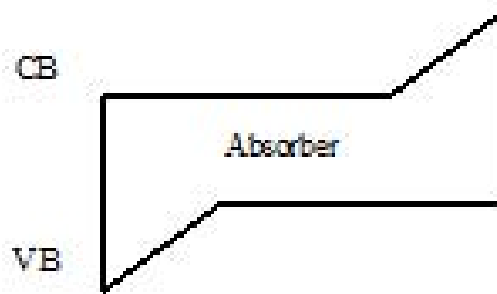


Figure 45: Grading both valence (front) and conduction (back) bands.

Ga-grading in the  $\text{Cu}(\text{In}_{1-x}\text{Ga}_x)(\text{Se}_{1-y}\text{S}_y)_2$  solar cells.

The integration with S affects both the CB and VB. The exact distribution between CB and VB offset is however complicated and, therefore, they assumed that by S-grading of the surface region, the CB stays flat and VB is widened. Also, a Ga graded layer anticipated for back region to enlarge the CB only by neglecting the VB offset in back region. Anyway, in this analysis, small benefit for grading both the front and back regions is attained because grading benefit depends on the perfect control of the defect and doping distributions, appropriate absorber thickness and many other parameters [121]. However, authors are agreeing that with optimization of the cell parameters, the graded profile will enhance the advantage of the generation and recombination rate in the cell. Finally, the authors assessed grading as successful if it reshapes the generation profile in a way that more charge carriers are generated in regions with less recombination probability.

Here, we propose a CIGS thin film solar cells with VB and CB grading in the space charge region and back surface region of the absorber layer. In all the examined profiles the VB widening effects on the performance parameters by promoting the carrier transformation, hole passivation and carrier collection in the cell are considered. On the basis of the results, an optimal graded band gap structure is proposed and considered with a design closer to the reality where the VB offset is created during the band gap grading processes. We take the effect of both VB and CB widening on the cell parameters into account. For each profile considered, efficiency ( $\eta$ ), open-circuit voltage, short-circuit current density and fill factor (FF) are optimized versus the thickness of the absorber material. To consider the band gap widening at the front surface of the absorber material, the interface between the CdS buffer layer and CIGS absorber is supposed to be a high recombination interface [117]. To grade the front and back surfaces of the absorber material, additional compositions of In, Ga, S or Se during the third stage of the deposition process along with a Cu-poor surface are used. For the calculations and simulations, the data are taken from the literature or

chosen in reasonable ranges. The band gap of the  $\text{Cu}(\text{In}_{1-x}\text{Ga}_x)(\text{Se}_{1-y}\text{S}_y)_2$  is given by [118],

$$E_g = 0.95 + 0.8x - 0.17y - 0.05y(1 - y) \quad (27)$$

The VB offset can be taken as 20 % of  $E_g$  due to  $x$  and 80 % of  $E_g$  due to  $y$ . Ga incorporation increases the CB of the absorber with a slight lowering in the VB. On the other hand, S incorporation or Cu-poor surface layer affects largely the VB and less increases the CB. In Fig. 46 the performance parameters of the five considered profiles obtained with AMPS-1D are shown. In profiles 1 and 2 we assume that the  $E_g$  widening is happening in the VB only. The VB offset can be produced with the intentional Cu-depletion or Ga distribution in the surface region. This grading decreases the diode current and so the recombination rate which improves  $V_{oc}$  and FF of the cell. This grading retains  $J_{sc}$  owing to a lower absorption of photons in the cell by enlarging the band gap low carrier collection for the electrons. In profile 3,  $E_g$  has a VB and CB shift at back surface contact. This kind of band gap widening can be seen in Cu-poor surface phases (i. e.  $\text{Cu}(\text{In,Ga})_3\text{Se}_5$ ) [117]. The CB offset almost does not change  $J_{sc}$  but increases  $V_{oc}$  to an optimum value.

In addition, the VB widening causes depletion of holes at the interface that increases  $V_{oc}$ . Once sufficient holes concentrations are provided to the surface region,  $V_{oc}$  is limited to an optimum value. Note that increasing the CB reduces the minority carrier transport ability which leads to a lower conversion efficiency. In fact, a CB grading at the front surface is not enough to deactivate the interface recombination unless the band alignment is completely changed. The reason is that a CB does not change the interface band gap. The hole barrier remains unchanged. In profile 4, we propose a back graded profile that can be incorporated from a high Ga content ( $x=0.3$ ) or S content (from  $y=0$  to  $y=0.3$ ) in the back region of the absorber. In this case a quasi-electric field arises at the back region and aids the photo-generated minority carriers to go away from the surface so that they can be collected and contribute to the photocurrent. So, in this case the recombination rate in the back region is reduced and the effective diffusion length of the minority carriers is improved. For this profile  $J_{sc}$  and  $V_{oc}$  are improved and the efficiency improves as well.

In profile 5, which is the last proposed profile, graded VB and CB are fractionalized at both sides. In this optimal profile hole depletion at both front and back surfaces is anticipated. Grading of both sides establishes a quasi-electric field that can reduce the recombination rate at both surface sides for electron and hole carriers improving  $V_{oc}$ . Therefore,  $J_{sc}$  and then  $\eta$  are enhanced. The effect of the VB widening is the hole passivation at the contacts with barrier height reduction and hole density lowering in these regions so increasing the effective diffusion length of the carriers and  $J_{sc}$  because of the sensitivity of the graded absorber devices to the hole density.

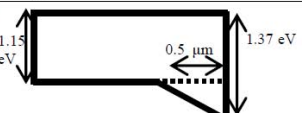
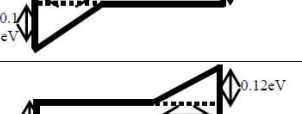
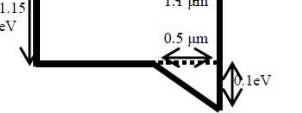
	<b>Graded band gap profile (Absorber thickness= 2 <math>\mu\text{m}</math>)</b>	$\eta$ [%]	$V_{oc}$ [mV]	$J_{sc}$ [mA/cm <sup>2</sup> ]	FF [%]
1		16.5	0.632	34.1	76.8
2		16.1	0.622	34.0	75.8
3		17.5	0.689	32.3	79.1
4		16.9	0.667	34.4	74.5
5		18.2	0.668	34.4	79.5

Figure 46: The optimized geometrical and electrical parameters of the graded VB CIGS solar cells.

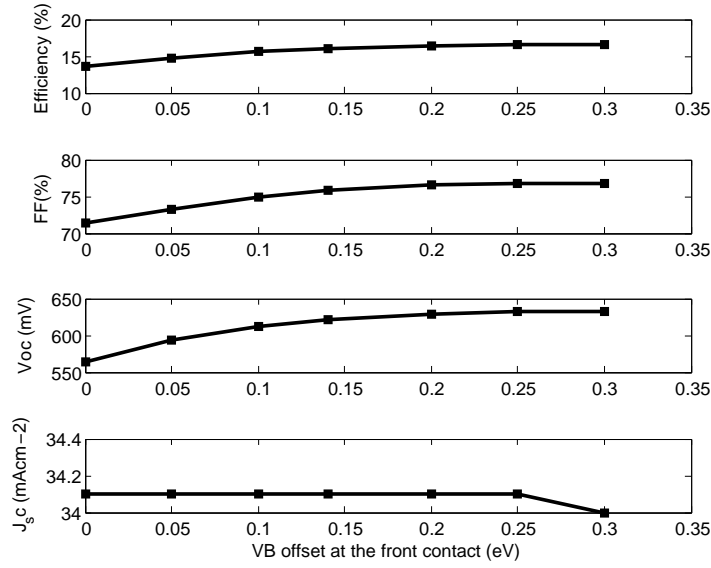


Figure 47: Effect of VB offset at the front contact on the cell parameters.

## 5.5 Conduction band grading

Due to the downward VB shift at the surface region, the band gap of the absorber at the surface region of the cell is at least 0.1 eV greater than that of the bulk region. This shift in the VB can be produced by Cu-poor surface phases (i. e., by  $\text{Cu}(\text{In,Ga})_3\text{Se}_5$  or by intentional Ga/In/Se/S grading [15]. In this profile the VB kept fixed while the conduction band offset increases to widen the band gap. However, many of the papers have theoretically and experimentally stated that the VB offset is effective on the main parameters of the cell, where the  $V_{oc}$  will improve by enlarging the barrier high at the surface region by grading the VB at interfaces. For example, Gloeckler and Sites evaluated the effects of VB widening at the surface of a Cu-poor surface and showed that hole depletion at the surface regions by VB offset is the crucial parameter in achieving high  $V_{oc}$  at the CdS/CIGS interface [103]. This is due to the hole concentration which is a limiting parameter for recombination rate on the junction surface and can be controlled by VB grading. When sufficient holes are supplied at the interface, they can limit the  $V_{oc}$ .

Analytical findings also verify that the VB position at the interface can limit the  $V_{oc}$ . The VB offset induced by S/Se alloyed Cu-poor material, can increase the barrier high at the interface and lower the recombination rate of the carriers there [122]. They concluded that a large VB offset of 0.4 eV can directly increase the barrier to a sufficiently large value which can eliminate interface recombination. In Fig. 47 we show the VB effects on the cell parameters based on data reported in [123, 124]. The curves prove that the VB widening improves the cell parameters with the exception of  $J_{sc}$  by reducing the carrier loss and

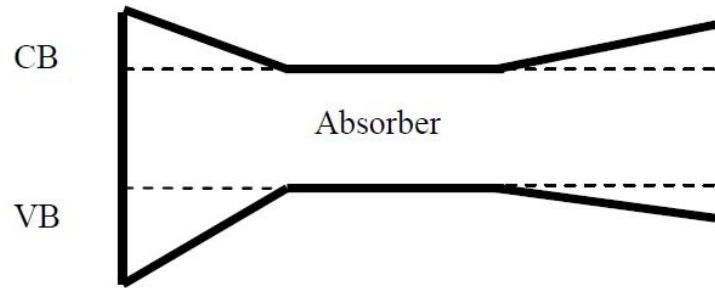


Figure 48: Graded band gap considering the VB offset.

hole depletion at the surface regions. Therefore, based on the above approaches, we present an improved graded profile, considering the valence and conduction band offsets at both sides of the absorber of the cell (Fig. 48).

The last profiles consider just one kind of grading that cannot be close to the real changes during grading the Ga or S contents in the absorber. For example, S variations in an absorber of  $\text{CuIn}(\text{S},\text{Se})_2$  material influences both the valence and conduction bands [125]. However, the exact distribution between CB and VB offsets at the different regions of the cell is complicated and should be optimized for the different doping and defect densities. The proposed model is a real one based on the changes in the VB and CB together, which can be produced by doping the absorber with Ga, Se or S [120, 125]. We suggest that grading will lower the VB edge in both sides of the absorber in Fig. 48; we state that the VB offset at the back contact aids the holes, as majority carriers of the absorber, to reach the contact. For a  $\text{CuIn}(\text{S},\text{Se})_2$  absorber material, a suitable improvement in the  $V_{oc}$  can be obtained by an appropriate doping concentration of the S or Se. Moreover, a S-rich surface and a Se-rich back region, can provide a good overlap between the band gap of the absorber and solar spectrum (1.5 and 1.1 eV, respectively). It should be noticed that by doping the absorber material, the VB offset becomes greater than that of the CB [126].

At the back surface, grading the band gap with S leads to widening of both VB and CB with a larger value of VB offset. The performance of this profile is enhanced due to the advantages of the offsets in the junction regions. VB widening at the surface region has a main effect on the performance parameters of the cell. VB offset reduces the saturation current at the surfaces which is accompanied with a hole depletion by the barrier height enlarging and hole passivation enhancement. On the other hand, the CB produces a quasi-electrical field which repels the electrons from the surface region. At the back region, CB offset assists the minority carriers to be collected and contribute to the current. However, this profile seems to be closer to reality as a graded absorber profile where both CB and VB offsets have been considered. For example, inserting the defects in the front and back surfaces will lead to the offset in both the band edges which shapes the proposed profile in Fig. 48 [127].

## 5.6 Graded window layer

One of the effective factors on the performance of the CIGS solar cells is the CB offset between the window layer and absorber layer at the interface. Recent calculations of the electron affinity difference between the window and absorber layers showed that the CB minimum of the absorber is below that of the window. In this state, a spike occurs in the CB at the interface which is accompanied by a widening of the window CB. Further considerations have shown that this spike can improve the  $V_{oc}$  of the cell due to lowering the recombination of the electrons of the window and holes of the absorber at the interface [128].

The CB offset between the window and absorber can be also a cliff which reduces the efficiency due to increasing the recombination current at the interface. For the case of spike, however, a lower  $J_{sc}$  is obtained which is due to the barrier against transferring the photo-generated electrons from the absorber to the window, anyway, the existence of a suitable spike in the interface increases the barrier against the injected electrons at the interface and, therefore, decreases the entire buck current density and enhances the  $V_{oc}$  of the cell. We propose the grading of the CB of the window at the surface region to enhance the carrier transferring ability.

Slightly increasing the CB towards the interface of the window results in a gradient in electron affinity and conducts the electrons to leave the interface which increases both filling factor and conversion efficiency. In this way the photogeneration current will be enhanced. This grading can be obtained by n-doping of the window material. For example, by n-doping of the CdS window of the CdS/CIGS solar cell [129] or variation of the Mg content at the surface region of the window of a ZnMgO/CdS/CIGS cell [130].

In summary, we considered the characteristics of the available graded band gap profiles of the CIGS solar cells. We propose and discuss the possibility and advantages of a new improved graded profile where both the valence and conduction bands have been considered at both sides of absorber. At the front region of this profile, VB widening will enlarge the hole depletion as a limiting factor for  $V_{oc}$ , CB grading will reduce the recombination rate of the carriers at the interface. At the back region, VB grading will enhance the transfer ability of the majority carriers and CB will improve carrier collection probability of the carriers to contribute to the current. However, this profile can better define the grading changes on the valence and conduction bands, e. g., for a S-graded absorber material. We also discuss the possibility of grading the front region of the window layer to enhance the passivation and transfer of the electrons coming from the absorber.

## Chapter VI

### Modeling the Transport Mechanism in CIGS Thin Film PV Devices

A simple model for the photocurrent density of a linearly graded band gap  $\text{Cu}(\text{In,Ga})\text{Se}_2$  solar cell is presented. Both generation and recombination mechanisms in the space charge region and absorber region of the cell are considered. The carrier collection function and effective absorption coefficients are introduced in the calculations to obtain a more realistic model. The results show that photocurrent density of the graded band gap solar cell is higher than in that with a constant averaged band gap. There is an optimum for grading strength or band gap widening of the absorber region. Recombination current reduces the photocurrent density with a lower reduction in the absorber material than in the depletion region. For longer diffusion lengths (or greater values of carrier collection factor), a higher photocurrent density is obtained except where collection probability is already unity everywhere in the absorber.

The effect of Auger generation on the thermodynamic efficiency of a reverse graded band gap  $\text{Cu}(\text{In,Ga})\text{Se}_2$  thin film solar cell is studied using a detailed balance approach. For the graded profile (1.5-1 eV), a wider range of photons can be considered as high energy photons to produce hot electrons which can pump an additional electron from the valence band to the conduction band. The effects of the carrier multiplication probability,  $P$ , and grading strength of the front band gap on the variation of efficiency are studied. Auger mechanism is more effective at lower band gaps due to higher multiplication probability. A thermodynamic efficiency of about 41% is obtained, which is higher than the maximum efficiency of 31% for a graded band gap cell without Auger generation. Moreover, we study the effect of Auger generation on the current-voltage characteristics of the cell. The carrier multiplication increases the short-circuit current due to the increased photogenerated electrons and almost does not change the open-circuit voltage. However, the band gap grading enhances the open-circuit voltage by reducing the recombination rate. Also, a known result is the red shift in the optimum band gap towards a lower band gap (1.15 eV) with respect to the Shockley-Queisser limit.

## 6.1 Transport mechanism in CIGS devices

In the last few years,  $\text{Cu(In,Ga)Se}_2$  (CIGS) thin film solar cells have shown a record efficiency of about 20.1% in laboratory scale [131]. As potentially efficient and low cost materials, many groups are working on the electrical and optical properties of these types of solar cells [132]. To enhance the electrical properties, (e. g., transport properties of the carriers), the recombination mechanisms and electronic loss effects of the cell have been considered. To promote the optical properties of the cell, the experiments evidenced that grading the band gap of the absorber material improves the device performance [133].

Along with the experimental works, the numerical modelling and simulation of CIGS solar cells have also been developed using programs such as SCAPS [62], AMPS [118] etc. Analytical approaches for modelling and determination of the cell parameters help to achieve a clear understanding of the physics of these structures which is necessary for design strategy and its optimization. Grading the conduction or valence band influences the recombination and generation mechanisms, light absorption process and the carrier collection of the cell (by an induced reverse quasi-electric field through the absorber material) [145].

In the current section, we consider a graded band gap CIGS solar cell with a linearly increased CB toward the back contact (Fig. 49). This profile is interesting to be considered because increased grading toward the back contact leads to enhanced carrier collection with a limit in the immediate vicinity of the metallurgical back interface due to high recombination velocity. Dullweber et al showed that this grading of the absorber material enhances the carrier collection of the cell and absorption of the long wavelength light [118]. In the literature, some of beneficial effects of this profile have been underlined [146, 147].

Mattheis et al have considered a semi-analytical theoretical model for quantum efficiency of this profile to investigate the back contact recombination velocity as well as the optical and electronic parameters of its absorber layer [146]. Decock et al., have derived a closed form analytical expression of the current density including a quasi-electrical field component originating from this grading [134]. In their analysis they assumed the absorption to be constant and neglected the recombination current.

In this section, we present an analytical model to analyse the photocurrent of this profile considering absorption coefficient, generation and recombination rates and carrier collection function relating their dependency to the thickness of the cell. Our theoretical approach considers the photocurrent density of the cell similar to Acevedos method, but in his calculations he considered the ideal photocurrent of the cell only, neglecting the recombination current, assuming 100% carrier collection efficiency and supposing that all photons reach the absorber without any generation or recombination in the SCR [148]. We take into account the recombination and generation currents in the SCR and absorber region of the cell. For different values of grading strengths and diffusion lengths (or carrier collections), we calculate the photocurrent density of the cell and the influence of recombination currents on this quantity. Furthermore, we compare the photocurrent density of the graded band gap and constant averaged band gap cells.

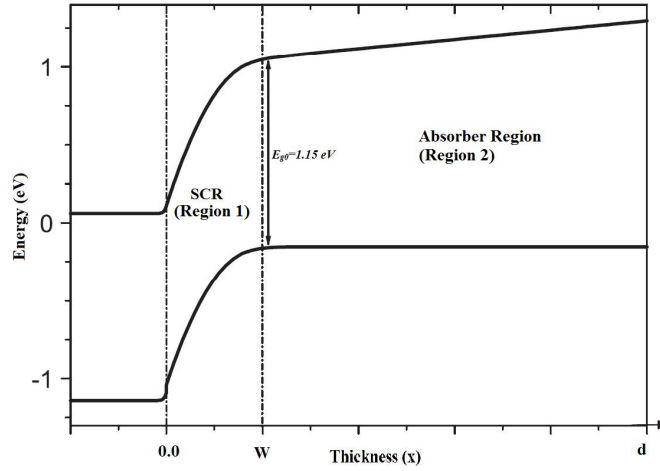


Figure 49: Band structure of linearly graded solar cell divided to SCR (region 1) and absorber region (region 2).

## 6.2 Photocurrent density

In Fig. 49, we divided the cell into SCR (from 0 to  $w=0.4 \mu\text{m}$ ) and absorber region (from  $w$  to  $d=2 \mu\text{m}$ ). For each region, we calculate the photocurrent density which depends on the recombination and generation rates. We assume that the increase of the band gap is due to grading the CB only with a grading strength ( $kT\zeta$ ). Then, the graded band gap is  $E_g(x) = E_{g0} + kT\zeta x$ , with  $k$  the Boltzmann constant,  $T$  the temperature and  $E_{g0}=1.15 \text{ eV}$ . For the incoming light from the left the total photocurrent density of the cell, we can write;

$$J_{tot} = J_1 + J_2, \quad (28)$$

where,  $J_1$  and  $J_2$  are the photocurrent densities of the SCR (region 1) and absorber region (region 2), respectively. The photocurrent density of each region is assumed to be proportional to the integral of the difference between the generation and recombination rates;

$$J_1(x) = -q \int_0^w (G_1(x) - U_1(x)) dx, \quad (29)$$

$$J_2(x) = -q \int_w^d (G_2(x) - U_2(x)) dx, \quad (30)$$

where  $q$  is the electron charge,  $U_1$ ,  $U_2$ ,  $G_1$  and  $G_2$  are the recombination and generation rates in the SCR and absorber region, respectively. In the absorber region, we use an energy and position dependent absorption coefficient  $\alpha(E,x) = A (E - E_{g0} - kT\zeta x)^{1/2}$  where  $A = 10^4 \text{ (cm}^{-1} \text{ eV}^{-1/2})$  is a constant. To calculate the generation rate, we need the number of photons per unit of area at the surface of the cell  $F_0$ . If the sun

is assumed to be a blackbody at  $T_S = 5760$  K,  $F_0$  is given by [135]

$$F_0(E) = [2\pi/c^2h^3] \int E^2 dE / [\exp(E/kT_s) - 1], \quad (31)$$

For the generation rate in SCR (region 1), we assume the following expression;

$$G_1(x) = \int_0^w F_0 \alpha \exp(-\alpha x) \eta_{c,1} dE, \quad (32)$$

where  $\alpha$  is the absorption coefficient in SCR and  $\eta_{c,1}$  is the carrier collection function of the SCR region. In SCR it is assumed that the absorption coefficient is constant ( $\alpha_1 = 10^5 \text{ cm}^{-1}$ ). Choosing this constant value for absorption coefficient in SCR leads to a minimum depletion width of  $0.4 \mu\text{m}$  corresponding to an acceptor density of  $2.75 \cdot 10^{16} \text{ cm}^{-3}$ . The maximum generation rate is obtained if we integrate over the solar photon spectrum and neglect all loss mechanisms due to optical and electrical losses. The most important electrical loss is due to charge carriers which undergoes recombination. Then, we consider the recombination rate as the only loss mechanism in the cell. For  $U_1$ , we assume equal lifetimes for holes and electrons ( $\tau_n = 1000$  ns, doping density of  $10^{15} \text{ cm}^{-3}$ ) with a trap energy level equal to the intrinsic Fermi level. Under forward applied voltage, the recombination rate in the SCR is given by [136];

$$U_1(x) = (q\eta_{c1}(x))(np - n_i^2) / [2\tau_n(n + p + 2n_i)], \quad (33)$$

where  $n$  and  $p$  are the minority and majority carrier densities in SCR, respectively,  $n_i$  is the intrinsic carrier density. Current transport in hetero-junction solar cells under dark conditions occurs as a consequence of different mechanisms. Ideally, the dominant current transport mechanism is carrier injection at the junction and diffusion due to a carrier gradient caused by recombination at the bulk and surface of the respective material at each side of the junction. However, in real non-ideal junctions, other mechanisms are present, such as recombination caused by traps at the junction interface enhanced by tunnelling, or due to Shockley-Read-Hall (SRH) recombination at deep levels within the space charge region of the junction. Furthermore, for the case that we consider the minority carrier density ( $10^{15} \text{ cm}^{-3}$ ) with recombination lifetime of (1000 ns) will cause a dominated radiative recombination current. The novelty in this equation is the introduction of carrier collection function  $\eta_{c,1}(x)$ , which gives the position dependency to the recombination rate.  $\eta_{c,1}(x)$  represents the mean probability of an electron or hole crossing the region without capture and recombination to be collected at the contacts. Usually, this parameter is assumed to be unity or in the range 0-1 in SCR [146, 147]. In the absorber region (region 2) with a graded band gap, we have;

$$G_2(x) = \int_w^d F_0 \alpha(x) \exp[-\alpha(x)x] \eta_{c,2} dE, \quad (34)$$

For this case we neglect the terms [1-R( $\lambda$ )] and [1-S( $\lambda$ )] where R( $\lambda$ ) and S( $\lambda$ ) are the reflection and grid-shadowing factors, respectively. These parameters are obtained by optical measurements [137]. In the absorber region,  $\eta_{c,2}(x)$  cannot be assumed as unity and it changes at absorber edges. In advanced state,

for a p-type absorber, with  $n \ll p$  and trap level at mid-gap, the carrier collection coefficient is a function of diffusion length of electron minority carriers, diffusion coefficient and surface recombination velocity as well as recombination lifetime of the electrons. Increasing grading strength, significantly increases carrier collection by the additional quasi-electric field. This additional electric field increases the diffusion length of the carriers and enhances the carrier transfer in the cell [139]. However, high ratio between the back contact recombination velocity and the diffusion coefficient limits the minority carrier collection at the back contact [146]. In case the absorber thickness is close to diffusion length ( $L_n$ ), the quasi-Fermi levels linearly change and the carrier collection function can be expressed by [137]

$$\eta_{c,2}(x) = \exp[(x + w)/L_n], \quad (35)$$

This function is the unique function of the device geometry and is independent of the generation rate. We propose this simple function for carrier collection factor to avoid the model to be complicated. Generally, this parameter assumes as unity in the theoretical works, however, this parameter depends on a variety of parameters like surface recombination velocity, diffusion length, diffusion coefficient, absorber thickness and so on [137]. In this regard, we are assuming a simple equation for this parameter to insert in the generation mechanism equations. This is the novelty of our simulations that makes the analysis closer to reality where the generated carriers will have probability for recombination and loss in the absorber region during transfer process to the electrodes. In the forward bias condition, this will not cause the light current to superimpose as the recombination process is also dependent on this parameter and in the results we have shown a reduction by that. Also, the presence of this parameter hampers the applicability of the expression when the recombination in the space charge region becomes significant. The recombination rate in the absorber (region 2) where  $n \ll p$  and for the case of forward applied bias of  $qV \gg kT$  is given by;

$$U_2(x) = B\Delta n(x)\eta_{c,2}(x), \quad (36)$$

where B is the recombination coefficient for non-degenerated material. The recombination loss in the absorber region is dominated by mid-gap centers or traps (SRH recombination) rather than band-to-band, radiative recombination. This is highly likely for CIGS solar cells. According to Roosbroek-Shockley-like relationships parameter B can be defined by [140],

$$B(E) = [2\pi/c^2 h^3 n_0] \int_{E_{g0}}^{\infty} E^2 dE / (\exp(E/kT) - 1), \quad (37)$$

Furthermore, in Eq. (36),  $\Delta n(x)$  is the excess of electrons in the CB, over that of the equilibrium [137]

$$\Delta n(x) = n_0(\exp(qV_e/kT + x/L_n) - 1), \quad (38)$$

$n_0$  is the electron concentration of the CB in equilibrium. The exact value of  $n_0$  is irrelevant in this model because this parameter also appears in B and, hence, they cancel out each other. The quantity  $qV_e$  is the

split between the electron and hole and quasi-Fermi levels in the absorber layer ( $V_e=0.2$  V). Replacing all these definitions into Eqs. (1)- (3), the photocurrent density of the regions 1 and 2 and total photocurrent of the cell are obtained under different conditions. The integrals of the above equations are complicated and have been calculated with Mathematica [141]. In the proposed model, we neglected interface and tunnelling enhanced recombination and saturation currents of the cell. As emitter doping has a strong effect on the interface recombination, a high doping or to be more precisely the absorber/emitter doping ratio, helps to reduce interface recombination. For an absorber doping density of  $10^{14}$ - $10^{18}$   $\text{cm}^{-3}$ , window doping density of  $10^{20}$   $\text{cm}^{-3}$  will switch off the interface recombination [137].

### 6.3 Optimization of the photocurrent density

We study a profile with a linearly increased band gap for the CB and with the VB kept constant through the absorber. This grading can be obtained with grading the gallium component in  $\text{Cu}(\text{In,Ga})\text{Se}_2$  material. It has already been shown that this grading increases the generation current of the cell [148], but here we provide an analytical approach which takes into account the influence of some effective parameters on the photo-generation of the cell (e. g., carrier collection function). We present a simple analytical model for the recombination and generation mechanisms of this graded band gap profile to consider their effects on the photocurrent density of the cell. The approach of this study is closer to reality as we used thickness (and then band gap) dependent absorption coefficient, collection function, excess minority carriers (Eq. (38)) and energy dependent radiative recombination (regarding B in Eq. (35)).

We will show that the calculations made with this model give very different results than those obtained with simplistic intuitive approaches such as calculating the photocurrent density of an averaged band gap profile or a variable band gap profile with a neglected recombination current or employing a constant carrier collection function through the cell. For this profile, with a  $d=2$   $\mu\text{m}$  absorber layer thickness,  $kT\zeta=0.2$   $\text{eV}/\mu\text{m}$  (which yields  $E_{gmax}=1.55$  eV), under AM 1.5 solar spectrum normalized to  $100$   $\text{mW}/\text{cm}^2$ ,  $\mu_e=50$   $\text{cm}^2/\text{V.s}$ , back surface recombination velocity  $S=10^3$   $\text{cm}/\text{s}$  we obtained the results shown in Fig. 50-Fig. 53. In Fig. 50, the total photocurrent density ( $J_{tot}$ ) is plotted versus the thickness of the cell for three different linear variations of the band gap between  $E_{gmin}$  and  $E_{gmax}$ . For this case, we neglect all recombination currents in regions 1 and 2. We assume that all generated carriers contribute to the photocurrent and the collection function is unity. The three upper curves are the graded band gap cells with different  $E_{gmax}$  and the lowest curve is a non-graded cell with a constant band gap ( $\zeta=0$ ). In graded cases ( $E_{gmax}=1.25$  eV,  $1.35$  eV and  $1.45$  eV), the photocurrent shows a higher value than in the constant case  $E_{gmin}=1.15$  eV. In our calculations we also introduced the nonlinear variable absorption coefficient as a function of the photon energy and cell thickness. Furthermore, whatever  $E_{gmax}$  increases, the photocurrent increases because of the lower recombination current of the minority carriers at the absorber region. Notice that, in the particular

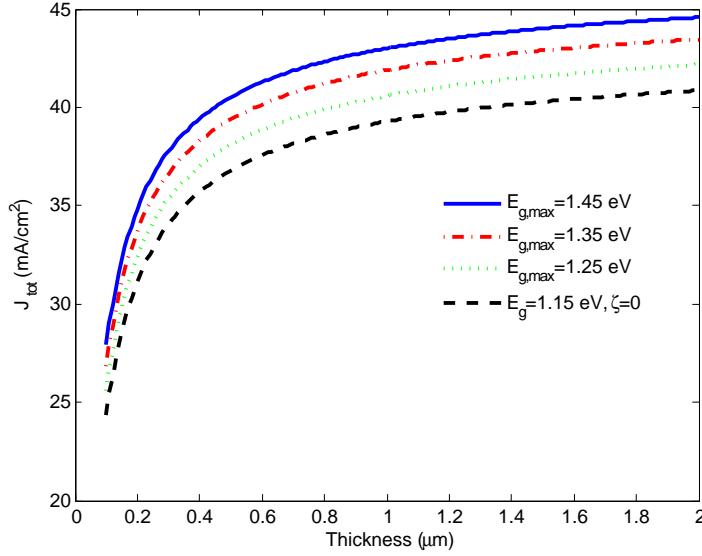


Figure 50: Photocurrent density as a function of absorber thickness for different  $E_{gmax}$  but constant  $E_{gmin} = 1.15$  eV

case of CIGS solar cells, the absorption coefficient causes an additional exponential increase for larger photon energies. This produces higher photocurrent density ( $J_{tot}$ ), as shown in Fig. 50. The photocurrent density using the effective absorption coefficient for the variable band gap material is much higher than the photocurrent density for a material with non graded band gap. The reason for the enhanced photocurrent in comparison with a non graded band gap cell is the nonlinear variation of the absorption coefficient as a function of the photon energy as occurs in direct band gap materials and as described in this model. The nonlinear absorption coefficient yields a better overlap with the solar spectrum and then absorption of the photons with high enough energy to be absorbed throughout the graded band gap can be taken into account. Due to variable absorption coefficient, the lowest curve also shows an increase for the photocurrent density, but with lower values in comparison with the graded cases. Therefore, the photocurrent density depends on the band gap via the absorption coefficient only. Obviously, the photocurrent density will reduce for the higher values of  $E_{gmax}$ , because the absorption ability of the cell reduces for higher  $E_{gmax}$ .

More realistic results obtained for the photocurrent density taking the recombination currents into account are shown in Fig. 51. We compared the photocurrent density of two cells with different values of  $E_{gmax}$ , excluding ( $U=0$ ) and including recombination currents through the cell. Fig. 51 shows that the recombination currents will reduce the photocurrent density of the cell. The point is that the reduction of the photocurrent density due to recombination currents is not uniform through the thickness of the cell. This is because the recombination current in SCR is greater than the one in the absorber region. On the other hand, grading the band gap prevents the recombination through the absorber material and the reduction of the photocurrent density in region 2 is lower than that in region 1. This is of course the purpose of grading the

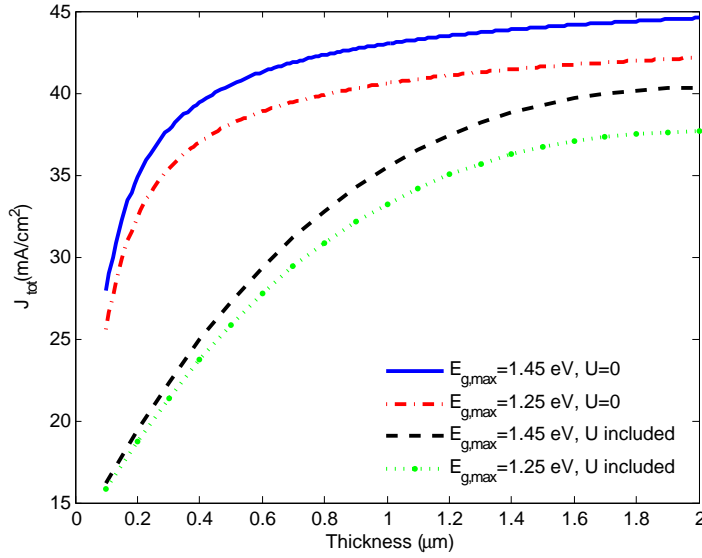


Figure 51: Photocurrent density vs. thickness excluding ( $U=0$ ) and including the recombination currents,  $\eta_{1,2}=1$

band gap. In this profile, the recombination current decreases in the back contact due to enhanced carrier collection which is amplified by the additional quasi-electric field. However, the recombination current in region 2 cannot reduce the photocurrent density very much since it is not the limiting current in the absorber region. Instead, the photocurrent density in SCR has a remarkable reduction because of recombination current. In our simulations, we also assumed that the carrier collection function exponentially depends on the diffusion length. This assumption allows a fast and easy way to highlight the influence of this parameter and diffusion length ( $L_n$ ) on the photocurrent density of the cell. In Fig. 52, the photocurrent density without recombination currents and for different diffusion lengths is plotted versus the thickness of the cell. The absorber region has grading with  $E_{gmin} = 1.15$  eV and  $E_{gmax} = 1.45$  eV. For diffusion lengths as long as the thickness of the cell ( $2\mu\text{m}$ ), the carrier collection function enhances the photocurrent density. As small diffusion lengths in the SCR limit the applicability of the analytical results considerably, we assumed  $\eta_{c,1}=1$  in region 1 and  $\eta_{c,2}$  variable with  $L_n$ . In the absorber material, the quasi-electric field, originating from the band gap grading, produces an increase in the photocurrent density due to an additional assist of the carriers to reach the contacts.

In contrast, for short diffusion lengths, the reduction is not negligible. The small diffusion lengths obtained lower photocurrent densities. Notice here that different values of diffusion lengths produce different values for carrier collection function regarding Eq. (36). For  $L_n$  close to  $2\mu\text{m}$ , the value of  $\eta_{c,2}$  holds in the range 0.5-1. For different combinations of  $L_n$  and  $kT\zeta$ , one can obtain identical collection functions. For the complicated case that  $\eta_{c,2}$  depends also on recombination velocity ( $S_n$ ) and diffusion coefficient ( $D_n$ ) [137], it can be shown that band gap grading significantly increases carrier collection and so the photocurrent

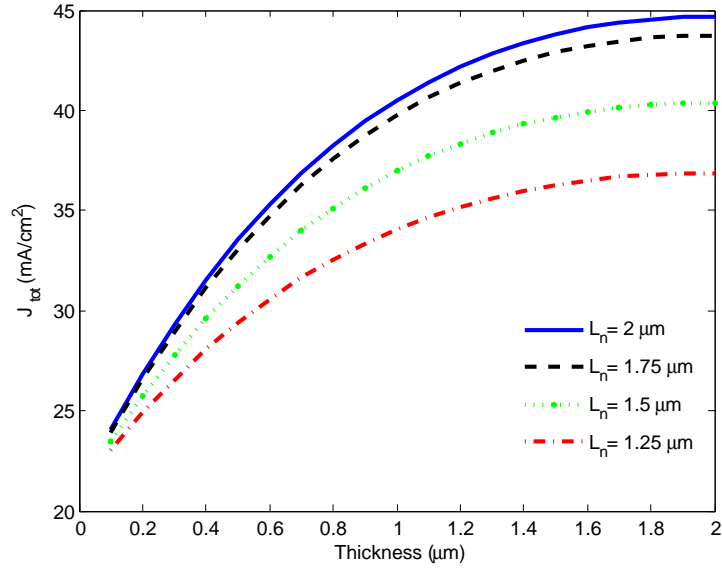
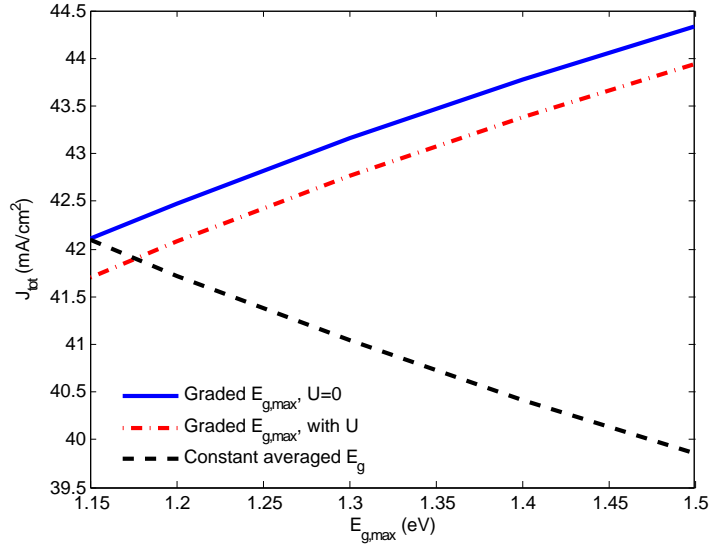


Figure 52: Photocurrent density as a function of thickness, for different values of  $L_n$  or carrier collection factor.

density. For example, a high ratio of  $S_n/D_n > 10^7 \text{ cm}^{-1}$  limits the carrier collection at the back contact. However, a large  $S_n/D_n$  with a graded band gap leads to a steep weakening of the collection function close to the back contact [146]. The photocurrent density with excluded and included recombination currents ( $U=0$  and  $U$  included, respectively) as a function of the grading strength  $E_{gmax}$  is compared with the photocurrent density of a constant averaged band gap cell ( $U=0$ ) in Fig. 53. It is shown that the photocurrent of a graded band gap cell is higher than that of a constant one even if the recombination current is included. It is an expected result while we graded the band gap to reduce the recombination effect on the photocurrent density of the cell. On the other hand, the energy and thickness dependent absorption coefficient causes an increase in the photocurrent density in comparison with the constant averaged band gap cell.

For increasing grading strengths or  $E_{gmax}$ , the absorption gain is reduced as the band gap is raised. This reduces the photocurrent density which decreases drastically for high grading strengths. Therefore, the detrimental effect of the grading on the light absorption leads to loss in carrier generation. Only slight grading can positively affect the photocurrent density. Steeper grading reduces light absorption too much. So, it proves that the photocurrent density of CIGS solar cells can be improved by band gap variation instead of just using an optimum single gap material. Graded band gap can be obtained with gradually modifying the gallium content through the absorber layer.

The lowest curve in Fig. 53, shows the reduction of the photocurrent density by increasing the average band gap due to reduction of the absorption of the photons with lower energy than band gap. A linear band gap variation converts the absorption law for a material where allowed direct transitions dominate

Figure 53: Photocurrent density versus  $E_{gmax}$  for  $E_{gmin} = 1.15$  eV

to a weaker energy dependence following the law for forbidden direct transitions. Generalising this insight, there is a trade-off between the decreased absorption due to a graded band gap and the increased current collection probability resulting from the quasi-electric field.

Overall, we presented a simple analytical model which gives a better understanding of the parameters influencing the generation and recombination mechanisms of grading band gap. The model considers the meaningful parameters and hence makes it fast to understand the physics of the problem. Using this model, one can also calculate the quantum efficiency of graded band gap absorbers, consider the effect of back contact recombination velocity as well as optical and electronic material parameters. The internal quantum efficiency is defined as the number of collected electron/hole pairs (photocurrent density) per photon incident on the absorber layer. Furthermore, as the photocurrent density gives the difference between the short-circuit and saturation currents, it is possible to obtain the current-voltage characteristics of the cell or its energy conversion efficiency. Further studies on the photocurrent generation and recombination in CIGS solar cells can be found in literatures [152, 153, 154].

#### 6.4 Auger generation mechanism

Solar cells based on  $\text{Cu}(\text{In,Ga})\text{Se}_2$  (CIGS) material exhibit remarkable conversion efficiencies up to 20.1% [131]. Increasing the efficiency of these cells is still a major research topic nowadays. Since 1980's, many technological and theoretical improvements have made it possible to increase their efficiency considerably in the laboratory scale [132]. This value is not close to the theoretical Shockley-Queisser limit [133] for

CIGS solar cells which leads to a lower efficiency of commercial CIGS modules comparing with large-scale applications of silicon based modules as a massive economically competitive energy source. Targeting high efficiencies, in order to go beyond the Shockley-Queisser limit, is obtainable by using photon energies that normally are lost in the cell. Solar spectrum consists of low energy photons, i. e., photons with energies less than cell band gap ( $h\nu < E_g$ ), that pass through the cell with a very low absorption, and high energy photons, i. e., photons with energies higher than the cell band gap ( $h\nu > 2E_g$ ), that generate hot carriers which are thermalized and cannot be efficient for the cell [134]. One possibility to use these low and high energy photons is band gap grading which has already been extensively studied.

Modern CIGS cell structures, however, are almost always graded by introducing a spatial variation of the Ga and/or In content within the absorber layer [145]. Such grading is present in the recorded  $>19\%$  efficient CIGS cells of NREL [108], and in the CIGS cells and modules which are now prepared for industrialisation by AVANCIS [146], Würth Solar [147] and others. Another method of targeting high efficiency in semiconductor solar cells can be, namely, Auger generation effect in which a high energy electron of the conduction band makes a transition to a lower energy in the same band. As a result, an electron from the valence band is excited to the conduction band. A common point of all these concepts is the generation of more than one carrier with a high energy photon which represents a better use of the solar spectrum [148, 135].

Hot carrier solar cells exploit the high energy photons by either a selective extraction of generated hot carriers or the creation of more than one electron-hole pair per photon by carrier multiplication [136, 149]. The effect of Auger generation between the valence and conduction bands has been experimentally shown for monocrystalline silicon solar cells but has not yet been exploited in CIGS solar cells nor for graded band gap cells.

In the following discussion, we present an analytical model to analyse Auger generation effect on the efficiency of a CIGS graded band gap solar cell considering the absorption coefficient, the generation and recombination rates regarding their dependency on the absorber thickness of the cell. Our theoretical approach assumes 100% carrier collection efficiency and supposes that all the photons reach the absorber without any generation or recombination in the SCR [138]. For different values of the front contact band gap ( $E_{gmax}$ ), we calculate the recombination and generation rates, the energy conversion efficiency and the current-voltage characteristics of the cell considering Auger effect.

We combine the concepts of grading band gap and carrier multiplication by hot carriers produced by Auger generation, in order to exploit energy of a wide range of energy photons in the solar spectrum. In fact, this study points out that the main benefit of a graded band gap is the reduction of Auger recombination and, moreover, the confinement of Auger recombination in some regions within the structure. However, in this section the ability of grading band gap is used to promote Auger generation in a thin film solar cell.

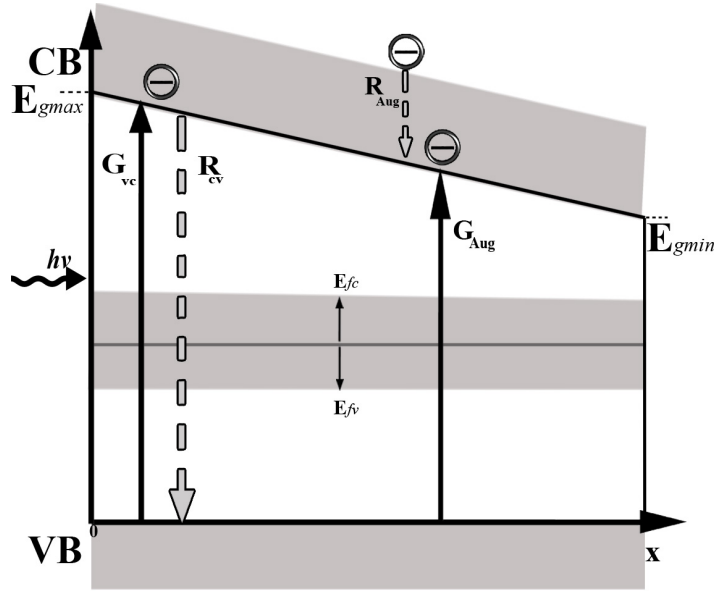


Figure 54: Reverse graded band gap absorber region of a CIGS solar cell.

### 6.5 Auger generation formulation

A detailed balance method is used to study the thermodynamic efficiency of a reverse graded band gap CIGS cell including Auger generation and recombination. In this study, the effect of carrier multiplication probability on the variation of efficiency and current-voltage characteristics due to the band gap grading at the front contact of the absorber material is analysed. In Fig. 54, the optical transition between the valence and conduction band pumps the electrons from VB to CB by an usual VB to CB transition (left hand side of the figure) and also by Auger generation (right hand side of the figure). In the latter transition, a CB hot electron falls into the CB bottom, but transfers its energy to another VB electron launching it into the CB.

Here, we have a process opposite to Auger recombination that is impact ionization where an electron from higher levels of the conduction sub-band collides with a VB electron and, as a result, gives its energy to the electron of the VB. The first one falls down to the CB edge and the second one rises up to the same CB edge. Assuming that nonradiative Auger process has a large rate, approximately the same rate can also be anticipated for the impact ionization process. It means that many Auger recombination and impact ionization processes occur while one radiative transfer from higher levels of the CB to the edge of the CB happens. We indicate  $E_{gmax}$  and  $E_{gmin}$  as the energetic values of the CB maximum (1.5 eV) and minimum (1 eV), respectively.

The carrier population of each band is described by a quasi-Fermi level, denoted with  $E_{fv}$  and  $E_{fc}$  for

the valence and conduction bands, respectively. As depicted in Fig. 54, the change of the cell band gap  $E_g$  is mainly caused by a change of  $E_{gmax}$  in the absorber. The energetic value of the VB edge remains constant [139, 140]. For this grading, the Ga content of the CIGS material needs to be controlled via the evaporation process. Controlling the evaporation rates of In and Ga makes it possible to vary the band gap over the absorber depth [150]. Based on a detailed balance model to calculate the thermodynamic efficiency, ignoring the emitter contributions and the Shockley-Read-Hall recombination, the current density  $J$  extracted from the cell is the difference of the generation current density  $J_{Gen}$  and the recombination current density  $J_{Rec}$  [151].

$$J(x) = J_{Gen}(x) - J_{Rec}(x), \quad (39)$$

where  $x$  is the position coordinate along the absorber layer as shown in Fig. 54. The former term depends on the geometrical concentration of the solar light, solar spectrum and intrinsic parameters of the generation mechanisms and the latter term depends on the difference between the quasi-Fermi levels and the cell temperature  $T_r$ . The carrier traps do not take part in these processes, although many different kinds of Auger effects with the participation of traps are likely important. Their discussion will be ignored and the band to band transitions analysed here will be the most important ones. However, one can analyse the other mechanisms which compete with Auger generation to obtain more realistic results. The current densities due to the generation and recombination of electrons are given as below

$$J_{Gen}(x) = q \int (G_{vc}(x) + G_{Aug}(x)) dx, \quad (40)$$

$$J_{Rec}(x) = q \int (R_{cv}(x) + R_{Aug}(x)) dx, \quad (41)$$

where  $q$  is the electron charge. In Eq. (40),  $J_{Gen}$  denotes the generation current density that constitutes the short-circuit current density of the cell which is obtained by the integration of the VB to CB transition generation rate ( $G_{vc}$ ) and Auger generation rate ( $G_{Aug}$ ).  $J_{Rec}$  is the recombination current density associated with the vanishing rate of electrons at the CB and holes at the VB, respectively. The recombination current density is found by the integration of the total radiative ( $R_{cv}$ ) and Auger ( $R_{Aug}$ ) recombination rates. The generation and recombination rate terms will be clarified in the following paragraphs. Of course, the radiative recombination and generation cannot be suppressed. In fact, radiative processes are competitive with Auger processes and could be more probable at different injection levels. We assume that radiative optical transitions by photon absorption or emission are possible between the bands. The generation rate for a transition between VB and CB and the corresponding recombination rate are given respectively by the number of photons absorbed and the generalized Planck's law [151],

$$G_{vc}(x) = \frac{4\pi}{c^2 h^3} \int_{E_g}^{\infty} \alpha_x \exp(-\alpha_x x) \frac{E^2}{\exp(E/kT_s) - 1} dE, \quad (42)$$

$$R_{cv}(x) = \frac{4\pi}{c^2 h^3} \int_{E_g}^{\infty} \alpha_x \exp(-\alpha_x x) \frac{E^2}{\exp(E - \mu/kT_r) - 1} dE. \quad (43)$$

In our model, we consider that the solar spectrum corresponds to a black body spectrum with a sun temperature  $T_s = 5760$  K and a room temperature  $T_r = 300$  K.  $E$  is the energy of the incident radiation,  $h$  is the Planck's constant,  $k$  is the Boltzmann constant and  $c$  is the velocity of light in vacuum.  $\alpha_x$  represents the absorption coefficient dependent on the absorber thickness and  $\mu(x)$  is the difference of the quasi-Fermi levels associated with the CB and VB:  $\mu(x) = E_{fc} - E_{fv}$ . The knowledge of this potential difference requires the solution of the carrier transport equations. However, in the absorber region and apart from the SCR region, this value stays almost constant even for the graded band gap [152, 153] and we assume it equal to 0.3 V as it has also been shown by other authors about Si solar cells. Also, this quantity has been calculated by SCAPS for CIGS solar cells showing a constant value in biased conditions [154]. It can be noticed that the radiative coefficient for CIGS devices is quite high [155], similar in its order of magnitude to that of GaAs cells.

Auger generation causes carrier multiplication with additional transitions between VB and CB due to the hot electrons generated by high energy photons ( $h\nu > 2E_g(x)$ ), in the graded band gap. Then, it generates a hot electron, which gives its excess energy to a new electron in the VB and pumps it from the VB to the graded CB. Auger generation rates are given as below [156, 157]

$$G_{Aug}(x) = \frac{4\pi}{c^2 h^3} \sum_{i=0}^{m_{max}} P^i \int_{(\theta+i)E_g(x)}^{\infty} \alpha_x \exp(-\alpha_x x) \frac{E^2}{\exp(E/kT_s) - 1} dE \quad (44)$$

$$R_{Aug}(x) = \frac{4\pi}{c^2 h^3} \sum_{m=0}^{\infty} \int_{(\theta+m)E_g(x)}^{(\theta+m+1)E_g(x)} (\sum_{i=0}^m P^i) \alpha_x \exp(-\alpha_x x) \frac{E^2}{\exp(E - [(m+1)\mu(x)]/kT_r)} dE. \quad (45)$$

We suppose that the carrier multiplication probability or averaged probability that a charge carrier will actually impact ionize is possible in the whole cell volume with the same probability. We denote  $P^i$  the probability of the  $i^{th}$  secondary electron after the generation of  $(i-1)$  electrons.  $m_{max}$  represents the maximum number of electrons generated by one photon. As the calculation of the thermodynamic efficiency needs reversibility, we suppose that in the energy interval  $[E_g + mE_{g0}, E_g + (m+1)E_{g0}]$ , the recombination process involves  $m$  captured electrons liberating  $mE_{g0}$  amount of energy to the same CB electron.  $\theta$  is a material parameter given by Eq. (46) in next sections. Clearly, for  $P=0$  we obtain the Shockley-Queisser result. However, we do not forget that, when comparing results to Shockley-Queisser, care must be taken as there is no mention of the thickness or absorptivity in their calculation deriving the limit for the case that all solar photons from the black body radiation at solar temperature are absorbed in the semiconductor.

The estimation of  $P$  (either averaged value or a function of the electron kinetic energy) is rather hard. If one does it theoretically, he has to take into account the main processes that compete with extra processes like the interaction with optical polar mode phonons, the deformation potential scattering and possibly the effect of the impurities present in the semiconductor. Beattie has done one of the most careful calculations of this type [158]. So, all the excess energy of a primary high energy photon is transferred to an additional electron.

Also Okuto and Crowell [159, 160] pointed out that the ionization probability is supposed to be zero immediately after each ionization process. After a certain distance from the window layer at  $x=0$ , the probability suddenly rises to a stationary value, determined by the local electric field. In the case of a constant positive electric field, the probability for an electron generated at  $x$  to impact ionize in  $x+dx$  depends on the microscope ionization coefficients [160].

In Eq. (44), the secondary generation rate (or Auger generation rate) is linked to the number of high energy photons. The inverse mechanism of the nonradiative low energy Auger generation is the nonradiative Auger recombination taking place between the CB and the VB.

Now, let the high energy photons in the incident radiation have energy  $E > \theta E_g$  ( $\theta > 2$ ). If  $\theta$  has an appropriate value for the material, then  $\theta E_g$  represents the excess energy in comparison with the threshold energy for Auger generation [161]. Appropriate values of  $\theta$  are obtained from [156]

$$\theta = 1 + \frac{2m_e + m_h}{m_e + m_h}, \quad (46)$$

where  $m_e$  and  $m_h$  are the the effective masses of electrons and holes in the conduction and valence bands, respectively. Here in the case of linearly graded band gap cell, the absorption coefficient  $\alpha_x$  changes as a function of position. For direct band absorption and for  $h\nu > E_g$  we can write with a good approximation [138]

$$\alpha(x, E) = A(E - E_g(x))^{1/2}, \quad (47)$$

where  $A$  is a constant which depends on the the effective masses of electrons and holes in the conduction and valence bands, respectively. As in our model the band gap changes as a function of position, the absorption coefficient will also change as a function of position  $x$  according to the above equation. However, it might be difficult to have experimental data for the absorption coefficient as a function of the band gap, and a simple model must be adopted. We shall consider semiconductors with a linear variation of the band gap from  $E_{gmax}$  to  $E_{gmin}$  as shown in Fig. 54. Then, for the band gap of the absorber region we get

$$E_g(x) = E_{gmax} - \beta x, \quad (48)$$

where  $\beta$  is given by

$$\beta = (E_{gmax} - E_{gmin})/d. \quad (49)$$

$E_{gmin}$  is the band gap at the end of the semiconductor layer having a thickness  $d$ . We can write

$$\alpha(x, E) = A(E - E_{gmax} + \beta x)^{1/2}. \quad (50)$$

By Eqs. (4) to (7),  $\alpha$  can be calculated regarding band to band or Auger transitions. For CIGS materials, detailed measurements of  $\alpha(x, E)$  show that Eq. (50) holds regardless of the Ga/(Ga+In) ratio which is

used for grading the absorber band gap during the growth process [138]. Consequently, the efficiency at different positions is calculated using the following expression

$$\eta = \frac{J(x)V}{P_{in}}, \quad (51)$$

where  $V$  is the cell voltage value at the maximum power and  $P_{in}$  is the incident power density at the front surface of the cell.

## 6.6 Parameters optimization for Auger generation probability

In this section, the graded band gap structure of a CIGS thin film solar cell has been used in order to analyse the effect of the carrier multiplication probability of Auger process on the conversion efficiency and current-voltage characteristics for various  $P$ ,  $\theta$  and  $E_{gmax}$  values. The calculations were made assuming a cell voltage  $V= 0- 0.8$  V, an incident power density,  $P_{in}$ , at the front surface of the cell equal to 100 mW/cm<sup>2</sup> and an absorber thickness  $d=3$   $\mu$ m.

The value used for the constant  $A$  was  $5 \times 10^4 \text{cm}^{-1} \text{eV}^{-1/2}$  in order to fit the typical reported values for the absorption coefficient in CIGS cells. Fig. 55 shows, for the reverse graded band gap cell ( $E_{gmax}=1.5$  and  $E_{gmin}=1$  eV), the optimized maximum efficiency versus the absorber thickness (equivalent to the absorber band gap) relative to different values of multiplication probabilities. A CIGS material with  $m_e/m_0= 0.2$  and  $m_h/m_0= 0.8$  where  $m_0$  is the free electron mass was considered. Therefore, according to Eq. (46), the curves of Fig. 55 are related to  $\theta=2.2$ . Comparing with the Shockley-Queisser limit of a single gap solar cell (31%), for smaller band gap and lower probability values, the efficiency of the graded band gap cell tends to the Shockley-Queisser limit.

The thermodynamic efficiency of the cell reaches 41% for an absorber thickness range of 1.5- 2  $\mu$ m and a band gap of about 1.15 eV. Notice that the absorber thickness range 0-3  $\mu$ m is equivalent to a reverse band gap of 1.5-1 eV. So, as indicated in Fig. 54, when the absorber thickness increases, the band gap is reduced. Obviously, for lower band gaps, the probability of Auger generation is increasing. Instead, for higher band gaps the generation of hot electrons, relevant for the carrier multiplication, becomes negligible as a lower number of photons in the solar spectrum can support Auger generation for higher band gaps and, consequently, the efficiency goes down again.

Thus, in Fig. 55, when  $P$  is zero, the cell behaves like a normal CIGS cell without Auger effect. When  $P$  goes to 1, the efficiency rises and the optimum band gap providing the maximum efficiency moves towards lower band gaps. Since the excess energy of hot photons is larger for lower band gaps, the number of electrons generated by carrier multiplication is higher. Therefore, Auger mechanism is much more effective at lower band gaps. For example, for band gaps higher than 1.5 eV, Auger mechanism becomes almost ineffective and the radiative transitions between VB and CB are reduced which causes a sharp reduction in

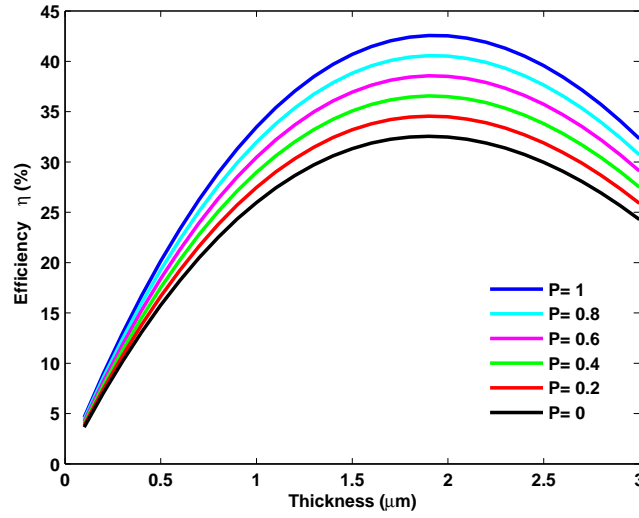


Figure 55: Efficiency vs. absorber thickness for different values of  $P$  ( $\theta=2.2$ ).

the efficiency. For the same reason, the efficiency approaches the Shockley-Queisser limit for higher band gaps.

To examine the possibility of transitions from the bottom of the CB to the top of the VB in order to make an Auger generation, we consider various values of  $\theta$  related to different values of the effective masses of electrons and holes in the conduction and valence bands, respectively. In Fig. 56, for different values of  $\theta$  between 2.0 and 2.5, the efficiency versus the band gap is shown. The carrier multiplication was assumed to be  $P=1$ . The lowest curve holds for  $\theta=2.4$  and the efficiency increases with decreasing  $\theta$ . We note an increase of the maximum efficiency around a band gap of 1.15 eV from 32.3% to 41.7% due to the carrier multiplication effect ( $P=1$ ).

The maximum efficiency for  $P=0$  (no Auger generation) is around 28% for  $\theta=2$ . For higher  $\theta$  values, a lower maximum efficiency is obtained due to higher effective masses of the carriers which effect the generation and recombination mechanisms. An increase of about 10% is obtained for the efficiency of the solar cells with lower  $\theta$  values. Clearly, a CIGS absorber with  $\theta=2.2$  has a high performance in its standard state. Si ( $E_g=1.12$  eV) and GaAs ( $E_g=1.43$  eV), as conventional solar cell materials, have  $\theta$  values of 2.37 and 2.12, respectively. This consideration confirms the CIGS material, with band gap higher than Si (close to optimum 1.5 eV) and  $\theta$  values higher than GaAs, as a good candidate for solar cell applications [156].

Then, we consider a CIGS cell with  $\theta=2.2$ . The variation of the efficiency as a function of  $E_{gmax}$  for various  $P$  values has been considered. The variation of  $E_{gmax}$  is limited to 1.5 eV but the conversion efficiency increases when  $P$  goes from 0 to 1. The beneficial effect of the grading band gap tends to zero as  $E_{gmax}$  tends to  $E_{gmin}$ . The band gap grading along with the carrier multiplication, and consequently,

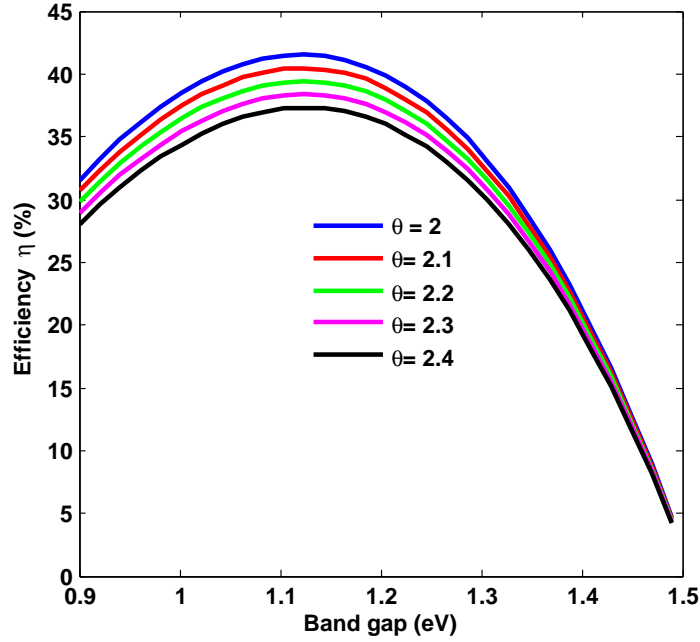


Figure 56: Efficiency vs. absorber band gap for different values of  $\theta$  ( $P=1$ ).

the excess energy of the hot photons, make it possible to exceed the Shockley-Queisser efficiency. The point is that, for lower band gaps, a further part of the solar spectrum can act as Auger generation source by producing hot photons [162].

The reverse grading increases the efficiency due to the presence of a greater barrier height (high built-in electrostatic field). Clearly, whenever  $P$  rises from 0 to 1, the maximum efficiency increases. In this case, the increment of the efficiency results from the increase in the number of hot electrons with an enhancement of the multiplication probability and reduction of the carrier recombination at the front contact by increasing  $E_{gmax}$ . The typical values of  $E_g$  in Cu(In,Ga)Se<sub>2</sub> may vary between 1.05 and 1.67 eV and they grow with a higher Ga concentration in CIGS components [161]. The highest efficiency is limited by the absorption property of the absorber material which depends on the photon energy and thickness (and then on  $E_{gmax}$  of the cell).

The fundamental mechanisms that limit the CIGS solar cell maximum efficiency are the transport and recombination losses. Band gap engineering can increase the conversion efficiency for the structures with thin CIGS absorber layers. In this way, the overall maximum open-circuit voltage and/or maximum conversion efficiency can be optimized.

Auger generation has an additional effect on the maximum conversion efficiency. Optimized  $E_{gmax}$  for graded profiles improves the efficiency for all the CIGS absorber thicknesses. The conversion efficiency improvements reach 41% achieved in a 3  $\mu\text{m}$  constant absorber thickness. The conversion efficiency of a

CIGS solar cell with  $E_{gmax}=E_{gmin}=1$  eV and non graded absorber is 35.1% for  $P=1$ . For  $E_{gmax}$  higher or closer to the optimal value (1.5 eV), the conversion efficiency can be improved due to lower recombination rates for the graded band gap regions.

CIGS material has a very high absorption coefficient and high energy photons are greatly absorbed in few tens of nanometres near the surface. For example, consider a point intermediate in the structure, e.g., with  $E_g=1.25$  eV. In order that impact ionization may occur, a photon with energy  $h\nu=2.5$  eV is required, but this photon would probably have been absorbed in the surface and thermalized before reaching that point. The chance for this hot carrier to reach a deeper point in the structure in which a second generation event can be promoted scarcely exists. Then, the possible positive effect of a graded band gap can be reduced. However, this assumption is valid for an ideal approach in order to calculate the maximum theoretical efficiency.

An example of a current-voltage characteristic of the considered cell with  $E_{gmax}=1.5$  eV and  $E_{gmin}=1$  eV is shown in Fig. 57. Auger generation increases the short-circuit current density  $J_{sc}$  and almost does not change the open-circuit voltage,  $V_{oc}$ . In fact, the absorber band gap determines the maximum  $J_{sc}$  of the cell. Decreasing the band gap increases  $J_{sc}$ , but decreases  $V_{oc}$ . In this case,  $V_{oc}$  does not change for various  $P$  values but still is higher than the non graded case [133]. The current density of the cell sharply rises from 41 mA/cm<sup>2</sup> to 50.2 mA/cm<sup>2</sup> when  $P$  goes from 0 to 1. Auger generation increases the number of carriers through the absorber layer.

Therefore, the number of photogenerated carriers and then the short-circuit current increase. Also, it has been shown that for probability values between 0.5 and 0.7,  $J_{sc}$  rises more slowly since in this  $P$  range Auger recombination rate becomes comparable with Auger generation rate. For higher values of the multiplication probability, Auger generation rate is faster and the variation of  $J_{sc}$  with  $P$  becomes nearly linear.

It has already been shown that the reverse grading enhances the photogeneration of the cell [162]. Fig. 57 shows the variation of the electrical quantities  $V_{oc}$  and  $J_{sc}$  of three cells with the  $E_{gmax}= 1.15, 1.3$  and  $1.5$  eV but all with  $E_{gmin}=1$  eV. The increase in  $J_{sc}$  is due to carrier multiplication and the increase in  $V_{oc}$  is due to higher grading strengths.  $J_{sc}$  values exhibit an increase up to 48.3 mA/cm<sup>2</sup> with increasing the  $P$  values up to 1 and the  $V_{oc}$  values reach almost 0.8 V for optimum  $E_{gmax}$  of 1.5 eV. Within our model, we stress that reverse grading affects the light absorption. Thus, increasing the multiplication probability values and  $E_{gmax}$  will shift the light absorption deeper in the cell which improves  $J_{sc}$  and  $V_{oc}$ , respectively. This maximum absorption becomes more pronounced for higher  $E_{gmax}$ . A higher grading strength increases  $V_{oc}$  by arising an electric field in the space charge region and reducing the recombination. In our simulations, we assumed that there was sufficient density of states for each band gap. Further considerations to assess the effect of carrier transport and recombination, the dependencies of physical parameters like optical absorption and carrier lifetime on the density of electronic states will be considered elsewhere.

This simulation and the results obtained may open a new way to carefully investigate Auger effect on CIGS solar cells as an effective phenomenon in generation mechanisms in all kinds of solar cells. Further

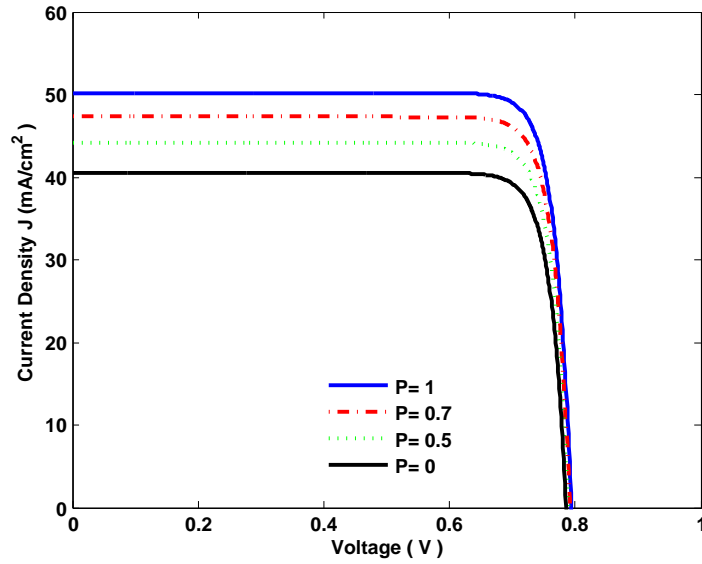


Figure 57: J-V characteristics for different values of  $P$  ( $E_{gmax}=1.5$  eV,  $E_{gmin}=1$  eV).

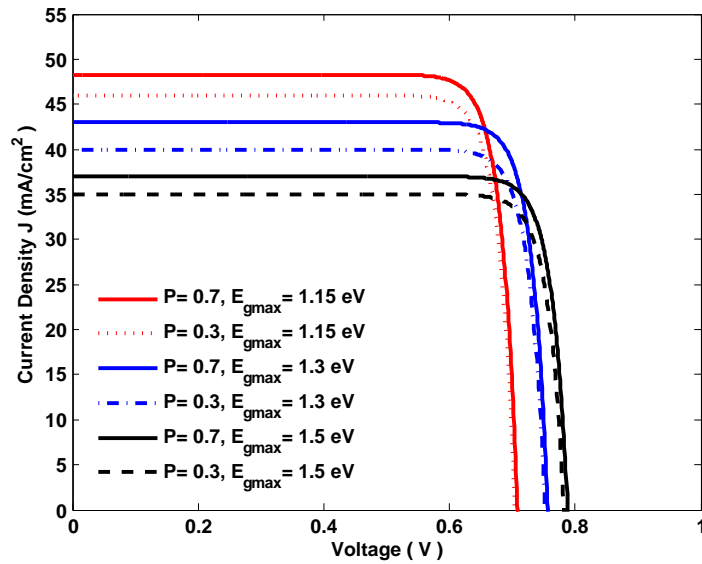


Figure 58: J-V characteristics for different values of  $P$  and  $E_{gmax}$  ( $E_{gmin}=1$  eV).

analysis to consider effects of the density of states on the efficiency and Auger generation may be carried out. The detailed balance equations are not appropriate for analysing the carrier mobility or state density effects in CIGS cells, but a different approach like the quasi-drift diffusion model can be employed for this purpose. In addition, the carrier collection, quantum efficiency, thin film quality effects (through recombination lifetime or surface recombination velocity) and effect of grain boundaries on Auger generation can be investigated for obtaining more realistic results. Nonradiative recombination mechanisms excluded in this analysis can also be included in further studies.

At present, more experiments and theoretical simulations for different material components in CIGS cells are needed to support these phenomena. Our calculation could be useful for device modelling and sheds some lights on the physical investigation of Auger mechanism in CIGS cells with graded band gap or/and different material components. Moreover, photon recycling effects, considered in graded band gap devices [5,6,7], can also be considered for the CIGS devices regarding Auger generation.

## 6.7 Conclusion of simulation and modeling

In this chapter, we proposed a new analytical model for the photocurrent density of a linearly increased graded band gap CIGS solar cell. In this model, the absorber cell thickness is divided into SCR and absorber region. For each region, we formulate the photocurrent density which includes the contribution of the generation and recombination current densities.

The total photocurrent density is assumed to be the sum of the photocurrent densities of the two regions. The model is closer to reality where we introduced the energy and thickness dependent absorption coefficient and thickness dependent collection function for generation and recombination rates of each region. The results show that grading the band gap improves the photocurrent density due to enhanced carrier collection since the additional quasi electric-field reduces the recombination through the absorber region. However, increasing  $E_{gmax}$  will reduce the photocurrent density due to lower absorption for higher band gaps.

The recombination current reduces the photocurrent density with a higher reduction in SCR region. For longer diffusion lengths (or higher collection factors) the photocurrent density is increased. Therefore, we propose the design of larger band gap cells to lower the recombination currents and a lower band gap for absorption enhancement. The thermodynamic efficiency of a reverse graded band gap CIGS thin film solar cell with and without Auger effect has been investigated using detailed balance equations. The variation of the efficiency for a graded band gap solar cell under different multiplication probability values has been studied. The maximum efficiency of about 41% was obtained for the highest multiplication probability value ( $P=1$ ) which is higher than the maximum efficiency of about 31% without Auger generation ( $P=0$ ).

The optimum band gap for the carrier multiplication was found to be about a non graded band gap (1.15 eV) since Auger mechanism was much more effective at lower band gaps. Auger generation from

---

hot electrons associated with a graded band gap has benefit in comparison with the purely radiative CIGS solar cell. As hot electrons generated by high energy photons are involved, the multiplication zone tends to lower band gap region where the absorption of low energy photons is high enough. Also, we considered the variation of the conversion efficiency due to the parameter  $\theta$  which characterizes the absorber material propriety for the solar cell applications. The results obtained confirmed CIGS as a promising material for this purpose due to its sufficient values of the carriers effective masses. Furthermore, the current-voltage characteristics with varying the multiplication probability have been investigated for this cell. The short-circuit current density clearly increases with increasing  $P$  while the open-circuit voltage does not change significantly. The increase in  $J_{sc}$  is due to Auger generation in the cell by high energy photons. In a different case, for three cells with different  $E_{gmax}$ , we calculated the J-V characteristics considering two values of the multiplication probability. Auger generation effectively enhances  $J_{sc}$  by the probability factor  $P$  as a result of increased generation rate. Furthermore, the significant increase of  $V_{oc}$  is due to increased  $E_{gmax}$ . No experimental tests were available for Auger generation in CIGS solar cells that could be compared with the obtained theoretical results.

## CONCLUSIONS

- The effect of shunting pinholes on the electrical parameters of CdTe devices was considered systematically.
- The CdCl<sub>2</sub> treatment of CdTe devices was modified to significantly improve the electrical parameters
- The water rinse was proposed for surface modification to improve the series resistance of CdTe thin film solar cells
- The effect of annealing in Ar ambient on the series & shunt resistances of CdTe devices was enhanced by water rinse
- The degradation rate of the electrical parameters of these cells under different stress conditions (bias, temperature, illumination, etc.) was numerically simulated
- The surface photovoltage spectroscopy was proposed to extract the band gap & defects of CIGS devices
- The valence band grading of CIGS devices was proposed to improve the hole passivation and increasing the photocurrent
- The photocurrent density was modeled with assumptions closer to reality and optimized effect of grading strength
- The Auger generation was proposed to improve the efficiency of the graded band gap CIGS solar cell

## REFERENCES

- [1] A. Chirila, P. Reinhard, A. R. Uhl, D. Keller, S. Buecheler, A. N. Tiwari, *Nature Materials*, 12 (2013) 1107-1111.
- [2] M. Gloeckler, I. Sankin, Z. Zhao, *IEEE J. of Photovoltaics*, 3 4 (2013) 6588601 1389-1393.
- [3] A. Jasenek, H. W. Schock, J. H. Werner, and U. Rau, *Appl. Phys. Lett.*, 79 (2001) 2922-2927.
- [4] W. Shockley, H. J. Queisser, *J. Appl. Phys.* 32, (1961) 510.
- [5] H. J. Queisser, Photovoltaic multiplicities, AIP Conf. Proc. 404 (1997) 267.
- [6] M. Gloeckler, J. R. Sites, *J. Phys. Chem. Solids* 66 (2005) 1891.
- [7] D. Attygalle, V. Ranjan, P. Aryal, S. Marsillac, R.W. Collins, *IEEE J. of Photovoltaics*, 3 1 (2013) 375-380.
- [8] P. Reinhard, A. Chirila, P. Blosch, S. Buechelers, A. N. Tiwari, *IEEE J. of Photovoltaics*, 3 1 (2013) 572-580.
- [9] M. S. Keshner, R. Arya, (2004), *Study of Potential Cost Reductions in Large-Scale Manufacturing of PV Modules*, NREL.
- [10] P. M. Kaminski, F. Lisco, J. M. Walls, *IEEE J. of Photovoltaics*, 99 (2013) 1-5.
- [11] Dennis J. Coyle, *Prog. Photovolt: Res. Appl.*, 21 (2013) 156-172.
- [12] P. V. Meyers, C. H. Liu, T. J. Frey, *U. S. Patent*, No. 4, 719 (1987) 589.
- [13] Y. Roussillon, D. M. Giolando, D. Shvydka, A. D. Compaan, V. G. Karpov, *Appl. Phys. Lett.*, 84 4 (2004) 616.
- [14] V. G. Karpov, A. D. Compaan, D. Shvydka, *Appl. Phys. Lett.* 80 22 (2002) 4256.
- [15] M. Mitra, J. Drayton, M. L. C. Cooray, V. G. Karpov, and D. Shvydka, *J. Appl. Phys.* 102, 034505 (2007).
- [16] V. G. Karpov, D. Shvydka, Y. Roussillon, *MRS Symposium Proc.*, 865 F10.1 (2005) 307-318.
- [17] D. W. Niles, D. Waters, D. Rose, *Appl. Surface Science* 136 (1998) 221229.
- [18] J. Lee, *Current Applied Physics* 11 (2011) S103-S108.
- [19] T. Muszynski, D. Shvydka, V. G. Karpov, *Proc. 31<sup>th</sup> IEEE PVSC*, (2008) 4922536.
- [20] N. R. Paudel, "Stability Issues in Sputtered CdS/CdTe Solar Cells ", *Thesis*, University of Toledo, (2011) pp. 41-50.
- [21] D. Shvydka, A. D. Compaan, and V. G. Karpov, *J. Appl. Phys.*, 91 11 (2002) 9059.
- [22] N. R. Paudel, Y. Yan, *Thin Solid Films*, 549 (2013) 30-35.
- [23] Private Communication with Kwon Dohyoung, Department of Physics, *Thin Film PV Lab*, University of Toledo, USA.
- [24] N.R. Paudel, K.A. Wieland, A.D. Compaan, *MRS Proc.* 1323 (2011) 834.
- [25] V. G. Karpov, *Phys. Rev. Lett.* 91 22 (2003) 226806-1.
- [26] N. R. Paudel, D. Kwon, K. Wieland, S. Asher, A. D. Compaan, *Proc. 35<sup>th</sup> IEEE PVSC*, 5614605 (2010) 1009-1013.
- [27] D. Shvydka, V. G. Karpov, *Proc. 31<sup>th</sup> IEEE PVSC*, (2005) pp. 359-362.
- [28] L. Sandrolini, M. Artioli, U. Reggiani, *Appl. Energy*, 87 2 (2010). 442-451.
- [29] Y. Roussillon, V. G. Karpov, D. Shvydka, J. Drayton, A. D. Compaan, *Appl. Phys. Lett.*, 96 12 (2004) 7283.
- [30] D. Shvydka, J. Drayton, M. Mitra, S. X. Marsillac, F. Jacob, *Proc. 4<sup>th</sup> IEEE PVSC*, 4059664 (2007) pp. 465-467
- [31] D. Shvydka, J. P. Rakotoniaina, O. Breitenstein, *Appl. Phys. Lett.* 84 5 (2004) 729.
- [32] V. Krishnakumar, A. Klein, W. Jaegermann, *Thin Solid Films*, 545 (2013) 548-557.
- [33] A. Salavei, I. Rimmaudo, F. Piccinelli, P. Zabierowski, A. Romeo, *Sol. Energy Mat. & Sol. Cells*, 112 (2013) 190-195.
- [34] V. Rejo, I. Riech, J. L. Pena, *Solar Energy* 95 (2013) 319-324.
- [35] A. Rios-Flores, O. Ares, J. M. Camacho, V. Rejon, J. L. Pena, *Solar Energy*, 86 (2012) 780-785.
- [36] M. D. Abramoff, P. J. Magalhaes, S. J. Ram, *Biophoton. Int.*, 11 (2004) 36-40.
- [37] Y. Park, Suho Lee, Junsin Yi, B. D. Choi, D. Kim, Jaehyeong Lee, *Thin Solid Films*, 546 (2013) 337-341.
- [38] C. Ding, Z. Ming, B. Li, L. Feng, J. Wu, *Materials Science & Engineering B*, 178 (2013) 801-806.
- [39] T.A. Gessert, S. H. Wei, J. Ma, D. S. Albin, H.R. Moutinho, *Sol. Energy Mat. & Sol. Cells*, 119 149-155 (2013).
- [40] M. Emziane, K. Durose, D. P. Halliday, A. Bosio and N. Romeo, *J. Appl. Phys.*, 100, 013513 (2006).
- [41] H. Arizpe-Chavez, F. J. Espinoza-Beltrán, R. Ramirez-Bon, *Solid State Communications*, 101, 1, 39-43, (1997).
- [42] M. Emziane, K. Durose, D. P. Halliday, A. Bosio and N. Romeo, *J. Appl. Phys.*, 100 (2006), 0135131-9.
- [43] V. Vadna, *Sol. Energy Mat. & Sol. Cells*, 87 (2005) 369-373.
- [44] M. E. Hernandez-Torres, R. Silva-Gonzalez, G. Casarrubias-Segura, *Sol. Energy Mat. & Sol. Cells*, 90 (2006) 2241-2247.
- [45] L. Alejo-Armenta, F. Espinoza-Beltrán, C. Alejo-Armenta, R. Ramirez-Bon, *J. Phys. & Chem. of Solids*, 60 (1999) 807-811.
- [46] C. Fenga, W. Yin, J. Nie, X. Zu, M. Huda, S. Wei, M. Jassim, Y. Yan *Solid State Communications*, 152 18 (2012) 1744-1747.
- [47] M. Hernandez-Torres, R. Silva-Gonzalez, J. Gracia-Jimenez, *Solar Energy Materials & Solar Cells*, 90 (2006) 2241-2247.
- [48] S. Jimenez-Sandoval, J. Carmona-Rodriguez, D. Dahlberg, *Sol. Energy Mat. & Sol. Cells*, 90 (15) (2006) 2248-2254.
- [49] R. Ramirez-Bon, F. Espinoza-Beltrán, H. Arizpe-Chavez, F. Sanchez-Sinencio, *J. Appl. Phys.*, 79 10 (1996) 7682-7688.
- [50] M. F. Mendoza, R. C. Perez, O. Z. Angel *Sol. Energy Mat. & Sol. Cells*, 95 2023-2027 (2011).
- [51] A. Picos-Vega, H. A. Chavez, F. H. Espinoza-Beltrán, *Journal of Applied Physics*, 89 (11 I) (2001) 6073-6078
- [52] D. C. Jordan and S. R. Kurtz, *Prog. Photovolt: Res. Appl.* 21, 12 (2013). doi: 10.1002/pip.1182.
- [53] T. Ott, T. Walter, D. Hariskos, O. Kiowski, R. Schaffler, *IEEE J. of Photovoltaics*, 3 1 (2013) 514-519.
- [54] V. Fjallstrom, P. M. P. Salome, A. Hultqvist, M. Edoff, T. Jarmar, *IEEE J. of Photovoltaics*, 3 3 (2013) 1090- 1094.
- [55] M.A. Islam, Q. Huda, M.R. Karim, N. Amin, *Current Appl. Phys.*, 13 S115-S121, (2013).
- [56] D. S. Albin, Y. Yan, M. M. Al-Jassim, *Prog. Photovolt: Res. Appl.*, 10:309-322 (2002).
- [57] N. R. Paudel, K. A. Wieland, M. Young, S. Asher, A. D. Compaan, *Prog. Photovolt: Res. Appl.* (2013), in press.
- [58] M. R. Oliver, A. L. McWhorter, A. G. Foyt, *Appl. Phys. Lett.*, 11 4 (1967) 111-113.
- [59] V. G. Karpov, A. Vjih, and A. Vasko, *J. Appl. Phys.*, (2013), 103 (7) 074105.
- [60] A. Klaver and R. van Swaaij, *Sol. Energy Mat. Sol. Cells.*, 92 50 (2008) 454-460.
- [61] M. Burgelman, P. Nollet, and S. Degraeve, *Thin Solid Films* 361-362 (2000) 527-535.
- [62] M. Burgelman, K. Decock, S. Khelifi, A. Abass, *Thin Solid Films*, 535 (2013) 296-301.
- [63] M. Gloeckler, A. Fahrenbruch, J. R. Sites, *Proc. 3<sup>th</sup> World Conf. Photovo. Energ. A* (2003) 491-494.
- [64] S. Lany and A. Zunger, *J. Appl. Phys.*, 100 (2006) 113725.
- [65] D. J. Chadi, *Phys. Rev. B*, 59 (1999) 15181.

- [66] M. Stutzmann, W. B. Jackson, C. C. Tsai, *Phys. Rev. B*, 38 23 (1985).
- [67] D. Redfield, R. Bube, *Photoinduced Defects in Semiconductors*, Cambridge University Press, Cambridge (1996),345-360.
- [68] S. S. Hegedus B. E. McCandless, *Sol. Energy Mat. Sol. Cell* 88 (2005) 75.
- [69] J. F. Hiltner and J. R. Sites, *AIP Conf. Proc.* 462 (1998) 170.
- [70] D. S. Albin, *SPIE Optics+Photonics Meeting, Conf. NREL/CP-520-42811* (2008).
- [71] D. S. Albin, R. G. Dhere, S. C. Glynn, and W. K. Metzger, *Proc. 34<sup>th</sup> IEEE PVSC NREL/CP-520-46055* (2009).
- [72] T. A. Gessert, S. Smith, T. Moriarty, S. Johnston, A. Duda, *Proc. 31<sup>th</sup> IEEE PVSC* (2005).
- [73] G. Agostinellia, D. L. Batzner, and M. Burgelman, *Thin Solid Films* 431432, 407 (2003).
- [74] V. G. Karpov, *Phys. Rev. B*, 86 16 (2012) 165317.
- [75] M. J. Romero, C. Jiang, R. Noufi, and M. Jassim, *Appl. Phys. Lett.*, 87 (2005) 172016.
- [76] L. Kronik, Y. Shapira, *Surface. Science Reports*, 37 (1999) 1.
- [77] D. Cavalcoli, B. Fraboni, and A. Cavallini, *J. of appl. phys.*, 103 (2008) 043713.
- [78] F. Streicher, S. Sadewasser, T. Enzenhofer, H.-W. Schock, M.Ch. Lux-Steiner, *Thin Solid Films*, 517 (2009) 2349-2352.
- [79] M. Takihara, T. Minernoto, Y. Wakisaka, S.Yamada, *Proc. of 34<sup>th</sup> IEEE PVSC Conf.* (2009) 000561-000563.
- [80] L. Kronik, B. Mishori, E. Fefer, Y. Shapira, W. Riedl, *Sol. Energy Mat. & Sol. Cells*, 51 (1998) 21-34.
- [81] R. Chakrabarti, J. Dutta, S. Bandyopadhyay, D. Bhattacharyya, *Sol. Energy Mater. & Sol. Cells*, 61 (2000) 113-126.
- [82] M. Venkatachalam, M. Kannan, S. Jayakumar, R. Balsundrarpbhu, *Thin Solid Films*, 516 (2008) 6848-6852.
- [83] S. Sadewasser, T. Glatzel, D. Cavalcoli, A. Jager-Waldau, M.Ch. Lux-Steiner, *Appl. Phys. Lett.*, 80 (2002) 2979.
- [84] M. Nie, K. Ellmer, *Thin Solid Films*, 536 (2013) 172-178.
- [85] A. Darga, W. Favre, M. Fruzzetti, J. P. Kleider, N. Barreau, *J. of Non-Crystalline Solids*, 358 (2012) 2428-2430.
- [86] A. Castaldini, D. Cavalcoli, A. Cavallini, and M. Rossi, *Sol. Energy Mater. Sol. Cells*, 72 (2002) 559.
- [87] A. Cavallini, A. Castaldini, D. Cavalcoli, and B. Fraboni, *IEEE Trans. Nucl. Sci.*, 54 (2007) 1719.
- [88] A. Minj, D. Cavalcoli, A. Cavallini, *Physica B*, 407 (2012) 2838-2840.
- [89] A. Minj, D. Cavalcoli, A. Cavallini, *Thin Solid Films*, 9 3-4 (2012) 982-985.
- [90] W. N. Shafarman, R. Klenk, and B. E. McCandless, *J. Appl. Phys.*, 79 (1996) 7324.
- [91] A. Rajanikanth, Y. K. Takahashi and K. Hono, *J. Appl. Phys.*, 101 (2007) 023901.
- [92] A. Kumar Das, *Renewable Energy*, 52 (2013) 95-98.
- [93] I. M. Dharmadasa, *Advances in Thin Film Solar Cells*, pp. 13-22, (2011) Pan Stanford Publishing Ltd.
- [94] J. Hui Tan, W.A. Anderson, *Sol. Energy Mat. & Sol. Cells*, 77 (2003) 283-292.
- [95] H. Bayhan, M. Bayhan, *Solar Energy*, 87 (2013) 168-175.
- [96] U. Rau, K. Taretto, S. Siebentritt, *Appl. Phys. A*, 96 (2009) 221-234.
- [97] Z. Ouennoughi, M. Chegaar, *Solid-State Electron*, 43 (1999) 1985-1988.
- [98] U. Stutenbaeumer, B. Mesfin, *Renewable Energy* 18 (1999) 501512.
- [99] O. K. Echendu, A. R. Weerasinghe, D. G. Diso, F. Fauzi, I. M. Dharmadasa, *J. of Eelectronic Materials*, 42 4, 2013.
- [100] H. Bayhan and C. Ercelebi, *Semicond. Sci. Technol.*, 12 (1997) 600-608.
- [101] B. Werner, W. Koodenny, M. Prorok, T. Zdanowicz, *Sol. Energy Mat. & Sol. Cel*, 95 (2011) 2583-2587.
- [102] B. Werner, W. Kolodenny, M. Prorok, *IEEE International Workshop on Photonics*, Poland, (2008) 90-93.
- [103] M. Gloeckler, J. R. Sites, *Thin Solid Films*, 480 (2005) 241-245.
- [104] A. Kassis, M. Saad, *Sol. Energy Mat. & Sol. Cells*, 77 (2003) 415-422.
- [105] P. T. Landsberg, H. Nussbaumer and G. Willeke, *J. Appl. Phys.* 74 2 (1993) 1451-1452.
- [106] J. Merten, J. M. Asensi, C. Voz, A. V. Shah, J. Andreu, *IEEE Trans. Elect. Dev.* 45 2 (1998), 423-429.
- [107] D. Azulay, O. Millo, I. Balberg, H.W. Schock, D. Cahen, *Sol. Energy Mat. & Sol. Cells*, 91 (2007) 85-90.
- [108] I. Repins, M. Contreras, B. Egaas, C. Perkins, R. Noufi, *Prog. Photovolt; Res. Appl.*, 16 (2008) 235-239.
- [109] R. Menner, T. Walter and H. W. Schock, *Proc. 10<sup>th</sup> Photovolt. Sol. Energy Conf.*, (1991) 787-792.
- [110] M. A. Contreras, J. Tuttle, A. Gabor, J. Keane, R. Noufi, *Sol. Energy Mat. & Sol. Cells*, 41 (1996) 231-236,
- [111] M. Wolf, *Proc. IRE.*, (1960) 1246-1263.
- [112] D. Schmid, M. Ruckh, F. Grunwald, H. W. Schock, *J. Appl. Phys.*, 73 6 (1992) 2902-2909.
- [113] J. Mattheis, P. J. Rostan, U. Rau, J. H. Werner, *Sol. Energy Mat. & Sol. Cells*, 91 (2007) 689-695.
- [114] A. M. Acevedo, *E-MRS Spring meeting, Symposium B, Energy Procedia* 2, (2009) 169-176.
- [115] A. M. Acevedo, *Sol. Energy Mat. & Sol. Cells*, 93 (2009) 41-44.
- [116] S. K. Chattopadhyaya and V. K. Mathur, *Phys. Rev. B*, 9 8 (1974) 3517-3523.
- [117] J. Song, S. Li, C. Huang, O. Crisalle, T. Anderson, *Solid State Electronics*, 48 (2004) 73-79.
- [118] H. Zhu, A. K. Kalkan, J. Hou, S. J. Fonash, *AIP Conference Proc.*, Colorado, (USA), 462 (1998) 309-315.
- [119] T. Dullweber, O. Lundberg, U. Rau, H. W. Schock, J. H. Werner, *Thin Solid Films*, 387 (2001) 11-13.
- [120] K. Decock, J. Lauwaerta, M. Burgelmana, *E-MRS symposium B, Energy Procedia* 2, 49-54 (2010).
- [121] M. Turcu, I. M. Kotschau and U. Rau *Apply. Phys. Lett.* 91 3 (2002) 1391- 1399.
- [122] M. Turcu, O. Pakma, and U. Rau, *Appl. Phys. Lett.*, 80 14 (2002) 2598-2600.
- [123] C. H. Huang, *J. Phys. & Chem. Solids*, 69 (2008) 779-783.
- [124] C. H. Huang, *J. Phys. & Chem. Solids*, 69 (2008) 330-334.
- [125] S. H. Wei, S. B. Z.hang, and A. Zunger, *Appl. Phys. Lett.*, 72 24 (1998) 3199-3201.
- [126] T. Dullweber, U. Rau, R. Noufi, and H. W. Schock, *IEEE Trans. Electron Devices*, 47 12 (2000) 2249- 2254.
- [127] V. Izquierdo-Roca, X. Fontan, J. Garcia, L. Barrio, A. Rodriguez, *Apply. Phys. Lett.*, 94 (2009) 061915-0619153.
- [128] S. B. Zhang, S. H. Wei, and A. Zunger, *Phys. Rev. B*, 57 16 (1998) 9642-9656.
- [129] A. Niemegeers, M. Burgelman, *Apply. Phys. Lett.*, 67 6 (1995) 843-845.
- [130] T. Minemoto, T. Matsui, H. Takakura, T. Negami, *Sol. Energy Mat. & Sol. Cells*, 67 (2001) 83-88.
- [131] P. Jackson, D. Hariskos, E. Lotter, S. Paetel, R. Wuerz, R. Menner, *Prog. Photovolt: Res. Appl.*, 19 (2011) 894.
- [132] V. Nadenau, U. Rau, A. Jasenek, and H. W. Schock, *J. Appl. Phys.* 87 (2000) 584.
- [133] K. Thomas, R. Uwe, *J. Appl. Phys.* 102 10 (2007) 104510.

- [134] K. Decock, S. Khelifi, M. Burgelman, *Sol. Energy Mater. Sol. Cells*, 95 (2011) 1550.
- [135] G. L. Araujo and A. Marti, *Sol. Energy Mater. Sol. Cells*, 33 (1994) 213.
- [136] S. M. Sze, K. K. Ng, *Physics of Semiconductor Devices*, Wiley, Hoboken, (2007) 110-120.
- [137] R. Scheer, H. W. Schock, *Chalcogen. Photovolt. Phys., Techn. & Thin Films Devices*, Wiley, Germany, (2011) 87-120.
- [138] U. Rau, A. Jasenek, H. W. Schock, F. Engelhar, T. Meyer, *Thin Solid Films*, 298 (2000) 361.
- [139] O. Lundberg, M. Edoff, L. Stolt, *Thin Solid Films*, 480-481 (2005) 520.
- [140] J. I. Pankove, *Optical Processes in Semiconductors*, Dover, New York, (1975) pp. 108-111.
- [141] Wolfram Research, Inc., Mathematica V. 7.0, *Wolfram Research Inc.*, Champaign, IL, USA, (2007).
- [142] A. Morales-Acevedo, *Solar Energy*, 83 9 (2009) 1466.
- [143] H. Bayhan, *Solar Energy*, 83 3 (2009) 372.
- [144] H. Bayhan, A. S. Kavasoglu, *Solar Energy*, 80 9 (2006) 1160.
- [145] K. Thomas, R. Uwe, *J. Appl. Phys.* 102 (2007) 104510.
- [146] J. Palm, V. Probst, W. Stetter, R. Toelle, S. Visbeck, H. Calwer, O. Hernandez, *Thin Solid Films*, 451 (2004) 544.
- [147] M. Powalla, B. Dimmler, *Thin Solid Films*, 387 (2001) 251.
- [148] S. Kolodinski, J. H. Werner, T. Wittchen, H. J. Queisser, *Appl. Phys. Lett.* 63 (1993) 2405.
- [149] J. H. Werner, S. Kolodinski, H. J. Queisser, *Phys. Rev. Lett.* 72, (1994) 3851.
- [150] A. Dhingra, A. Rothwarf, *IEEE Trans. Electron Devices* 43 (1996) 613.
- [151] A. Luque, A. Marti and L. Cuadra, *IEEE Trans. Electron Devices* 50 (2003) 447.
- [152] N. H. Rafat, S. Habib, *Sol. Energy Mater. Sol. Cells*, 55 (1998) 341.
- [153] N. H. Rafat, A. M. Abdel Haleem, S. Habib, *Renewable Energy* 32 (2007) 21.
- [154] M. Burgelman, J. Marlein, *23<sup>rd</sup> Proc. PVSEC*, (2008), Valencia, Spain, 2151-2155.
- [155] P. J. Rostan, J. Mattheis, G. Bilger, U. Rau, *Thin Solid Films* 480-481 (2005) 399.
- [156] K. Puech, S. Zott, K. Leo, M. Ruckh, H. W. Schock, *Appl. Phys. Lett.* 69 (1996) 3375.
- [157] M. Ley, J. Boudaden, Z. T. Kuznicki, *J. Appl. Phys.* 98 (2005) 044905.
- [158] A. R. Beattie, P. T. Landsberg, *Auger effect in semiconductors*, Proc. R. Soc. A, 249 (1959) 16.
- [159] Y. Okuto, C. R. Crowell, *Phys. Rev. B*, 6 (1972) 3076.
- [160] A. Spinelli, A. Pacelli, A. L. Lacaita, *Appl. Phys. Lett.*, 69 (1996) 3709.
- [161] P. T. Landsberg, *Recombination in semiconductors*, University Press, Cambridge, (1991).
- [162] A. Morales-Acevedo, *Energy Procedia*, 2 (2010) 169.